Global Warm Rain Processes and Their Relationship with Environmental Conditions

By

Ethan L. Nelson

A dissertation submitted in partial fulfillment of
the requirements for the degree of

Doctor of Philosophy
(Atmospheric and Oceanic Sciences)

at the
UNIVERSITY OF WISCONSIN-MADISON
2017

Date of final oral examination: 11/20/2017

The dissertation is approved by the following members of the Final Oral Committee:
Tristan S. L'Ecuyer, Assistant Professor, Atmospheric and Oceanic Sciences
Steve A. Ackerman, Professor, Atmospheric and Oceanic Sciences
Larissa E. Back, Assistant Professor, Atmospheric and Oceanic Sciences
Mark S. Kulie, Assistant Professor, Geological and Mining Engineering and Science at Michigan Technological University
Grant W. Petty, Professor, Atmospheric and Oceanic Sciences

Abstract

Global Warm Rain Processes and Their Relationship with Environmental Conditions

by Ethan L. Nelson

Warm rain plays a crucial role in the tropics through radiation and precipitation. More specifically, warm rain contributes upwards of 14% of the total rain that falls in tropical regions. Prior estimates of microphysical processes–condensation and evaporation–associated with cloud and precipitation estimation have stemmed from instruments with a low sensitivity to shallow, lightly precipitating clouds that are characteristic of warm rain. This study uses an algorithm database built on cloud-resolving models and simulated radar observations of the model realizations. Observations from the CloudSat Cloud Profiling Radar are then used to estimate the impact of heating from warm rain in the tropics and globally. Analysis at a global and regional scale indicates that the layer of heating in warm rain remains generally invariant, while the entrainment layer of cooling above condensational heating increases with decreasing inversion strength. A merger with other latent heating estimates in the tropics offers observations of latent heating from all precipitation regimes; the synergy of these two datasets provides a framework for examining the relative contributions of each regime to the total heating from cloud and precipitation formation. Finally, composites are made of the Madden-Julian Oscillation to gauge the impact of warm rain in the MJO.

This work is dedicated to my dear friend, Dylan A. Lavin, who passed away in 2015.

Acknowledgements

I would like to begin by thanking my advisor, Tristan, for an inordinate amount of mentoring, brainstorming, caring, and involvement in both my research and academic work. The graduate school experience can be made or broken by an advisor–and I appreciate Tristan for being the best supervisor I could possibly ask for.

My research group members, and in particular my officemates Elin, Kate, and Marian, have been such a good group to work with. I consider you all not just colleagues but also friends. With a group this size, there is an enormous amount of knowledge and skill contained in our nexus. Going through the day to day grind of work would not be the same were I taking it on alone.

I thank my committee for overseeing my PhD and serving as key motivation to completing this work. Your encouragement and involvement over my time here has been so kind and helpful for my development as a professional scientist.

Additionally, I want to thank all of the staff in the Atmospheric and Oceanic Sciences department. Pete, Debbie, Kathy, Sue, Sonja, Chelsea, and Dee: your tireless dedication is integral to our existence as a functional academic unit.

Thank you to Shaima for nudging me to apply to the Cold North that is Wisconsin, which allowed me to fall in love with the University, Madison, and Wisconsin. And thank you to Don, Istvan, and Laurinda for your encouragement and support through my undergraduate years.

Outside of work, I must thank many of the communities that have welcomed me in. Asbury UMC has been a wonderful home, not only for the opportunities they provided me by teaching and volunteering but also by growing close to many of my fellow members and families. Bart, Dave, Willie, David, Nicole, Julie, Harold: thank you.

I also became involved in the OpenStreetMap community, where I was able to befriend fellow free and open source advocates from across the world. Attending States of the Map, working with the Data Working Group, and volunteering with Humanitarian OSM Team have been very rewarding extracurriculars.

I would like to thank my many friends–some of old and others new–who have kept me enlightened and sane during this time. The hockey games, gaming nights, lifting sessions, and so on generated so many memories that I will cherish. That includes Amy, Brandon, Chris, Erin, Brandon, Alex, Wyatt, Aaron, Matt, Walter, Sam, Will, Erik, Sheryl, Stephanie, Ryan, Eric, Michael, and Michael.

Without the support and love of my parents and family for over a quarter-century, it would be impossible for me to be where I am right now. I am also indebted to my ancestors for the sacrifices they made over their lives.

Numerous agencies have supported my time as a graduate student for funding and conference assistance, including NASA, AMS, DOE, and the State of Wisconsin. Madison was originally home to the Winnebago peoples and I am grateful to have worked and lived on this land.

My time as a graduate student has been one of enormous growth and change. In nearly every way, I have grown to be a better person, scientist, presenter, programmer, thinker, writer, reader, persuader, researcher, and more. I cannot thank or repay enough all of the people who have helped me throughout my entire lifetime.

On Wisconsin!

Contents

List of Figures

List of Tables

Chapter 1

Background

1.1 Introduction

Storms that reside in the marine boundary layer are responsible for much of the spread in global climate models when responding to a changing climate (Bretherton et al., 2013, Brient et al., 2016, Medeiros and Stevens, 2011, Nuijens et al., 2015, Randall et al., 2007, Wyant et al., 2006, and others). Furthermore, the boundary layer clouds that cause the greatest spread are those in subsiding regions of the general circulation (Bony and Dufresne, 2005), which are regions characteristic of clouds named "warm" that are composed only of liquid hydrometeors (Wood, 2012). This problem is compounded by inconsistencies between climate model representation of and observations of these clouds

(Wyant et al., 2006). Progress towards furthering this knowledge is made possible when considering newly devised observations from a satellite-based radar.

Without explicit simulation of the microphysical processes of convection and precipitation, climate models must rely upon accurate parameterizations to functionally represent the evolution and magnitude of such processes in a given grid box. Observations strictly of precipitation can satisfy this requirement to some degree, but given that precipitation is the integrated result of processes in the full column, there are important components missing in this measurement: the vertical distribution of hydrometeor formation and the temporal evolution of this distribution. Observation-based microphysical process estimates can be used to evaluate and validate the relationships utilized in climate model parameterizations by representing this vertical distribution and its evolution. And, while prior work has investigated microphysical processes in large-scale tropical clouds and precipitation (e.g. Tao et al., 2016), those studies have utilized measurement platforms that have some insensitivity to warm rain.

1.2 Satellite precipitation remote sensing precursors

Imagery from outer space can be traced back to Vergeltungswaffe-2 (V-2) ballistic missiles repurposed after World War II under the auspices of the United States Army Ordnance Department (Fraser, 1985). A team at Johns Hopkins Applied Physics Laboratory modified a V-2 to include a DeVry 35 mm camera that would later take photos after launching from the White Sands Missile Range in Alamogordo, New Mexico in 1946 (Fraser, 1985).

The recovered rocket camera provided a glimpse of Earth–and more importantly clouds for weather and climate purposes–that opened a new era of sensing from space.

Remote sensing instruments can be divided into two categories: those that only "listen," or measure, and those that both transmit and measure the return. The former are known as passive sensors and only measure radiation incident upon the device. Taking pictures in the visible part of the electromagnetic spectrum either from the ground or from aloft is one straightforward mechanism to passively sense atmospheric phenomena (e.g. Newell, 1982). But what humans can see with the naked eye is not the full picture. Radiation outside of the visible spectra has been realized for quite some time as important for Earth's energy balance (e.g. Dines, 1917), and sensors which can measure such have come in a wide variety of forms including pyrometers (Wedgwood and Banks, 1782), Leslie's cubes (Leslie, 1804), bolometers (Langley, 1900), pyranometers (Abbot and Aldrich, 1917), and radiometers (Dicke, 1946). In each of these cases, instruments were designed that allowed measurements of the electromagnetic radiation that was emitted or reflected by some item and transmitted through a medium to a distance away from the source. But, again, these measurements are passive and rely on native energy already in the system.

Actively transmitting and receiving the reflected electromagnetic radiation outside of the visible spectrum for interrogating atmospheric phenomena was developed and refined in the early Twentieth Century. One of the most prominent forms of this active remote sensing is radio detection and ranging, or radar. Radar technologies rapidly advanced

during and immediately after World War II with help from civilian research conducted at places such as the Radiation Laboratory at Massachusetts Institute for Technology, the Marshall research group at McGill University in Canada (under the "Stormy Weather" project name), and the General Electric Company in the United Kingdom (Atlas, 1990). Some of the first radar photos of weather systems available in the literature were presented in Maynard (1945), collecting images of frontal systems, thunderstorms, and hurricanes. National weather agencies soon began to deploy radars for continental-scale, operational purposes as the science of active remote sensing was refined, including precipitation estimation (Ryde, 1946), three-dimensional velocity measurement (Lhermitte, 1973), and hydrometeor size estimation based on dual-polarization (Seliga and Bringi, 1976) or dual-frequency (Eccles and Mueller, 1971) radars.

Unfortunately, observations taken from the ground suffer from issues of sampling. Most atmospheric state sensors such as thermometers, anemometers, and barometers only provide measurements at a point location. And, while sensors such as cameras and radars provided the ability to remotely sense, limitations still exist due to Earth's curvature. Moreover, all of these systems are usually located over land (with the exceptions of buoys) or are only away from land for short time periods (such as ships and airplanes), thus limiting continuous and long timescale measurement over much of the planet's area. The combination of remote sensing technology development and escalation of the Space Race resulted in advances for weather satellite technology (Kidder and Vonder Haar, 1995).

1.2.1 Passive satellite-based estimates

Among the first satellites to contain instrumentation for sensing the atmosphere were the Vanguard 2 in February 1959, Explorer 6 in August 1959, and Explorer 7 in October 1959 (Kidder and Vonder Haar, 1995). The first contained an optical sensor and, though thrown into an unplanned orbit, collected useable images (Hanel et al., 1960). The latter two were equipped with an array of bolometers to measure ultraviolet and infrared radiation (Suomi, 1961), though Explorer 6 also experienced unexpected orbit issues (Kidder and Vonder Haar, 1995). With instruments now able to orbit Earth and collect information about the atmospheric state, a natural progression was to exploit these observations and derive properties of the atmosphere, including weather phenomena. Rainbird (1969) provided a cursory overview of efforts utilizing infrared observations to estimate precipitation across the world, including a limited case study of water basin rainfall to radiation intensity relationships. The measurements yielded a slight trend of increased rainfall associated with lower radiation intensities but the relationship had considerable spread.

Barrett (1970) proposed a methodology for estimating distributions of rainfall from operational "nephanalyses," or charts of cloud cover, derived with visible imagery available from the Environmental Science Services Administration (now the National Oceanic and Atmospheric Administration) Operational Television Infrared Observation satellites launched in 1966 (Dubach and Ng, 1988). Barrett's approach entailed calculating a coefficient based on the monthly mean cloud coverage and a subjectively generated probability

of both rainfall occurrence and intensity that was then constrained by observations. Sikdar (1972) presented satellite infrared intensity anomalies composited with rain gauge data and radar estimates, which had good agreement with one another, providing further confirmation of the potential ability to retrieve rainfall over large areas using satellite observations.

Development of passive satellite instruments and algorithms continued through the latter half of the Twentieth Century as geostationary satellites were launched to provide dedicated and stable data for forecasting (Kidder and Vonder Haar, 1995). Yet, to an extent, passive instruments provide only "flat" images–two dimensional information that was taken to be either at cloud top, the surface, or somewhere in the atmosphere based on estimated profiles of atmospheric state. Overall, drawbacks do exist in passive remote sensing due to some of the properties inherent in the observations: sampling time, footprint size, and algorithm uncertainties, yet their cost is lower and lifetime longer relative to active measurements (e.g. Ebert et al., 1996).

1.2.2 Active satellite-based estimates

By the mid 1980s, modeling efforts to understand dynamics of the tropics demonstrated that the vertical distribution of precipitation, and not simply the horizontal scale, was an important factor in simulation of the tropics (Hartmann et al., 1984). In this sense, vertical structure of precipitation is a reference to the precipitation formation processes and associated latent heating with cloud systems in the equatorial region. Investigations

of this type led Simpson et al. (1988) to posit, "It is important for modelers of large-scale circulations to know the location and amount of heat release in the atmosphere. They need to know its vertical profile as well as its horizontal distribution." Indeed, this statement was a main motivating factor for the proposed Tropical Rainfall Measurement Mission (TRMM). The novelty of TRMM was launching a science-based active remote sensor–a radar–on a spaceborne platform. TRMM's Precipitation Radar (PR), a Ku-band across-track scanning instrument, served not only as a proof of concept for active remote sensing from space but also played an instrumental role in building knowledge of global precipitation distributions.

Later efforts in active remote sensing for precipitation culminated in the Afternoon Constellation, or A-Train, containing both the CloudSat and Cloud-Aerosol Lidar and Infrared Pathfinder Satellite Observation (CALIPSO) satellites (Stephens et al., 2002). CloudSat was proposed to be an instrument with high sensitivity to clouds and light precipitation; it launched with the nadir-pointing Cloud Profiling Radar (CPR), a W-band (94 GHz) radar in 2006 (L'Ecuyer and Jiang, 2010, Stephens et al., 2008). CALIPSO was launched in the same vehicle as CloudSat and is equipped with a dual-wavelength lidar in the ultraviolet spectrum (Winker et al., 2009). Other active remote sensing satellites either launched or planned include the Global Precipitation Mission Core Observatory (Skofronick-Jackson et al., 2017) and EarthCARE (Illingworth et al., 2015).

1.3 Atmospheric heating

Though quantifying precipitation illuminates the transport of water from the atmosphere to the surface, the vertical distribution of that precipitation formation in the atmosphere is not necessarily diagnosed. Rather, energy released in the atmosphere from microphysical processes can be estimated in one of two methods. The first is a localized approach that entails measuring the fluxes of atmospheric components through some area. In doing so, the net sink or source can be estimated as a residual based on closure assumptions. The second method involves taking measurements at some moment in time and relating them to the physical processes that likely occurred to generate that state. Each approach has its own advantages and disadvantages, which are expanded on below.

With respect to tropical dynamics, latent heating was approached on a regional scale using localized atmospheric soundings. Reed and Recker (1971) explored this possibility with observations available twice a day from three stations in the equatorial West Pacific– the island of Ponape and the Kwajalein and Eniwetok atolls–to investigate properties of wave disturbances passing through the region. They first derived the pressure-integrated moisture budget over the region:

$$P - E = g^{-1}\frac{\partial}{\partial t}\int_{p_0}^{300}\overline{q}\mathrm{d}p + g^{-1}\int_{p_0}^{300}\overline{V\cdot\nabla q}\mathrm{d}p + g^{-1}\int_{p_0}^{300}\overline{q\nabla\cdot V}\mathrm{d}p, \qquad (1.1)$$

where P is net precipitation, E is surface moisture flux, g is the gravitational acceleration, t is a unit time, p_0 denotes the surface pressure, 300 is the pressure at 300 mb, q is the specific humidity, V is the horizontal wind, and the overbar denotes averages. Each of the three terms on the RHS represents a different component of storage. The first is simply the content of moisture present in the region; the second is the advection of water into the region by the horizontal wind; and the third is the converence or divergence of water vapor. One term neglected in their estimate is change due to condensation, since they only accounted for water vapor. Their calculations yielded positive advection estimates ahead of a trough and negative advection behind it. The largest changes ahead of a trough, however, were due to convergence of moisture–particularly at low levels.

They expanded upon budget work with an idealized budget to estimate the atmospheric heating at a given level:

$$\frac{1}{c_p}\frac{dh}{dt} = \frac{\partial T}{\partial t} + V \cdot \nabla T + \omega(\frac{\partial T}{\partial p} - \frac{\alpha}{c_p}), \tag{1.2}$$

where c_p is the specific heat holding pressure constant, h is the net heating per unit mass, T the temperature, ω vertical motion, and α the specific volume. This equation can be described in grouped terms with the diabatic heating equal to the sum of storage, advection by the horizontal wind, and the trade-off between vertical advection of temperature and adiabatic cooling due to vertical movement.

Yanai et al. (1973) provided a more explicit representation of heating considering the net effect of all processes in what is termed apparent heating (Q_1), derived from heat energy continuity:

$$Q_1 = \frac{\partial \overline{s}}{\partial t} + \overline{\nabla \cdot sV} + \frac{\partial \overline{s\omega}}{\partial p} = Q_R + L(c - e) - \frac{\partial}{\partial p}\overline{s'w'}, \tag{1.3}$$

where s is the dry static energy ($s = c_pT + gz$), Q_R is the radiative heating, L is the latent heat of condensation, c is the rate of condensation per unit mass of air, e is the rate of evaporation per unit mass of air, and primes indicate anomalies from the spatial mean. This inclusion of all heating terms allowed for the first estimates of the contribution of latent heating to overall heating in tropical clouds.

Localized observations for estimating heating over a region have been further utilized in work such as Thompson et al. (1979), Johnson and Ciesielski (2000), and Schumacher et al. (2007). In each case, the budget of the region must be adequately closed, meaning observations that are taken provide a representation of the fluxes in and out of the region. This requires not only a sampling strategy that ensures observations adequately sample the fluxes through the region but also adequately calibrated instruments so that relative differences between observing sites are captured (Mapes et al., 2003). But this approach as a whole, coming from first principles, does not require any assumptions of microphysical processes as no model is necessary for calculations.

Some of the earliest work generating quantitative latent heating estimates using larger-scale remote sensing observations and relating them to the microphysical processes occurring was Sikdar et al. (1970). They applied a theoretical convective model to geosynchronous Applications Technology Satellite images in order to calculate estimates of latent heating, E_c, as a result of cloud coverage changes at the outflow:

$$E_c = L \cdot \Delta W \cdot \frac{\rho_L}{K} \cdot (\Delta Z \cdot \frac{dA_c}{dt}), \tag{1.4}$$

where δW is the difference in water mixing ratio between the cloud base and top, ρ_L is the density of air, K is a constant relating the volume flux at the level of outflow to that at the level of inflow, δZ is approximately the vertical distance buoyant air can rise (given as $\sim$1 km), and dA_c/dt is the change in cloud coverage with time. Some of the constants used in this equation require atmospheric soundings to be derived, namely K and δZ. A misprinted figure (Fig. 8(b)) prevents some interpretation, but Sikdar et al. (1970) concluded that moderate thunderstorms exhibited greater latent heat fluxes than ordinary storms. They also remarked that clouds with less well-defined edges consisted of different structures than frontal storm systems, possibly indicating that subsidence at low levels is an important consideration in subtropical clouds.

As previously mentioned, information derived from passive observations is somewhat limited vertically. The availability of long-term three-dimensional measurements from

TRMM across the tropics over many years provided a large advance towards understanding the nature of latent heating observationally (Tao et al., 2016). The technical implementation of estimating latent heating from TRMM passive microwave and, in some cases additionally the PR, follows a general methodology of starting with a profile or assumption of vertical distribution of hydrometeors and calculating latent heating based upon that. As an example, the TRMM Hydrometeor Heating product estimates the profile of hydrometeors based on multiple frequencies of passive microwave observations and calculating mass fluxes therein (Smith et al., 1994, Yang and Smith, 1999). The use of only passive observations does require an accurate radiative transfer model to relate observations to states in a simulation database.

Another algorithm that followed this approach in TRMM estimates is the Spectral Latent Heating (SLH) product (Shige et al., 2009, 2008, 2004, 2007). SLH is a Bayesian algorithm that relates pieces of information about a given radar profile and finds a similar profile in a database populated with model simulations. Strengths of the Bayesian approach include accounting for measurement uncertainties, relating observations of a different nature (such as height and reflectivity), and providing a solution distribution that provides for spread in the possibility of states. And, more broadly speaking, the models employed in this scheme of retrieval can resolve the scales of convection, meaning they can represent the microphysics of the system instead of relying upon parameterizations. These and other algorithms related to latent heating have been extended now to the Global Precipitation Mission Core Observatory, with a payload that includes a dual-frequency satellite radar,

to follow the work of TRMM.

Despite the clear utility of these estimates, building algorithms upon a database of model states is not an error-free task. Ideally one would simulate every single possible atmospheric state assuming a perfect model representation of nature and simply match the observation to the fully-encompassing model database. This is difficult for a variety of reasons, notwithstanding the definition of a "perfect" model or the requirement of precise and accurate observations. In practice, a state-of-the-art model is instead used to simulate a variety of cases to generate a distribution space of possible atmospheric states that adequately represent reality.

Larger-scale remote sensing observations can also be used to generate radative heating estimates thanks to a similar model-coupled scheme. Measurements of radiation (the net result of column integrated transmission, emission, and scattering) at the top of the atmosphere have been available since Suomi (1961). And more continuous passive observations as Earth radiation budget missions matured have yielded not only radiation estimates in all sky conditions, but also provided enough sampling to give estimates strictly in clear sky conditions and thus generate a cloud radiative effect, or cloud forcing–the difference in net radiation between all sky and clear sky conditions (Wielicki et al., 1996, Zhang et al., 2004). However, the advent of the A-Train Constellation project, with nearly collocated instruments of diverse types and sensors particularly sensitive to clouds, has resulted in vertically-resolved profiles of radiation through the full atmosphere (Henderson et al.,

2013, Matus and L'Ecuyer, 2017). Similar to some of the mentioned latent heating algorithms, the A-Train algorithm, 2B-FLXHR-LIDAR, takes instantaneous observations of the atmosphere using both CloudSat and CALIOP combined with reanalysis atmospheric state data and runs a radiative transfer model to estimate the heating occurring in that profile.

1.4 Warm rain

The term "warm rain" refers to the regime of rain that has formed in a system below the freezing level in the atmosphere and thus containing only liquid droplets. That is not to say that all liquid-only clouds are classified as warm rain; indeed, water can exist in liquid form at heights above the freezing level (or in other words temperatures below freezing) in a supercooled state, but the classification of such hydrometeors requires additional observations beyond environmental temperature to test whether hydrometeors are liquid or not. Moreover, the mechanism of warm rain is not relegated to a single cloud type but rather is responsible for multiple regimes of clouds including full decks of stratocumulus, broken decks of stratocumulus, stratus, and isolated shallow convection over the ocean. Unfortunately, the nature of warm rain extending beyond only the lightest of rain rates has been somewhat unclear in the past.

Some of the first work to classify clouds by regime is succinctly compiled in Douglas (1934). In this, he categorized clouds based on their formation mechanism: frontal systems or other slowly convecting systems, strong convective systems, clouds maintained by

turbulence whether stratified or not, and lenticular clouds. For the class of clouds related to turbulent motions, Douglas (1934) stated that clouds may exist even in the presence of large-scale subsidence, that temperature and humidity discontinuities are the cause of clouds in these cases (cf. Augstein et al., 1974), and noted the presence of cumulus that penetrate layers of stratocumulus after extended periods of surface heating. He additionally stated that "[t]he complete history of a cloud often involves more than one type of physical process," an important consideration when viewing clouds at an instantaneous moment in time.

Work by Findeisen (1938) provided explanations about the microphysics of warm rain: "water clouds" consist of suspended droplets of different sizes growing either by condensation or collision and coalesence. Qualitative upper limits on the growing size of water droplets were speculated to be governed by the aerodynamics of droplets, ruling out electric attraction as a mechanism for the majority of growth. Conclusions regarding warm rain by Findeisen (1938), however, downplayed the significance of warm rain in the water cycle given that he stated the only precipitation predicted to be generated by these clouds is drizzle. Simpson (1941) also furthered the pretense that all rain types "other than drizzle" originate from clouds containing ice phase particles.

Observationalists often found many cases of warm precipitation over the oceans. Byers and Hall (1955), Ackerman (1956), and Battan and Braham (1956) provided observations of warm rain from an airplane-mounted X-band (3 cm) radar over the ocean near Puerto

Rico. While it was documented whether the cloud was in a precipitating state or not, the rate at which it was precipitating was not measured. A motivating factor for the broader Cloud Physics Project these studies describe was understanding some of the basic relationships between cloud physical extent and precipitation with a penchant for cloud seeding. Earlier flights near Hong Kong associated with a different campaign yielded observations of somewhat intense warm rain (over 3 mm hr^{-1}) in storms that had tops near 2.5 km with probed temperatures remaining above freezing (Heywood, 1940).

Some of the first large-scale observations including warm rain yielded similar cases where warm rain existed beyond the drizzle regime. A satellite-based analysis by Petty (1999) revealed that warm-topped clouds in the Pacific Warm Pool often exhibited precipitation rates beyond light drizzle. That study was based on derived cloud top temperatures strictly from passive infrared observations. Active and passive combined data indicated almost a fifth of tropical area precipitation was contributed by warm rain Liu and Zipser (2009). More focused observational campaigns continue to reveal both the drizzling and raining nature of warm rain *in situ*. The Rain in Cumulus over the Ocean (RICO) campaign (Rauber et al., 2007) found a third of the warm rain detected in a trade wind region mostly northeast of Barbuda was raining at over 1 mm hr^{-1} over a two month time period (Nuijens et al., 2009). Additionally they found that more humid environments may promote deeper warm clouds that rain more often. The Barbados Cloud Observatory has also seen examples of intensely raining warm rain (Stevens et al., 2016). In any case, it is clear that from a precipitation occurrence standpoint, the contribution of the warm rain

regime cannot be ignored.

1.4.1 The problem of warm rain sensing

Over the course of 17 years, TRMM provided observations of both precipitation and latent heating, among other quantities, using both the PR and associated passive instruments. Though Simpson et al. (1988) listed a proposed TRMM radar as a dual frequency Ku- (14 GHz) and Ka-band (24 GHz) instrument, the sensor was later refined to a single frequency Ku-band 13.8 GHz radar (e.g. Nakamura et al., 1990). Because of the relatively long wavelength in the Ku-band, it is less sensitive to smaller hydrometeors and misses some cloud-sized droplets and small rain droplets usually associated with warm rain. Another issue related to sensing small, isolated precipitation is that the radar field of view is 4 km, causing some issues in beam filling for these types of systems.

CloudSat is a satellite mission that was proposed to alleviate many of these constraints; it was designed from the start to focus on cloud and light precipitation observation. Figure 1.1 provides an example of the differences in sensitivity between the missions, displaying a nearly collocated overpass between CloudSat and the Ku-band radar on the Global Precipitation Mission Core Observatory that is analogous to the TRMM PR. Indeed, studies have shown that CloudSat does provide enhanced sensitivity to rainfall especially pertaining to the frequency of occurrence (Behrangi et al., 2012, Berg et al., 2010, Short and Nakamura, 2000), though some biases still exist for shallow precipitation due to a blind zone that extends about a kilometer above the surface (Christensen et al., 2013).

Complementing the suite of latent heating products available from TRMM, the Wisconsin Algorithm for Latent heating and Rainfall Using Satellites, or WALRUS, has recently become available (Nelson et al., 2016). WALRUS has a similar foundation to SLH by building a satellite retrieval based on a database populated from cloud-resolving model simulations. The target of WALRUS is warm rain systems, which reduces the complexity of microphysical assumptions by only simulating processes of condensation, evaporation, and collision-coalesence. WALRUS provides the ability to examine the global distribution of warm rain latent heating and, coupled with nearly collocated observations in the A-Train, could be used to estimate the total contribution of this regime to atmospheric heating both from microphysical processes and radiation.

1.4.2 Critical role of warm rain

A pressing need in the current stage of atmospheric science is refining simulations that compose the Coupled Model Intercomparison Project (CMIP; see Taylor et al. (2012) for an overview of the latest iteration, version 5). These simulations are the basis for reports by the Intergovernmental Panel on Climate Change (IPCC), an international body of scientists tasked with compiling and disseminating information about the past, current, and future states of the climate under the auspices of the United Nations.

Unfortunately CMIP5 models, and global climate models in general, often stumble when it comes to clouds, and understandably so given they are incredibly variable spatiotemporally yet are an intimate component of energy movement in the Earth system. This

intimacy results in a delicate balance that can easily be disrupted causing feedbacks or perturbations therein. Schneider (1972) demonstrated this with a simplified radiative model, which showed that the evolution of the simulated system was dependent not simply on an increase in clouds but rather the change in cloud radiative effect–a function of the cloud albedo compared to the surface and of the cloud extent and location both vertically and zonally. A survey of global climate model responses by Cess et al. (1990) revealed that differences in model behavior as a result of a sea surface temperature perturbation (simulating a global warming scenario) largely stemmed from variations in the response of clouds.

This conclusion has persisted in climate model behavior even with modern fully coupled systems between the land and ocean (Dufresne and Bony, 2008). This in part occurs because climate models must rely on parameterizations to simulate the processes within a grid box (Jakob, 2010). An emerging key to the uncertainty in cloud response is boundary layer cloud behavior in particular (e.g. Bony and Dufresne, 2005, Boucher et al., 2013, Zhang et al., 2013). It has also been shown that warm rain clouds can be affected by the local environment (e.g. Klein and Hartmann, 1993, Wood and Bretherton, 2006). Thus, warm rain plays a very critical role in the challenge of simulating the future climate and an open pathway to furthering progress on this topic is improving the understanding of how microphysical processes of warm rain respond to changes in the environment.

1.5 Madden-Julian Oscillation

With the advent of computing technologies and spectral analysis techniques (e.g. Kahn, 1957), Rosenthal (1960) began to analyze the nature of variations in the tropical troposphere as prior analyses employed spectral analysis mostly to stratospheric data. Working through Los Alamos Scientific Laboratory in New Mexico, Rosenthal (1960) obtained upper air data for seven stations for analysis with three to four months of data across the stations. In spite of the sparseness of the observations, a peak around the 5 day period was found in the power spectrum. Similar data analyzed by Yanai et al. (1968) also yielded a 5 day period peak with about three months of data; this was cautiously attributed to easterly waves. In both of these studies, the authors noted data over a longer time period was needed.

Shortly thereafter, Wallace and Chang (1969) carried out a spectral analysis of upper air data but had six months of observations. In power spectra of winds, humidity, and surface pressure, they found the same peak at 5 days the previous authors had associated with easterly waves. More importantly, they discovered a substantial portion of the power was confined to periods greater than 10 days. It was this longer time period of observations that allowed Wallace and Chang (1969) to provide some of the earliest evidence of what is now known as the Madden-Julian Oscillation. Because of Nyquist frequency limitations, however, the exact peak of this power could not be fully resolved (e.g. a 50 day MJO period wave would fit in a six month period only about five times).

The turning point for concrete evidence of a multiweek oscillation in the tropics was the analysis of Madden and Julian (1971). The authors utilized spectral analysis of ten years of atmospheric profiles taken at Canton Island which included surface pressure, and both lower- and upper-level wind data. Power spectra revealed a few notable items of interest: a peak existed in observational data around the period of 40 to 50 days, surface pressure and low-level zonal wind varied similarly, and low-level and upper-level zonal wind varied oppositely. A general description of MJO behavior was provided in a follow-on paper (Madden and Julian, 1972).

Monitoring the MJO is available through a variety of mechanisms (e.g. Kikuchi et al., 2012, Liu et al., 2016, Ventrice et al., 2013, among others), with a common method being the index proposed by Wheeler and Hendon (2004). Often named the "Wheeler-Hendon Index", and referred to as WHI herein, the index is calculated using two empirical orthogonal functions (EOFs) of outgoing longwave radiation, and lower- and upper-level zonal wind behaviors. The result is a two-dimensional phase diagram that segregates the MJO into one of eight Equatorial longitudinal slices. Phase is generally calculated on the day timescale and an intensity metric is also available based on the magnitude of the two EOFs.

Work since the discovery by Madden and Julian has tried to find the main drivers behind the MJO given not only its localized effects but also teleconnections to other climatic features (see Zhang (2013) for a review of teleconnections and Zhang et al. (2005) for a survey

of MJO theories). Representation of the MJO in global climate models is progressing with improved representation of the cloud regime spectrum and evolution therein, from shallow rain to deep convection (Park, 2014). Heating estimates from Tropical Ocean Global Atmosphere Coupled Ocean-Atmosphere Response Experiment (TOGA-COARE) observations yielded a vertically sloping pattern in anomalous heating over the eight WHI MJO stages indicating the lifecycle of convection from suppression that evolved into shallow and then deep convection followed by decay (Kikuchi and Takayabu, 2004). A similar trend appears in many modern reanalysis datasets, but such a pattern escapes TRMM heating estimates with low level initial heating missing (Jiang et al., 2011). Yet it is this shallow heating in incipient stages that has thought to be important for MJO growth (Zhang and Song, 2009). Observations that are sensitive to the shallow regime of precipitation on longer time scales than field campaigns could provide further credence to this theory.

1.6 To be Investigated

Ultimately, the preceding has motivated a study into the microphysical processes of condensation and evaporation within warm rain as a future benchmark for climate model evaluation. Specifically for this work, I aim to:

1. Document the global structure of warm rain processes,

2. Identify differences in process characteristics based on surrounding environment and location, and

3. Examine the context of warm rain in the full range of precipitation regimes, including the Madden-Julian Oscillation.

Investigation of these aims is possible because of recent advancement of remote sensing measurements and, in particular, instruments that can adequately sense the shallow and sometimes isolated nature of warm rain.

The following work represents an investigation from the global scale down to the regional scale. Chapter 2 outlines the approach, methodology, and areas of study for this work. Global distributions of warm rainfall and processes, as well as the broad impact of environmental conditions on these processes, are examined in Chapter 3, which has been submitted to the *Journal of Geophysical Research: Atmospheres*. Investigating these properties further at the regional scale occurs in Chapter 4. A more complete picture of latent heating in the tropics by merging views, with specific application to in the Madden-Julian Oscillation, is established in Chapter 5. A synthesis of the results and implications therein is covered in Chapter 6.

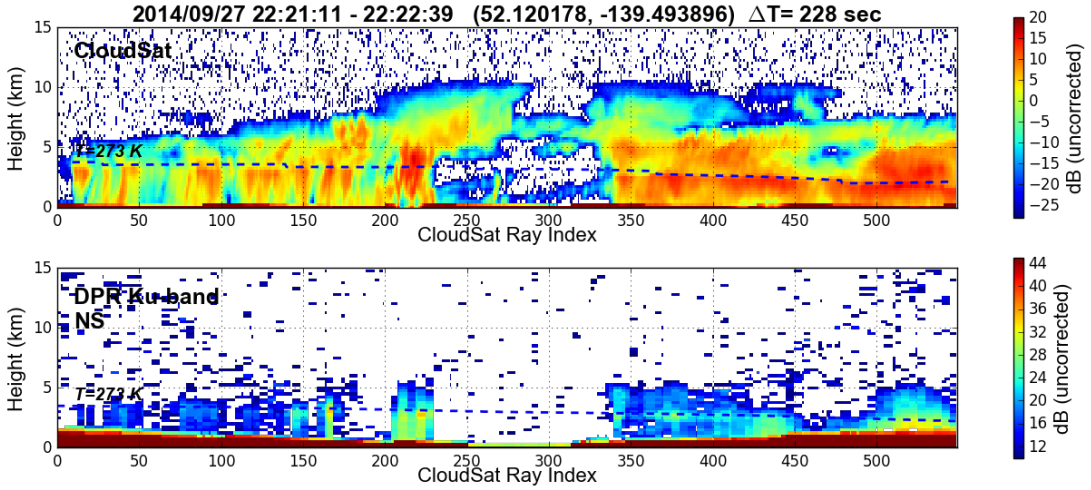

FIGURE 1.1: Example overpass showing radar observations [dBZ] from CloudSat and the GPM core observatory that were taken within four minutes of each other for a scene on 27 September 2014 near 52^{o}N, 139.5^{o}W (Turk, 2016).

Chapter 2

Investigational Tools

The following chapter provides information, both on the data sources and the methodology, that is employed in subsequent analysis. The main component of this analysis is an oceanic warm rain latent heating product available from the WALRUS algorithm that is used on CloudSat radar reflectivity observations. Reanalysis data is introduced to provide information about the atmospheric state for a given time. When assembling a merged picture of latent heating across all precipitation regimes, a similar latent heating dataset from TRMM observations is included.

2.1 Observations

2.1.1 CloudSat

CloudSat is a satellite in the polar-orbiting A-Train constellation that is equipped with the Cloud Profiling Radar (CPR) at a 94 GHz (W-band) frequency. The radar is nadir pointing, meaning it only profiles the atmosphere straight down to the surface with no side-to-side or front-to-back movement. Radar observations have a resolution of 1.4 km across the track and instantaneous observations have about a 1.7 km along track resolution (Stephens et al., 2008). Technical specifications place the vertical resolution at 480 m, but oversampling increases this to 240 m (Marchand et al., 2008). In addition, the bottom three to four vertical bins, extending up near 1 km above ground, are considered a blind zone to the radar because of ground clutter and backscatter contamination, which cloud lead to understimation of clouds confined strictly to this area. Particularly important for sensing clouds and light precipitation, the CPR minimum detectable reflectivity is near -30 dBZ (Tanelli et al., 2008).

CloudSat was launched in late 2006 and placed into orbit with an inclination of 98^{o} at 700 km height and an equatorial crossing time of 1:30 local time (L'Ecuyer and Jiang, 2010). For over four years, CloudSat provided nearly continuous observations from its orbit covering the globe up to about 82^{o}. In 2009, CloudSat began to experience intermittent issues related to the on-board battery system and finally stopped transmitting information in April 2011 (Keys, 2010, Nayak et al., 2012). Operations to recover from this issue were

successful before the end of that year with the decision to operate the radar and telemetry only during the day time when the solar panels are illuminated (Nayak et al., 2012).

Unfortunately, precipitation in the tropics is known to vary diurnally (e.g. Rozendaal et al., 1995). While issues of limited revisit sampling due to the satellite orbit cannot be averted, issues of limited diurnal sampling can be mitigated to the extent possible by restricting analysis to data that contains both day and night sampling. Therefore, CloudSat data extending from January 2007 to December 2010 are used in the following analysis. Though not a long enough time period to establish a climatology, this still allows composites over a multi-year period and has the added benefit of minimizing long term climatic trends.

Built around CloudSat is a suite of official algorithms that provide a variety of data for scientific application. The radar is a single-frequency, non-Doppler instrument, meaning observations from the radar consist of the vertical profile of backscattered radiation available in the 1B-CPR product, and the 2B-GEOPROF product provides converted radar reflectivity values for the full profile (Marchand et al., 2008).

Another algorithm, 2C-PRECIP-COLUMN, provides column information about precipitation, including path integrated attenuation (PIA) by hydrometeors and surface rainfall rate over the ocean (Haynes et al., 2009). Pulling in environmental information from reanalyses, 2C-PRECIP-COLUMN uses sea surface temperature and surface wind speed to gauge the difference–or extinction by hydrometeors–in returned surface reflectivity

compared to what is expected from modeling reflectivity off the sea surface (Li et al., 2005). In warm rain situations, uncertainty is reduced because of the simplification that all hydrometeors are liquid drops and no scattering assumptions regarding ice habit or orientation are required. That said, there are uncertainties in the PIA even in warm rain calculated by this method that are a function of the surface wind (Haynes et al., 2009), notwithstanding other inherent observational uncertainties.

Another rainfall product available from CloudSat is the 2C-RAIN-PROFILE algorithm. The theoretical basis for this algorithm was introduced in L'Ecuyer and Stephens (2002) and applied to CloudSat in Mitrescu et al. (2010). At its core, the algorithm is an optimal estimation technique applied to the difference between the observed reflectivity profile and a simulated model of the microphysical drop size distribution. Lebsock and L'Ecuyer (2011) introduced refinements to this algorithm focused on warm rain by including a more representative drop size distribution and specifically treating attenuation by cloud water. Together, 2C-PRECIP-COLUMN and 2C-RAIN-PROFILE can be used to gauge newly developed precipitation algorithms given their direct comparison on CloudSat footprints and efforts for validation (e.g. Ellis et al., 2009, Smalley et al., 2014).

2.1.2 WALRUS

WALRUS is a Bayesian algorithm that retrieves latent heating and other microphysical information in oceanic warm rain systems (Nelson et al., 2016). WALRUS is built on a database of cloud-resolving model simulations of oceanic warm rain systems (Saleeby

et al., 2015). Model simulations are sampled and run through a reflectivity simulator (Haynes et al., 2007) to provide a pool of model profiles analogous to observations (Nelson et al., 2016).

Profiles of CloudSat reflectivity are screened 1) for clouds and rain that exist solely below the freezing level available from 2C-PRECIP-COLUMN and 2) that rain is present in the column as indicated by a reflectivity of at least 0 dBZ occurring in the profile; this reflectivity threshold is the estimated backscatter from a profile precipitating at a rate of 0.03 mm hr^{-1} (Haynes et al., 2009). If both of these of criteria are met, the profile is then matched to similar profiles in the database using characteristics of the reflectivity profile that describe intensity (PIA, path integrated reflectivity, and near-surface reflectivity) and vertical extent (cloud top height, rain top height, and maximum reflectivity height) to provide an *a posteriori* distribution of database states. Because the retrieval relies on PIA as an input parameter, WALRUS can only retrieve where those are available from CloudSat, namely over the oceans.

Errors assumed in the Bayesian scheme are in line with instrument uncertainties (1 dB) or algorithm resolution (300 m) and off-diagonals of the covariance matrix are scaled by the correlation between parameters. The weighted mean of this output distribution is the mean retrieval state and variance is indicated by the weighted spread in the distribution.

Chiefly among the products available from WALRUS is the full profile of latent heating extending down to the surface. Here, the model is used to fill in information below the

cloud that is missed by the blind zone in reflectivity below 1 km. The latent heating and cooling is the byproduct of condensational and evaporational processes that are retrieved to be occurring in the profile and come from the five minute integrated accumulation by the model. Other microphysical information retrieved includes surface rainfall rate, profiles of vertical velocity, liquid water path, mean diameter of hydrometeors, and others available from the model. Figure 2.1 highlights the warm rain component of a CloudSat orbit section taken on April 17, 2007. A range of warm rain types are present, ranging from storms extending a few kilometers in height with intense precipitation rates down to lightly raining and shallow clouds. The vertical extent of reflectivity is reflected in retrieved vertical profiles of latent heating and hydrometeors, indicating the algorithm can distinguish atmospheric states of different heights and types. Another indication of physical information communicated through the retrieval is the vertical distribution of the hydrometeors: areas of higher surface rainfall rates have more and larger drops close to the surface compared to those that are not. In any case, this demonstrates the retrieval can retrieve a spectrum of warm rain regimes in a variety of locations.

2.1.3 TRMM

TRMM was a satellite equipped with a package of instruments for precipitation sensing including the Ku-band (13 GHz) Precipitation Radar (PR), TRMM Microwave Imager (TMI) with 5 channels (4 having dual-polarization), and visible and infrared scanner (VIRS) (Kummerow et al., 2000). Unlike CloudSat's CPR, TRMM's PR was a cross track scanning system, meaning the radar took observations not only pointing straight

down to the surface but also to the side of the track at an angle to generate a swath width in excess of 200 km. The PR horizontal resolution was about 4 km and the vertical resolution 250 m, both of which increased when moving away from nadir. Minimum detectable reflectivity was higher than CloudSat at 18 dBZ and surface clutter could mask the signal for up to 1.6 km at side angles (Heymsfield et al., 2000).

TRMM was launched in 1997 at a 350 km orbit height with an approximate 35^{o} inclination in a precessing orbit, but the height was soon increased in 2001 by about 50 km to prolong the mission (e.g. DeMoss and Bowman, 2007). The maneuver was successful and TRMM continued to orbit until reentry in 2015 (NASA Orbital Debris Program Office, 2015). Like CloudSat, TRMM products include the radar reflectivity and path integrated attenuation (Product 2A21), PR precipitation classification (2A23), and both rainfall estimates and vertical drop size distribution profiles available from the PR, TMI, and combined PR/TMI (2A12, 2A25, and 2B31, respectively) (Kummerow et al., 2000).

2.1.4 SLH

As previously discussed, SLH is a latent heating algorithm that uses radar data from TRMM and more recently GPM. The core algorithm technique SLH employs is a spectral lookup table based on two-dimensional cloud resolving model simulations (Shige et al., 2004). Characteristics of the reflectivity profile that are used in the retrieval are the precipitation classification, precipitation top height, the precipitation rate at the freezing/melting level, and the precipitation rate at the surface. Output from SLH is

a vertically-resolved profile of latent heating and $Q_1 - Q_R$ (Shige et al., 2004). SLH is just one of the latent heating datasets available from TRMM but is most similar to the retrieval scheme in WALRUS.

2.1.5 GPCP

A rainfall measurement independent of the radar-based estimates of WALRUS and TRMM is the Global Precipitation Climatology Project (GPCP). GPCP was established under the auspices of the World Climate Research Program to provide a merged global rainfall dataset with a long term record (Huffman et al., 1997). Observations from satellite and surface based instruments are included in GPCP estimates. Microwave sensor estimates of precipitation are used to train geostationary infrared observations that have greater global coverage, and the merged estimates are then calibrated with rainfall gauge estimates (e.g. Adler et al., 2003, Huffman et al., 1997, 2009). While GPCP provides excellent temporal and spatial coverage, estimates over the ocean from passive instruments and without rain gauge calibration may miss some warm rain that falls from clouds close to the surface (e.g. Rapp et al., 2013).

2.2 Atmospheric state

Reanalysis data is employed to provide information about the general atmospheric state. In general, reanalysis data is generated by modeling centers using a model dynamical core that is forced by assimilated observations from a variety of sources. NASA's Modern

Era Retrospective-analysis for Research and Applications (MERRA) is used in this study. MERRA uses the Goddard Earth Observing System version 5 dynamical core with its associated three-dimensional variational data assimilation scheme (Rienecker et al., 2011). Though reanalyses provide global data, they are not wholly perfect just like any dataset that does not observe the planet at every point at every point in time with complete accuracy. In particular, some deficits are noted in regards to implied energy transport (Appendix A) and radiative-precipitation efficiencies (Daloz et al., 2017). Nevertheless, the variables used in this analysis are reliant mostly on state variables and are used as a best guess of the general environment.

Because MERRA provides temperature, water vapor, and vertical motion information, it can supply large-scale environmental properties. A few of these variables will be used to aid in this investigation. The first is relative humidity at 700 mb (RH_{700}), which is a measure of the water vapor pressure at 700 mb compared to the saturation vapor pressure. Using a measurement at 700 mb in the tropics allows for measurement of the free tropospheric humidity, as opposed to near surface measurement like those from ground stations.

A second variable from MERRA to be used is the vertical motion at 700 mb (ω_{700}). Given in pressure coordinates, the vertical motion supplies information about the large-scale movement of the atmosphere. Areas that are generally sinking or subsiding will be indicated by positive vertical motion values, while areas of large scale ascent will show

negative.

The final parameter used from MERRA is the estimated inversion strength (EIS) as defined in Wood and Bretherton (2006). Rather than a simple measure of the large-scale environment, EIS informs about the atmosphere's thermodynamic structure in the lower atmosphere. It relies on two components: the local tropospheric stability (LTS; Klein and Hartmann (1993)) and information about the local temperature using a mean level moist adiabatic lapse rate (Γ_m). LTS is defined as

$$LTS = \theta_{700} - \theta_0, \tag{2.1}$$

or the difference in potential temperature between the surface (0) and the free troposphere (700 mb). EIS is defined as

$$EIS = LTS - \Gamma_m^{850}(z_{700} - LCL), \tag{2.2}$$

where z_{700} is the 700 mb height and LCL is the lifting condensation layer height.

2.3 Methodology

Global analyses in Chapter 3 and regional analyses in Chapter 4 will both use a gridded WALRUS dataset with a horizontal resolution of 2.5° by 2.5°. This dataset is generated by binning WALRUS retrievals monthly over the January 2007 to December 2010 period.

Two different means are used to answer different parts of the questions to be investigated in this analysis. The first is a monthly mean and the second is a four year conditional mean.

The monthly mean may be considered an accumulation of a quantity or an "unconditional" mean. It is calculated as follows: the retrieved variables in a given month are summed and divided by the total number of CloudSat observations, irrespective of whether a retrieval is performed. Unless otherwise stated, each month is then averaged across the four year time period to yield a four-year mean annual cycle that is then averaged by weighting each average month by the days in that month, i.e.

$$\overline{x} = \sum_{i=1}^{12} x(i) * n_{\mathrm{m}}(i) / \sum_{i=1}^{12} n_{\mathrm{m}}(i), \tag{2.3}$$

where x is a given variable and n_{m} is the number of days in a given month. The result provides the monthly mean accumulation of heating, surface rainfall, or another variable.

Conditional means are calculated to examine the behavior strictly of the retrieval, as opposed to the total accumulation or contribution of the physical values. These means are calculated by summing all retrievals over the course of the four year time period and divided by the number of retrievals included in that sum, i.e.

$$\overline{x} = \sum_{i=1}^{np} x(i) / n_{\mathrm{p}}, \tag{2.4}$$

where n_{p} is the number of WALRUS profiles retrieved over the four years.

MERRA data used in Chapters 3 and 4 is similarly gridded to a 2.5° by 2.5° resolution but is taken only where WALRUS retrievals occur. To obtain the MERRA value from its native approximately 0.5° resolution for a given profile bin, a nearest-neighbors approach is used (Smalley and L'Ecuyer, 2015). Since variables from MERRA are those describing the atmospheric state, only conditional averages are taken to yield the average state during WALRUS retrievals.

Two different datasets derived from TRMM SLH are used in Chapter 5 analysis. The first is a pre-gridded dataset at a 2.5° by 2.5° horizontal resolution. Because TRMM's orbit extends only into the subtropics, WALRUS data is restricted to a similar region in this analysis. The second is a granule level dataset gridded to 0.5° by 0.5° horizontal resolution.

SLH separates out retrievals based on different regimes including convective, shallow stratiform, and convective stratiform (e.g. detraining anvil). WALRUS does not separate regimes explicitly in its retrieval, but is designed only for warm rain–rain that is shallow and often stratiform. This presents an opportunity to merge the two datasets by retaining only convective and convective stratiform latent heating components from SLH and including WALRUS warm rain estimates to create a complete regime-spanning latent heating dataset. Some understimation may still occur in cases where warm rain resides wholly in the blind zone of CloudSat near the surface.

2.3.1 Locations of regional analysis

A variety of locations are selected for study in Chapter 4, some based on prior studies and others due to their general circulation regime. Figure 2.2 illustrates the areas selected across the globe. The first region is taken from the Cloud Feedback Model Intercomparison Project–Global Atmospheric System Studies Intercomparison of Large Eddy Models and Single Column Models (CGILS; Zhang et al. (2013)). CGILS is a coordinated effort of detailed eddy simulations and observations focused on three domain boxes that span from the coast of California in the United States to near the islands of the state of Hawai'i. Other observing field campaigns have taken place in this region as well, such as MAGIC (Zhou et al., 2015) and FIRE (Albrecht et al., 1988). Given that the transition from stratocumulus to shallow cumulus is an area of active investigation in climate models, benchmarks of the heating in these regions are important.

Another zone is the Variability of the American Monsoon Systems Ocean-Cloud-Atmosphere-Land Study Regional Experiment (VOCALS-REx; Mechoso et al. (2014)). VOCALS took place off the coast of Chilé in South America providing highly detailed observations of the stratocumulus in the region. The transect for this area is taken to be a successive group of boxes moving westward off the coast of the continent to capture changes in cloud morphology or behavior that may occur.

Five boxes are selected to directly match part of the analysis of Klein and Hartmann (1993), namely the subtropical marine stratus regions off western coasts of most of the

continents. In the Northern Hemisphere, that includes off the California coastline, partially overlapping with the CGILS area, and near the Canary Islands. The Canary Islands box is five degrees south of the California but half of their area is in the same zonal belt. Southern Hemispheric boxes are selected off the west coasts of Peru, Namibia, and Australia. The Peru and Namibia boxes are in the same zonal band, while the Australian is further south than both.

An Atlantic Ocean transect is selected from the Azores to Barbados. This area has been subject to a variety of field campaigns spanning parts of this transect (Augstein et al., 1974, Holland and Rasmusson, 1973, Rauber et al., 2007). Longer term observations in this part of the world are also available from the ground. The Barbados Cloud Observatory (Stevens et al., 2016) was established at one end of the transect in Barbados and the other end was home to a Department of Energy Atmospheric Radiation Measurement Mobile Facility on Graciosa Island for nearly two years (Rémillard et al., 2012). Finally, two sections across the Intertropical Convergence Zone (ITCZ) are chosen that span the areas of the Pacific Ocean from Back and Bretherton (2006). These areas will examine specifically the interbasin differences in the Equatorial Pacific where both are embedded in regions of tropical convection.

These data sources, both observational and from reanalysis, provide the necessary components required to answer the aims of this work. Namely, CloudSat and TRMM algorithms supply process-level information through latent heating across all regimes of

precipitation. Reanalyses inform on the environmental conditions present surrounding precipitation. And the WHI serves as a metric for estimating the state of the MJO.

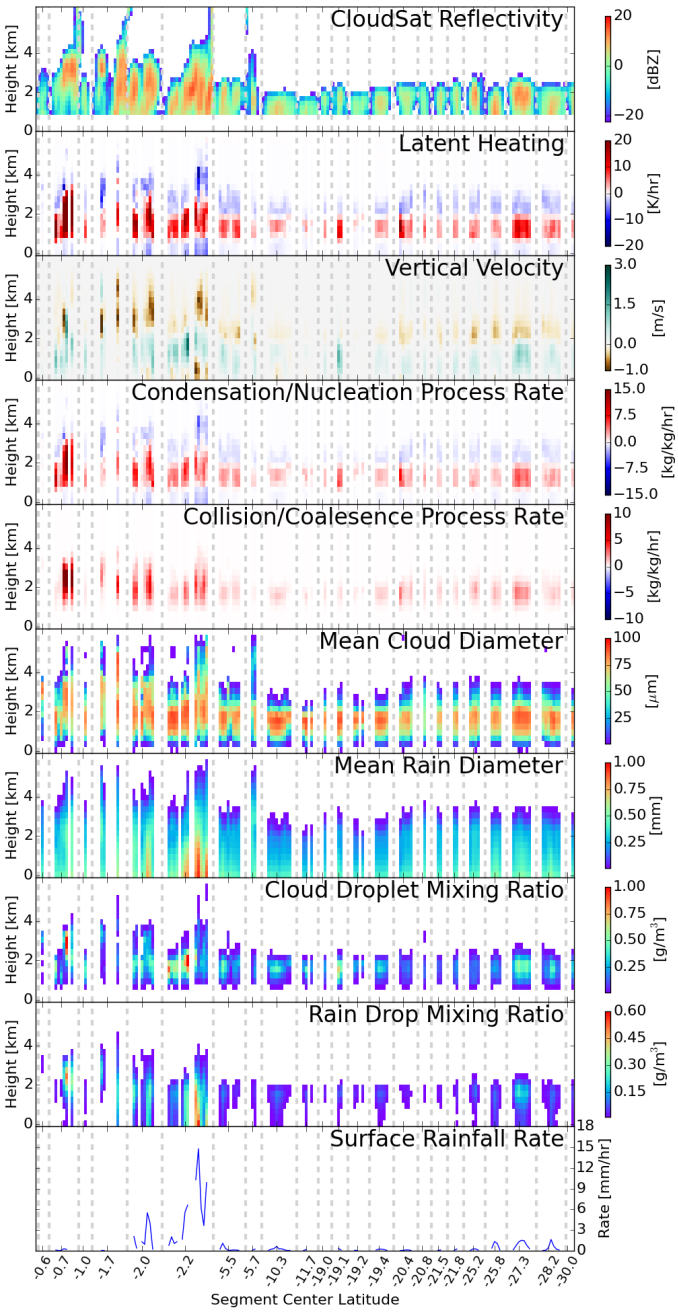

FIGURE 2.1: Example WALRUS retrieval on part of CloudSat granule #05151 showing the algorithm outputs available. Segments where more than five profiles are not retrieved are truncated (indicated by gray dashed lines) for easier viewing. The top panel shows the CloudSat reflectivity used as input for the algorithm and subsequent plots display latent heating (positive values condensational heating, negative values evaporative cooling), vertical velocity (positive values up, negative values down), condensation process rate (positive values condensation, negative values evaporation), collision and coalescence process rate, cloud mean diameter, rain drop mean diameter, cloud droplet mixing ratio, rain drop mixing ratio, and surface rainfall rate.

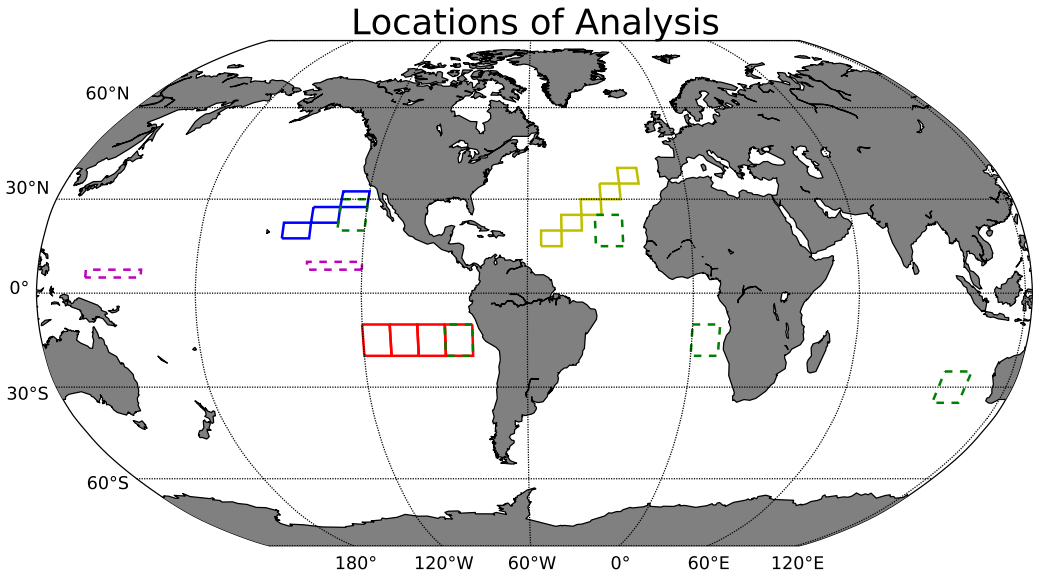

FIGURE 2.2: Global map of locations selected for regional latent heating analysis in Chapter 5.

Chapter 3

Global Analysis*

3.1 The global distribution of warm rain

The monthly mean global distribution of warm rain accumulation derived from WALRUS is shown in Figure 3.1(a). The warm rain components of large-scale features like the Intertropical Convergence Zone (ITCZ) are clearly present. Though the ITCZ is often visualized as a band of tall convection owing to its signature in infrared observations, WALRUS is able to demonstrate that it is comprised of convection of different shapes and sizes at various stages in their lifecycles. Some of the warm rain–particularly in convective areas–captured by WALRUS may eventually evolve to include an ice phase component, but at the observation time it had not yet glaciated and precipitation was still being generated through warm rain processes.

* This chapter is under review in the *Journal of Geophysical Research: Atmospheres*.

Mean warm rainfall amounts peak near 0.1 mm hr^{-1} just north of the Equator in the Pacific Ocean. Eastern ocean basin regions that coincide with the descending branch of the Hadley Cell and coastal upwelling also support higher warm rain accumulations with values ranging from 0.01 to 0.05 mm hr^{-1}. Overall, warm rain contributes 0.011 mm hr^{-1} (0.26 mm day^{-1}) of accumulation over the global oceans.

The frequency of WALRUS retrievals from all profiles that CloudSat observes is documented in Figure 3.1(b). The highest sampling, nearly 8% of all observations, occurs off the western coast of South America. With the exception of the Equatorial region in the West Pacific Ocean Basin, observations are favored in areas of the descending branch of the Hadley Cell in both the Northern and Southern Hemispheres. Fractions tail off moving poleward as more precipitation falls from mixed phase precipitation processes that reached the freezing level. Some areas that are precipitating at a rate less than drizzling (0.01 mm hr^{-1}) may not be captured by the 0 dBZ required threshold which could skew these occurrences lower than reality.

The average intensity of warm rain, or conditional mean warm rain rates, are presented in Figure 3.1(c). Warm rain intensities are more uniform than the mean accumulations in Figure 3.1(a), averaging 0.5 mm hr^{-1} in many locations with areas of enhanced instantaneous rain rates exceeding 1 mm hr^{-1} north of the Equator in the Pacific Ocean basin. In upwelling regions along the west coasts of the continents and along the equator, conditional rain rates are locally depressed where the stratocumulus decks are most

prevalent.

Comparing the rainfall rate distribution retrieved from WALRUS against GPCP (Fig. 3.1(d)), warm rain explains 9.2% of the total GPCP rainfall accumulation over the oceans. Subsidence regions in the eastern ocean basin regions are almost entirely comprised of warm rain. Restricting to the area between the 50° latitudes, the average WALRUS percentage of warm rainfall over the oceans is 11.0%. Further restricting the averaging area to the tropics bounded by 25° latitudes yields the percentage of warm rainfall over the oceans is 13.9%. The percentage grows when focusing on the tropical regions because warm rain fractions are near zero in the midlatitudes and polar regions indicating that cold precipitation processes dominate in these areas.

It should be noted that the requirements for defining warm rain in WALRUS are more conservative than those applied in the CloudSat 2C-PRECIP-COLUMN algorithm (Haynes et al., 2009). The latter often considers profiles labeled *rain probable* as likely containing drizzle, but Figure 3.1(e) indicates that WALRUS does not currently include some of these drizzling profiles. Future latent heating estimates may need to consider lightly drizzling and non-precipitating scenes to fully capture the effects of condensation and evaporation on the vertical structure of atmospheric heating in warm rain.

To illustrate that the RAMS database does not introduce large biases in WALRUS warm rain retrievals, the estimates in Figure 3.1(c) are compared with those obtained from 2C-RAIN-PROFILE in Figure 3.1(f). WALRUS retrieves slightly higher rainfall rates in

the north- and southeastern ocean basins than the 2C-RAIN-PROFILE product while rates in the Equatorial ocean basins are lower. Globally, WALRUS warm rain estimates are 12.1% lower than the 2C-RAIN-PROFILE algorithm over the oceans.

Though warm rain is present over much of the globe's oceans, liquid clouds exhibit widely varying characteristics as evidenced in part by the variation in rain rate. Both stratocumulus decks and shallow convection produce warm rain but they form in different large-scale environments that dictate their evolution. It can be expected that these two cloud types will have different latent heating profile characteristics since their vertical extents and intensities are different. To better distinguish these distinct warm rain regimes, we introduce a simple classification based on WALRUS retrievals of in-cloud vertical velocity: profiles with a retrieved maximum vertical velocity greater than or equal to 1 m s^{-1} are considered "shallow convective" or, simply, convective warm rain and profiles with a maximum vertical velocity less than 1 m s^{-1} are stratiform warm rain.

This follows the generalized definition defined by Yuter and Houze Jr. (1995) who defined convective conditions to occur when vertical velocity exceeds $\sim$1-3 m s^{-1}. The partitioning of retrieved profiles between these categories is shown in Figures 3.1(g) and (h). Convection is most frequently observed in the ITCZ as well as along the eastern coast of the Asian continent. Globally, convective constitutes only about 11% of all warm rain occurrences but it comprises 36% of warm rain accumulation.

3.2 Global latent heat release in warm rain processes

3.2.1 Spatial distributions

Given its consistency with existing rainfall products, WALRUS provides an ideal resource for quantifying the global distribution of latent heating owing to warm rain processes. Mean vertically resolved profiles of latent heating and cooling are column pressure weighted based on a standard atmosphere to yield the monthly mean column-integrated latent heating by warm rain shown in Figure 3.2(a). Over the world's oceans, the average latent heating and cooling combined is 0.15 K day^{-1}. It is apparent that warm rain contributes to atmospheric heating nearly globally. Like the distribution of global mean warm rain, the largest contributions of latent heating from warm rain are found in the ITCZ, reaching nearly 1 K day^{-1} in the East Pacific, with lower maxima occurring in the subsidence regions of all major ocean basins. Regions immediately off the coasts in the East Pacific and Atlantic Oceans that are characterized by stratus decks exhibit local minima in total heating and cooling. Small amounts of warm rain latent heating from postfrontal warm systems are also retrieved in areas extending into the midlatitudes, but the fraction of rain at these latitudes originating from warm rain processes is low (Fig. 3.1(d)).

The components of the average latent heating profiles owing to condensation and evaporation processes are separated in Figures 3.2(b) and (c). Notwithstanding differences in

environmental conditions, the presence of more heating in a column (Fig. 3.2(b)) generally means there is more column liquid water that can be evaporated (Fig. 3.2(c)). Evaporation may exceed the rate of condensation due to entrainment at the cloud top or sides, which is the process by which clouds are eroded through mixing with dry environmental air (Wood, 2012). Additionally, as rain falls from the base of the cloud toward the surface, it encounters drier environmental air that evaporates raindrops. An extreme example of the latter case is virga, a phenomenon that occurs when precipitation is completely evaporated prior to reaching the surface.

This ability to separately diagnose heating and cooling regions using WALRUS provides additional insights into the relative importance of specific processes in warm rain scenes. Figure 3.2(d) shows the ratio of cooling below the cloud from rain evaporation to cooling above the condensation layer from entrainment by further separating the cooling from Figure 3.2(c). It should be noted that the separation into below and above condensational layer heating is only generated when heating exists within one contiguous layer. Wyant et al. (1997) found that modeled stratocumulus evolved into trade cumulus when SST was increased due to a moistening of the boundary layer. This is generally in line with other studies of the stratocumulus to cumulus evolution (e.g Sandu and Stevens, 2011, Tsai and Wu, 2016). A similar pattern is evident here as the ratio of evaporation to entrainment decreases as one moves westward away from the eastern coastal regions, where clouds transition from stratocumulus to shallow trade cumulus. Careful examination of evaporation below cloud and entrainment separately (not shown) suggests that

this decreased ratio is caused primarily by enhanced rain evaporation to heating near the continents, while the higher ratios in the Western Pacific ITCZ are the result of less entrainment compared to heating.

3.2.2 Vertical structure of heating

Differences in the magnitude of cooling processes below and above the heating layer in Figure 3.2(d) hint at variations in the vertical structure of latent heating and cooling in warm rain across the globe. In Figure 3.3, the structure of the mean latent heating profile is shown for boxes in the East Central Pacific (5°S-5°N, 100°W-95°W) and the Southeastern Pacific (20°S-15°S, 100°W-95°W). Profiles are separated into convective and stratiform regimes as described before and both the four year conditional averages and total monthly means are shown. Focusing first on the East Central Pacific, convective latent heating profiles are more intense and vertically developed than stratiform profiles (Fig. 3.3(a), left side). But, because convective profiles occur about 10% of the time in this region over the four years, stratiform profiles tend to dominate the occurrence-weighted mean (Fig. 3.3(a), right side).

Figure 3.3(b) shows that there is significant regional variability in the relative importance of convective and stratiform warm rain even in the same longitude stripe but displaced to the south in a subsidence region. The fraction of retrieved profiles classified as convective decreases from 10% to 4%, which is reflected in a decreasing relative contribution to the mean latent heating profile in spite of the conditionally larger heating retrieved in

convective profiles. Yet another factor in the difference in the average profile for all regimes between these two regions is the fact that the absolute occurrence of warm rain is nearly triple that observed in the East Central box owing to the increased prevalence of warm rain in that area. Nevertheless, stratiform regime profiles are still more prevalent and therefore exert a stronger influence on the mean warm rain latent heating structure for both regions based on the separation criteria here.

A comparison of each regime's relative contribution to the vertical structure of latent heating is examined on the global scale. Figure 3.4 shows the global mean latent heating and cooling distributions in 900-m thick layers by averaging three algorithm layers together, starting near the ground and extending upwards. A strength of the Bayesian approach used in WALRUS is that it is less affected by ground clutter that obscures satellite observations below 1 km; parameters observed above the clutter region are used to extrapolate information down to the ground using the database. This is especially highlighted in the lowest layer, where boundary layer cooling due to rain evaporation dominates the globe. The layer between 0.9 and 1.8 km above the ground approximately corresponds to the layer of strongest condensational heating. The 1.8-2.7 km layer begins to differentiate warm rain regimes: cooling is prevalent in the stratus decks in upwelling coastal regions in eastern ocean basins as well as in the midlatitudes, while trade cumulus in the ITCZ and SPCZ still exhibit latent heating associated with hydrometeor formation and growth at this height. All regions are characterized by cloud top evaporation in 2.7-3.6 km with cooling replacing any of the areas of heating from the layer below. Weak

cloud top cooling remains in only some of the taller warm rain regions between 3.6-4.5 km, and by 4.5-5.4 km cloud top cooling is only realized in Equatorial warm rain.

The vertical structures of heating from convective and stratiform warm rain are compared more directly in Figures 3.5 and Figure 3.6. Convective profiles exhibit less evaporative cooling below the cloud base in 0-1 km compared to the analogous stratiform profiles. The convective profiles also contribute more condensational heating from 1.8-2.7 km and lack the presence of a heating–cooling dipole across ocean basins. Cooling at upper levels is also lower in magnitude in the convective cases due to the lower frequency of occurrence. Averaged layers from stratiform profiles still show some dipole character, possibly due to the stringent velocity requirement taken in the classification that may still allow some convective profiles to be classified as stratiform. Nevertheless, these characteristics describe general differences in the character of the processes retrieved between these two different regimes that have been defined by the retrieved vertical velocity. This fact is further reflected in the difference in latent heating contribution between the regimes, as the mean column integrated latent heating contribution from convective rain is 0.078 K day^{-1} while that from stratiform rain is 0.076 K day^{-1}.

3.2.3 Seasonal cycle

It has previously been documented that stratus clouds in the subtropics exhibit a seasonal cycle, generally peaking in coverage in the season of highest thermodynamic stability (Klein and Hartmann, 1993). To examine whether a similar variation exists in warm

rain latent heating over the course of the seasonal cycle. The zonally averaged oceanic distribution of warm rain column latent heating is decomposed into seasons in Figure 3.7. The zonal distribution of the yearly mean and most seasons shows the greatest heating north of the Equator with a local minimum just south of the Equator. The distribution of heating is asymmetric between the hemispheres with larger values occurring in the subsidence regions in the winter hemisphere. For transition seasons of spring and fall in the subtropics, the Southern Hemisphere contributes a larger magnitude of latent heating. Nevertheless, the overall pattern favors the subtropics and just north of the Equator as areas of largest heating throughout the year implying that the general circulation is a strong influence on where the warm rain occurs.

Each hemisphere respectively exhibits a pattern in the seasonal cycle. While the subtropics peak in the winter, the higher latitudes peak around the summer months. This is likely the case because the warm summer clouds over the ocean contributed by baroclinic cyclones are replaced by cold winter precipitation at these latitudes. In both hemispheres, the seasons that are favored to reach a maximum reverse at around the 30^{o} part, appearing to coincide with edge of the Hadley cell in the general circulation.

3.3 Environmental drivers

The preceding climatologies can be used to evaluate the current representation of warm rain processes in models. But, to offer a pathway toward improving model physics, the responses of warm rain processes to environmental drivers must be quantified. Previous

studies have suggested that environmental stability metrics serve as good predictors for cloud cover and type in both models (Bretherton et al., 2013, Chung and Teixeira, 2012) and observations (Klein and Hartmann, 1993, Larson et al., 1999, Sun et al., 2011, Wood and Bretherton, 2006). It can then be expected that the processes by which these clouds are ultimately generated should similarly be constrained by the environmental stability.

3.3.1 Distributions of environment and (in)stability

Monthly averaged values of three MERRA environmental parameters conditionally sampled to retrieved WALRUS scenes are shown in Figure 3.8 on the left with associated standard deviations on the right. All three indicators exhibit similar behaviors to a first order given that they all provide a measure of climatic regime. Values of RH_{700} (Fig. 3.8(a)) are lower in the subsiding regions of the Hadley cell extending from the eastern ocean basins Equator- and westward. Higher humidities are present just north of the Equator across the globe, extending south from the Equator in the West Pacific Ocean, and in northwestern ocean basins. ω_{700} (Fig. 3.8(c)) shows a similar distribution of subsidence in the areas containing lower humidity and large-scale ascent collocated with areas of higher humidities. EIS (Fig. 3.8(e)), which is calculated as introduced in Section 2.2, follows the pattern of higher stability in subsiding regions and lower stability in convective regions. While these variables all share a similar pattern, EIS has the most consistent variability outside the Equatorial region (Fig. 3.8(f)).

3.3.2 Instability and cloud processes

To better understand the impact of these environmental drivers on the latent heating profiles, we next examine mean profiles of evaporative cooling and condensational heating over the range of each parameter. Figure 3.9 shows how the mean structure of latent heating and cooling vary as a function of MERRA RH_{700}, ω_{700}, and EIS. Increased relative humidity aloft shows taller cloud extents, while a drier upper atmosphere has a shallower top with stronger evaporative cooling (Fig. 3.9(a)). ω_{700}, describing vertical motion, compresses the vertical depth of the profile (Fig. 3.9(b)). As the vertical motion intensifies, indicating stronger subsidence, the layer becomes more compressed vertically. EIS encapsulates these behaviors of a decrease in the cloud height extent, a decrease in heating, and a decrease in cooling with increasing EIS as well (Fig. 3.9(c)). These relationships broadly follow theoretical models of cloud-topped boundary layers (e.g. Lilly, 1968, Stevens, 2002), that boundary layer depth is a function of entrainment and vertical motion. Yet in each of these cases, the height of maximum heating seems to be less variant than the cooling layer.

To describe changes in the overall character of the latent heating relationships with stability, joint histograms of maximum cooling height, cloud top cooling thickness, evaporation below to above ratio, maximum heating height, and heating thickness with EIS are synthesized in Figure 3.10 on a monthly timescale. The behavior of some of these parameters is as expected. Increased stability yields a decreased height of maximum cooling (Fig.

3.10(a)), a narrower cloud top cooling thickness (Fig. 3.10(b)), increased relative importance of evaporation below cloud base compared to entrainment above the heating layer (Fig. 3.10(c)), and some narrowing of the condensation layer thickness (Fig. 3.10(e)). These behaviors show an increase in stability prevents rain systems from expanding in height, generally following models of cloud-topped boundary layer evolution as before. Somewhat surprisingly, however, the height of maximum latent heat release in condensation appears to be remarkably invariant to changes in stability (Fig. 3.10(d)). Globally, the height of maximum condensational heating in warm rain is 1.5 +/- 0.6 km, independent of stability.

The separation of these parameters for the two different warm rain regimes reveals different but related behaviors (Fig. 3.10, right side). Convection with stronger updrafts ostensibly extend the convective plume to a higher vertical level compared to stratiform, increasing the thickness of the condensation layer. By spreading the condensation higher into the atmosphere, the height of maximum entrainment is displaced higher and the depth of entrainment decreases due to the intruding condensation. With a reduction in entrainment, its efficiency compared to evaporation below the cloud base is reduced and convective clouds have higher evaporation to entrainment ratios than stratiform.

Therefore, we see that the environment plays a strong role–in depth and in placement–of the evaporative cooling characteristics, as does the warm rain regime, while the level of maximum latent heating is nearly constant even among differing regimes (Fig. 3.10(d)).

Large eddy simulations (LES) compiled in Blossey et al. (2016) for the CFMIP/GASS Intercomparison of Large eddy and Single column models also show that, even in a $4xCO_2$ perturbation simulation, the vertical distribution of the heating in precipitating shallow cumulus are somewhat invariant on a long time scale. This may be an important characteristic of warm rain that is captured by both climate models and observations that warrants further observation and exploration on smaller spatiotemporal scales in the future.

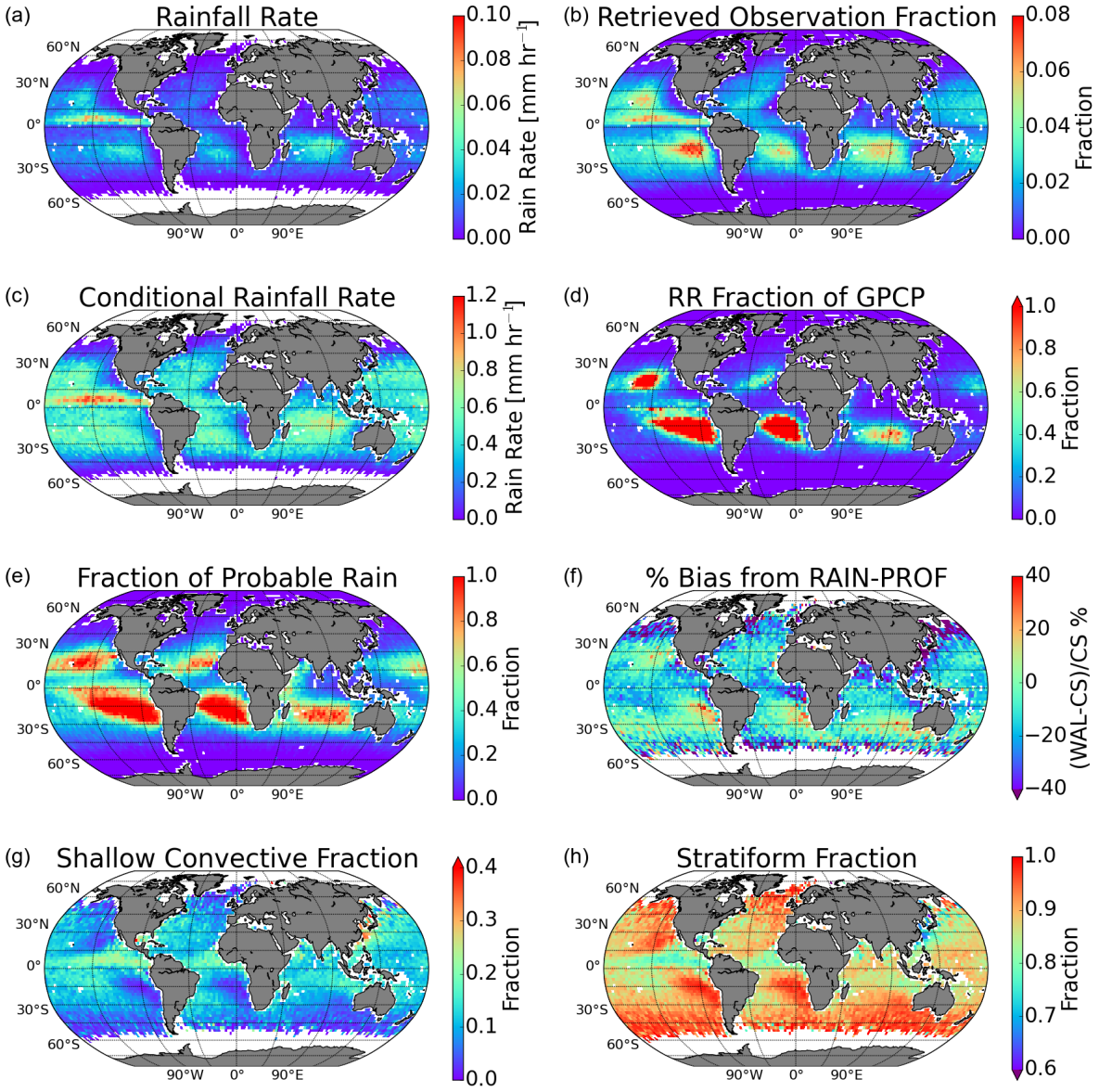

FIGURE 3.1: (a) Monthly average warm rainfall accumulation. (b) Fraction of all observed CloudSat profiles retrieved as warm rain for this time period. (c) Conditionally averaged warm rainfall rate. (d) Fraction of average GPCP monthly rainfall accumulation contributed by warm rain. (e) Fraction of probable rain profiles according to 2C-PCP-COLUMN that are retrieved as warm rain by WALRUS for this time period. (f) Monthly average bias percentage of WALRUS conditional rainfall from 2C-RAIN-PROFILE CloudSat product. Fraction of retrieved profiles classified as (g) "shallow convective" and (h) stratiform in this study.

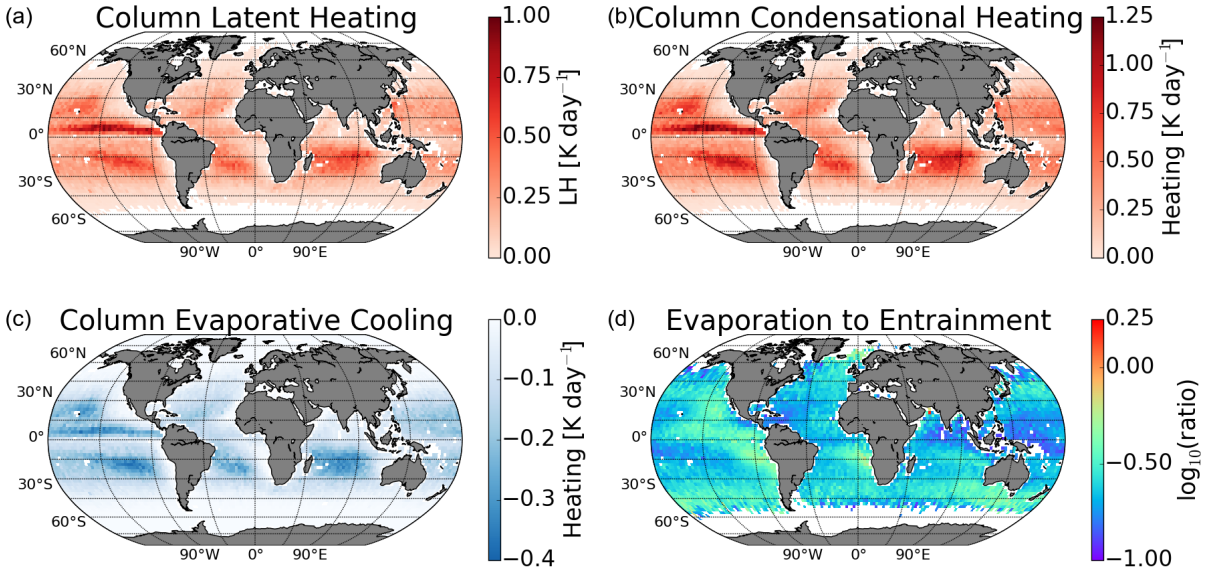

FIGURE 3.2: Global distributions of monthly averaged warm rain processes. (a) Column latent heating from condensation and evaporation. (b) Column latent heating from condensation only. (c) Column latent cooling from evaporation and entrainment only. (d) Ratio of cooling below to cooling above the heating layer.

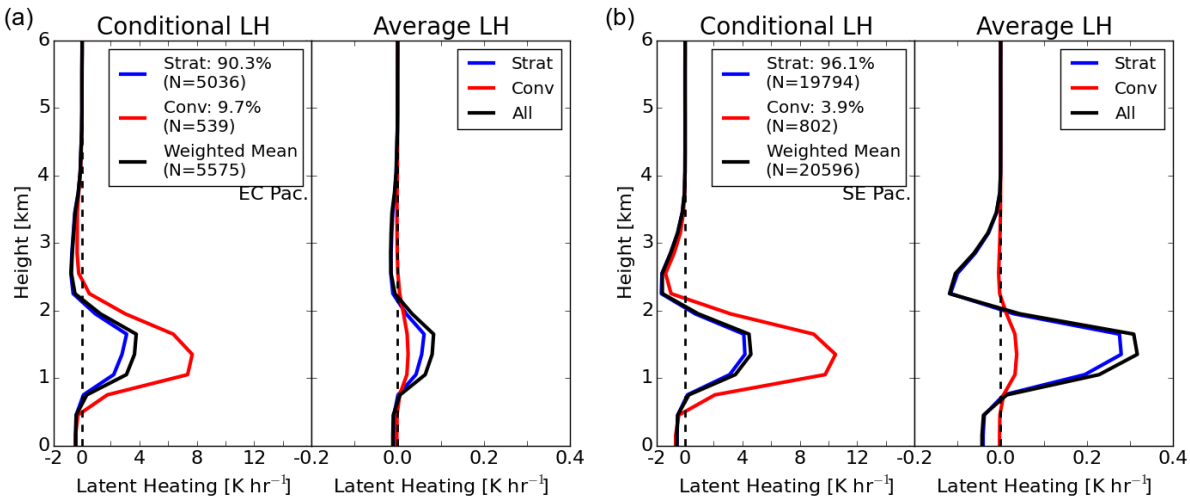

FIGURE 3.3: Profiles of latent heating taken as a four year conditional average of retrievals (left) and as the monthly mean over all observations (right) for (a) a box over the East Central Pacific (5°S-5°N, 100°W-95°W) and (b) a box over the Southeastern Pacific Ocean (20°S–15°S, 100°W–95°W). Conditional plots include a weighted mean based on the regime frequencies of occurrence shown in the legend, while average plots show the total contribution by both regimes.

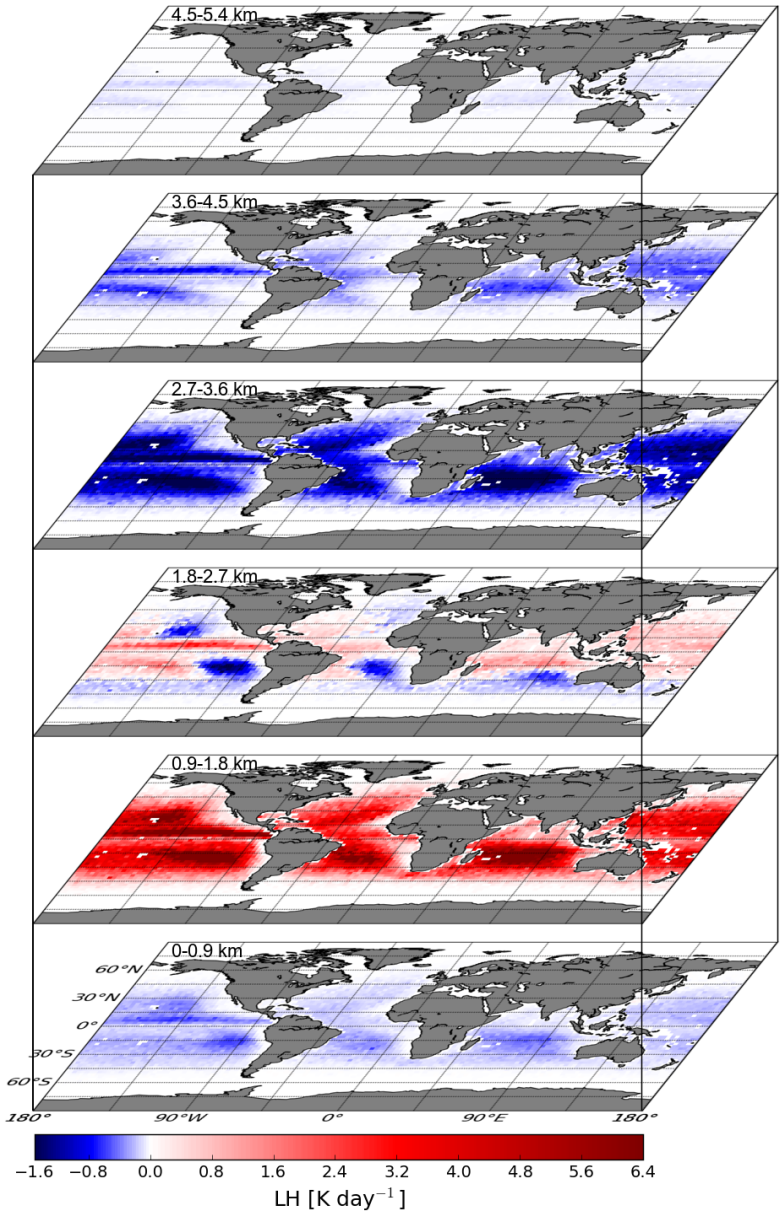

FIGURE 3.4: A vertical cross section of the mean monthly global latent heating distribution averaged in approximately one kilometer layers.

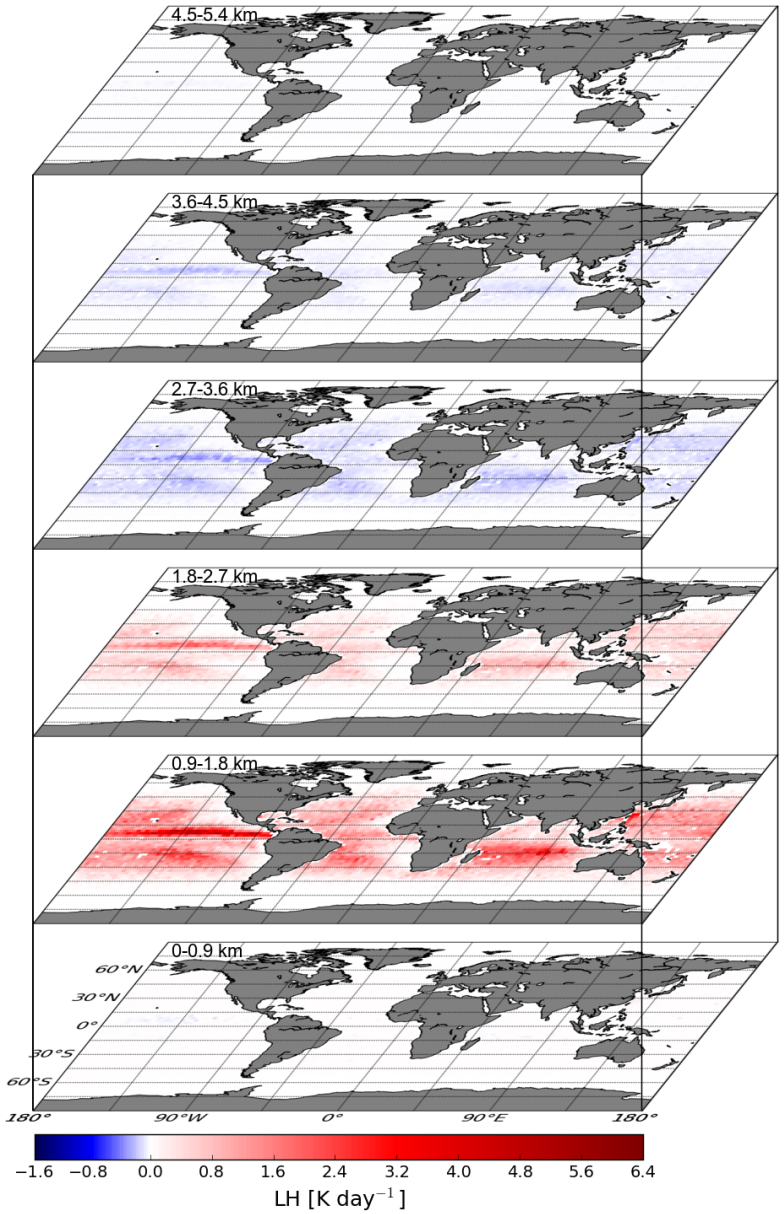

FIGURE 3.5: As in Figure 3.4 but only for profiles with a maximum vertical velocity greater than or equal to 1 m/s representing regimes more characteristic of convection.

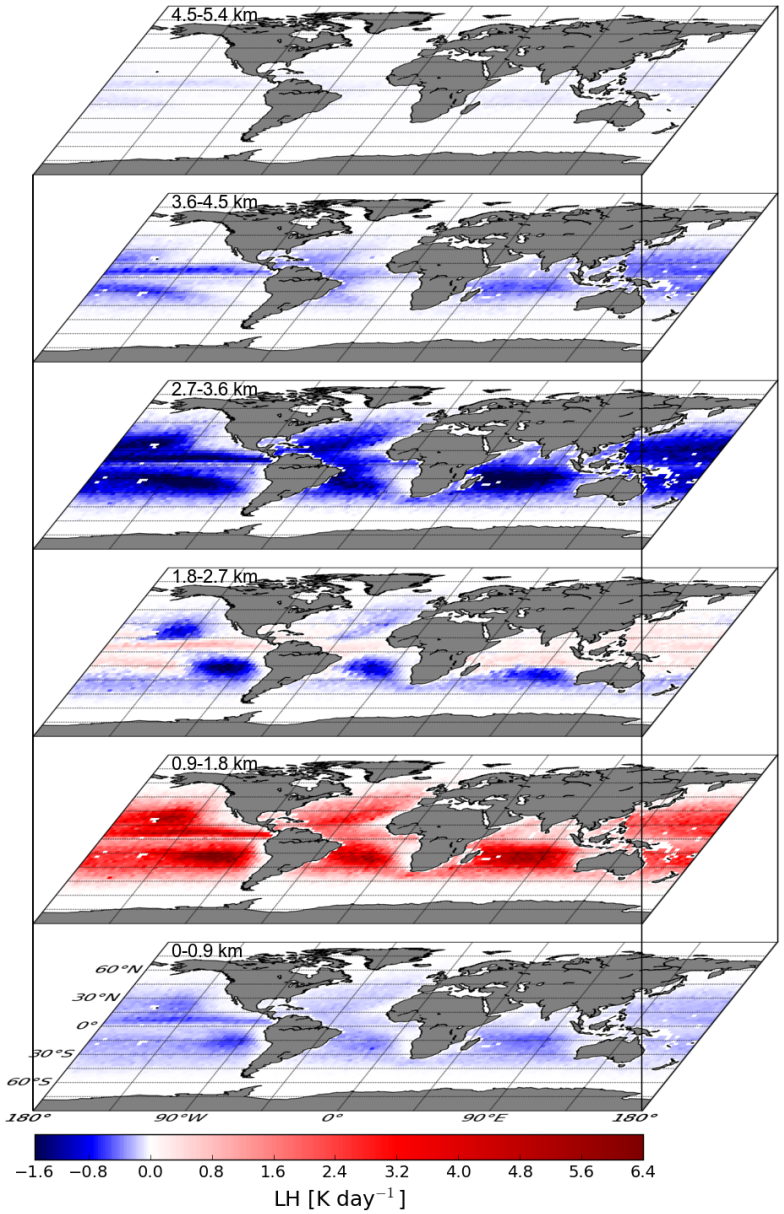

FIGURE 3.6: As in Figure 3.4 but only for profiles with a maximum vertical velocity less than 1 m/s representing more stratiform regimes.

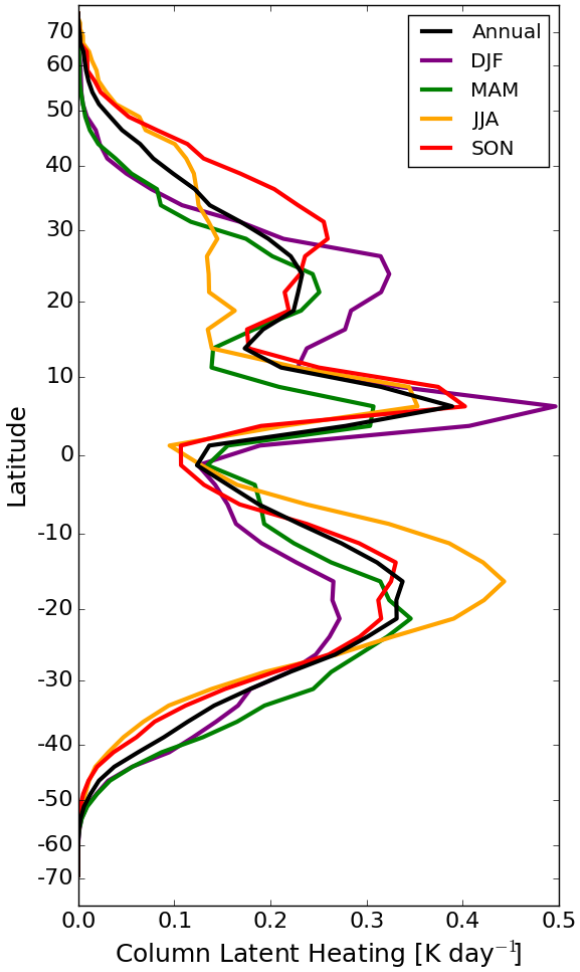

FIGURE 3.7: Zonal distribution of the monthly mean column latent heating for the full annual cycle (black) and months that comprise each season (see legend).

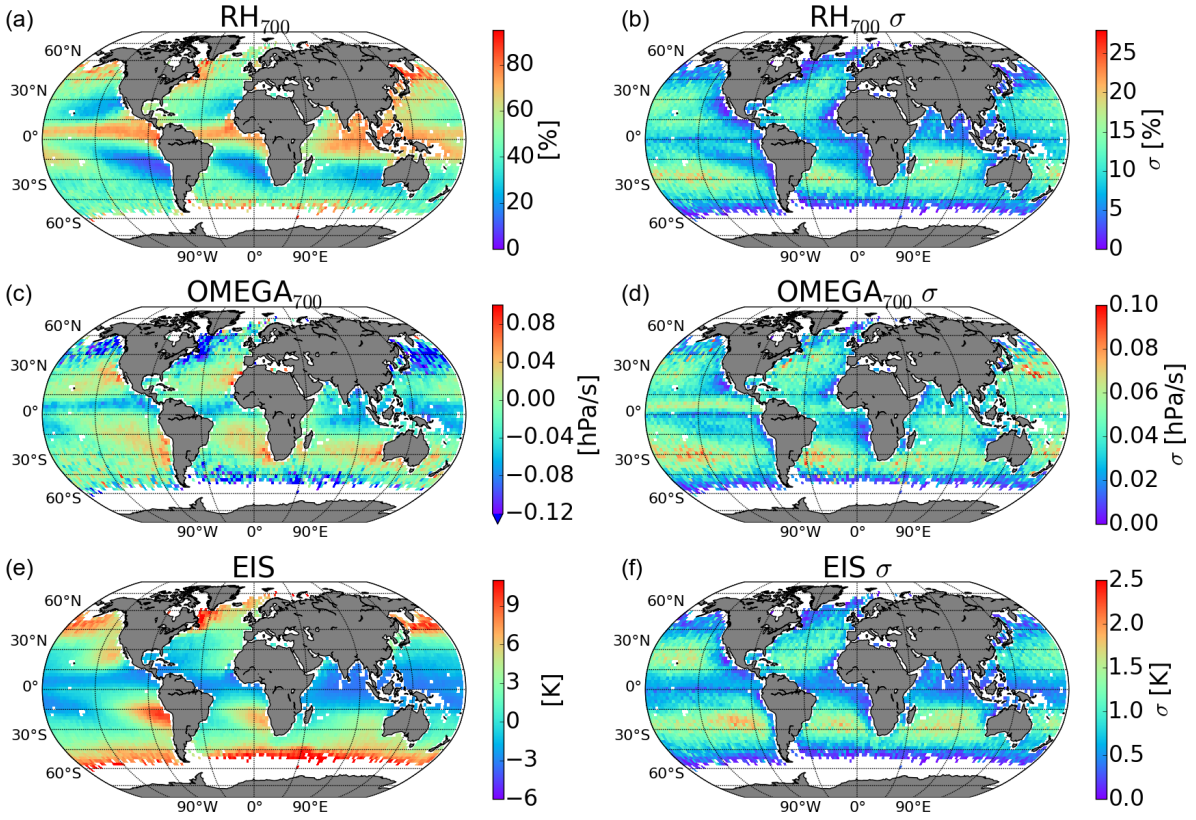

FIGURE 3.8: Monthly conditionally averaged MERRA parameters for instances where warm rain was retrieved: (a) relative humidity at 700 mb, (c) vertical velocity at 700 mb, and (e) EIS, with respective standard deviations in (b), (d), and (f).

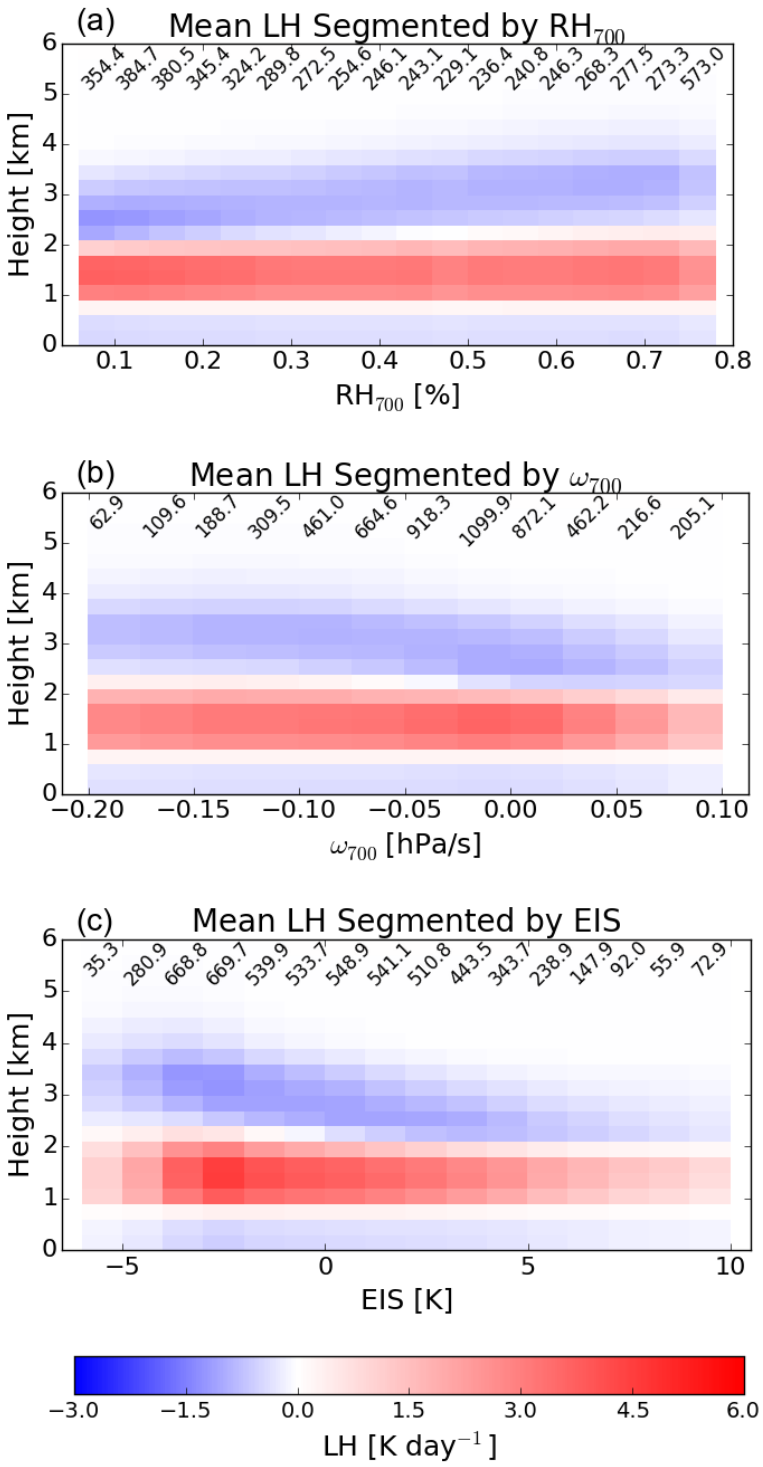

FIGURE 3.9: Distributions of monthly mean latent heating and cooling profiles binned by conditionally averaged MERRA parameters of (a) RH at 700 mb, (b) ω at 700 mb, and (c) EIS. The number of warm rain scenes in each bin is noted at the top of each bin profile (in thousands).

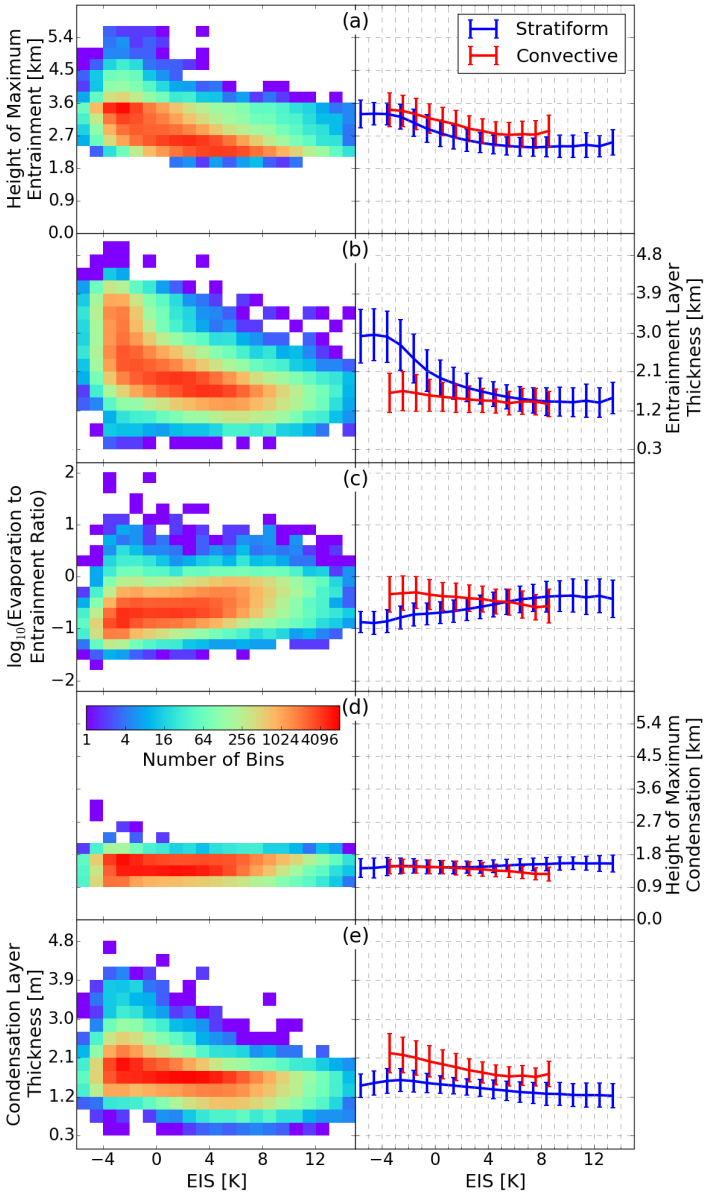

FIGURE 3.10: Joint monthly averaged grid box distributions between EIS and characteristics of the average latent heating profile for all regimes (left) as well as 1 K EIS bin mean and standard deviation separated into each regime (right). Characteristics shown are (a) height of the maximum cooling in the entraining layer above the heating, (b) depth of the cooling layer above the heating, (c) ratio of the cooling below the heating layer to the cooling above the heating layer, (d) height of the maximum condensational heating, and (e) thickness of the heating layer. Line plots are slightly offset on the abscissa for improved viewing.

Chapter 4

Regional Variability

4.1 Introduction

Analysis of warm rain on a global scale reveals not only that warm rain is nearly prevalent everywhere but that there are differences in the frequency of occurrence, intensity, and structure. Cursory examination of these patterns compared with environmental metrics of stability and humidity shows that at least the intensity and structure is at least partially related to environmental stability on a global scale. The next step is to examine the variability of the latent heating profile character on a regional level to determine to what extent these relationships hold with respect to intraregional variability. Selecting a variety of regions provides many unique samples of warm rain behavior in response to different

variations of environmental parameters against which climate model responses can be evaluated.

4.2 Vertical character of latent heating

Initially presented is a comparison between the regions highlighted in Figure 2.2 covering a wide variety of locations that warm rain exists. The following sections are grouped either by location or regime. The full extents are listed in Table 4.1. In each case, two types of profiles are shown: the four year conditional mean profile and the monthly unconditional mean (as described in Section 2.3). Additionally, an inset scatterplot shows the monthly mean and spread of EIS and ω_{700} for each profile to place a given subregion in context of its environment.

4.2.1 CGILS

The first place examined is the CGILS transect in the Northeastern Pacific Ocean (Fig. 4.1), which encompasses the transition from laminar or sheet-like warm rain to more isolated shallow convective warm rain. Three equal grid resolution boxes sized 5^{o} longitude, 3^{o} latitude are selected that extend from off the coast of California southwestward. Starting in the box nearest to the coast, the conditional mean (left side of figure) shows a profile with heating between 1km and 2km in height, some minor cooling below the cloud base, and a 1.5 km layer of cooling above the heating. While the heating has a maximum near the middle of the heating layer, the entrainment cooling is focused more toward the

bottom of the cooling layer. Moving southwestward, the conditional profile increases in magnitude of heating and in both magnitude and vertical extent of entrainment cooling above the heating layer. Additionally, the southwesternmost average profile (red) reaches a maximum cooling at a higher level.

The inset figure shows the general trend of ω_{700} and EIS both decreasing while moving southwestward, though differences in ω_{700} are relatively small for the central and southwestern boxes. Now, taking into account the frequency of occurrence (Fig 4.1, right side), differences appear in both heating and cooling magnitude among the boxes. Though in the conditional case where each successively southwestwardly profile increased in heating linearly, the northeast box is shown to actually contribute a lower fraction relative to the others. This accentuates some of the differences that arise possibly not only due to environmental differences but also the frequency of occurrence of retrieved precipitating warm rain systems.

4.2.2 VOCALS

A transect of 10^o longitude, 10^o moving west from South America in the VOCALS region of similar behavior with respect to regime change shows a similar progression (Fig. 4.2). Conditionally, the profile with the least amount of heating is the easternmost profile nearest to the coast (red) while the most heating occurs in the westernmost profile (green). More subtly, the level of maximum condensational heating slightly decreases due to a fuller amount of heating in lower layers. Entrainment cooling above the heating layer

shows the same progression as heating with increased cooling magnitude moving away from the coast. The westernmost profile (green) displays the highest level cooling with a peak around 2.5 km.

Environmentally, EIS continually decreases moving westward, while the ω_{700} magnitude increases for the first three profiles then decreases. So far, lower levels of EIS have indicated more heating and entrainment cooling with deepening of the cooling layer above the cloud as well. Considering the frequency of occurrence, the center-west (yellow) and westernmost profile (green) contribute a nearly similar amount of heating. The easternmost profile (red) is again contributing a relatively lower amount of heating compared to the others.

4.2.3 Atlantic transect

The transect spanning the North Atlantic Ocean is unique from others so far in that it is much longer and extends from near a western coastline to near an eastern coastline. Namely, this transect is of 7.5^{o} longitude, 5^{o} latitude boxes from the Azores in the Northeast Atlantic Ocean to Barbados in the Tropical West Atlantic Ocean that covers a wide range of environmental conditions. Moving southwestward, the conditional profiles extend from a smaller magnitude of heating, increasing to slightly larger magnitudes peaking in the central profile (yellow), and then decreasing slightly in the two southwestern profiles (green and blue). The cloud cooling layer above condensation monotonically increases over the course of the transect in height and magnitude. When considering the

frequency of occurrence, the pattern of profiles is such that the heating layer increases in its magnitude while moving southwestward along the whole extent.

The inset figure again shows some similarity in the patterns of environment to the properties of the profile. ω_{700} behaves in a parabolic manner consistent with the heating magnitude: moving southwestward increases ω_{700}, an increase of large-scale subsidence, increases in heating magnitude peaking in the central profile (yellow), then decreases when moving towards the most southwestern profile. Contrast this with EIS, which is consistently decreasing over the full course of the transect. Considering that EIS indicates local inversion strength, moving towards negative values means increasing instability over the course of the transect–matching with the increase in cooling layer magnitude and depth. Thus response to the EIS is similar to prior regions considered so far, while ω_{700} yields differing behavior.

4.2.4 Equatorial Pacific

Variability within the ITCZ and broader Equatorial region between the east and west sides of the Pacific Ocean basin has been previously documented (e.g. Back and Bretherton, 2006, Klein and Hartmann, 1993). Two regions were examined in Back and Bretherton (2006) which revealed a difference in the character of vertical motion profiles, with the Eastern Pacific more bottom heavy and the Western Pacific more top heavy. These differences may represent different regimes of precipitation given the implications of the vertical motion structure on latent heating, with the former containing a large magnitude

of heating near the surface and the latter containing a larger magnitude of heating in the free troposphere.

Profiles for these two sections of size 20° longitude, 2.5° latitude are shown in Figure 4.4. The eastern profile (orange) contains more heating, less entrainment cooling above that heating, and more evaporative cooling below the cloud than the western profile. The difference in mean retrieved character may possibly be showing warm rain in the Western Pacific (red) is more efficient at moistening the troposphere with more cooling above the heating layer per unit of heating, which could be some signal of a moist-convective feedback in the Western Pacific (e.g. Grabowski and Moncrieff, 2004). When the frequency of occurrence is accounted for, the eastern box contains much more heating and cooling overall. This difference in prevalence hints that warm rain makes up a larger component of heating in the eastern region while warm rain in the western region may be only a fraction of the full convection occurring and is consistent with the findings from Back and Bretherton (2006).

4.2.5 Interregional variability

Five stratocumulus regions from Klein and Hartmann (1993) are shown next (Fig. 4.5), all of 10° longitude and 10° latitude. Conditionally, these profiles have some similarities. Australia and Canary Island have nearly equal heating but different cooling such as Canary peaking slightly higher. Peru and the American boxes have the second largest conditional heating magnitude in general, with Peru containing somewhat more heating,

yet their cooling structure is more alike. The Namibian box has the smallest magnitude of heating and cooling. With frequency of occurrence considered, the distribution shifts with the Australian box contributing much more than the Canary Islands and Namibia contributing a larger amount of heating. No clear pattern in the environmental parameters are present in these distributed boxes.

4.2.6 Transect behavior

The tendency for the transects to react similarly moving from east to west motivates summarizing how the relationships between some of the characteristics of the latent heating profile behave with changes in either zonal distance or environmental parameters. These behaviors could be important for considering future changes in climate (e.g. Cess et al., 1990, Dufresne and Bony, 2008). Figure 4.6 shows the changes in the monthly mean heating and cooling based on longitudinal degrees from the easternmost box for each of the CGILS (NEPac), VOCALS (SEPac), and Atlantic (Atl) transects.

The left side of Figure 4.6 displays the heating characteristics. In all three cases, the magnitude of unconditional column heating increases while moving west. The Pacific transects (green and red) have a similar slope in increase per degree of longitude, while the Atlantic transect increases at a slower rate. The thickness of the net condensational layer remains mostly consistent, increasing by about one vertical level over the course of most the transects; the CGILS transect remains constant over the full length. Finally,

the level at which condensational heating peaks varies somewhat but has no discernible trend.

The right side of Figure 4.6 shows different behavior for some parameters. The unconditional cooling magnitude increases moving westward to relatively less stable regions for all three transects. The thickness of the entraining layer also generally increases moving westward, with the Atlantic transect increasing in all but the westmost box. And the level at which entrainment cooling peaks increases over the course of each transect, with a difference of about one extra algorithm level (300 m).

The transects also indicated some trends with respect to EIS, so shown in Figure 4.7 are similar cross sections like Figure 4.6 but now plotted as a function of EIS. In each transect, EIS decreases over the full extent of the profile, so moving from right to left equates to moving from right to left in Figure 4.6 as well.

Focusing first on the integrated heating and cooling components in the top row, a general trend is shared by each of the transects, but only relatively speaking. Because the frequency of occurrence differs in each of these regions, the absolute values are understandably different. Nevertheless, a trend of perhaps an exponential form exists for each of the three transects describing the increase in both magnitude of integrated heating and cooling as EIS decreases.

The thickness of the condensation and entraining layers are shown in the middle row of

Figure 4.6. Because thickness describes the physical extent of the profiles is not unconditional, there is some similarity between values in all of the transects. The overall trend is generally an increase in the thickness of the layer with decreasing EIS. Some overlapping of values occurs between the CGILS (red) and VOCALS (green) transects. These two transects even nearly line up with EIS values in the Atlantic transect that could possibly reveal a robust relationship that describes the change in the layer thickness of heating and cooling above the heating with respect to a change in EIS.

Finally, the levels of maximum heating and cooling are shown in the bottom row of Figure 4.6. A less discernible relationship is present in the height of maximum heating, but there is a movement towards higher values in the higher EIS (or more stable) environments and a slight lowering towards more unstable environments. Similarity is more coherent in the level of maximum cooling with respect to EIS, where again the two Pacific basin transects nearly overlap and have a similar slope as the Atlantic basin transect.

These plots hint at the existence of relationships between inversion strength and latent heating profile–at a minimum relative to a given basin but possibly more robust as well. Deeper entraining layers are shown to occur in less stable environments. This follows behavior described in Wood (2012), who states that higher stability yields less entrainment and shallower planetary boundary layers. Some hesitation in universally applying these is due to the differences in stratocumulus among the different basins outside these transects specifically from Figure 4.5. Additionally, differences in the grid box sizes could

be responsible for blurring some signals in environmental parameters. One important consideration to keep in mind is that there is no direct input into the WALRUS product related to the environmental character except that a given reflectivity profile of a storm from CloudSat is below the freezing level. In other words, the algorithm is able to discern differences in local environments strictly based on the radar reflectivity profile.

Description	Location
CGILS Transect	
NE	130°W–120°W, 27.5°N–32.5°N
Cent	140°W–130°W, 22.5°N–27.5°N
SW	150°W–140°W, 17.5°N–22.5°N
VOCALS Transect	
E	90°W–80°W, 20°S–10°S
CE	100°W–90°W, 20°S–10°S
CW	110°W–100°W, 20°S–10°S
W	120°W–110°W, 20°S–10°S
Atlantic Transect	
NE	25°W–17.5°W, 35°N–40°N
CNE	32.5°W–25°W, 30°N–35°N
Cent	40°W–32.5°W, 25°N–30°N
CSW	47.5°W–40°W, 20°N–25°N
SW	55°W–47.5°W, 15°N–20° N
Equatorial Pacific	
East	140°W–120°W, 7.5°N–10°N
West	120°E–140°E, 5°N–7.5°N
Stratocumulus	
Australian	95°E–105°E, 35°S–25°S
Namibian	0°–10°E, 20°S–10°S
Canarian	35°W–25°W, 15°N–25°N
Peruvian	90°W–80°W, 20°S–10°S
American	130°W–120°W, 20°N–30°N

TABLE 4.1: List of locations in analysis (shown in Figure 2.2) with geographic bounding box.

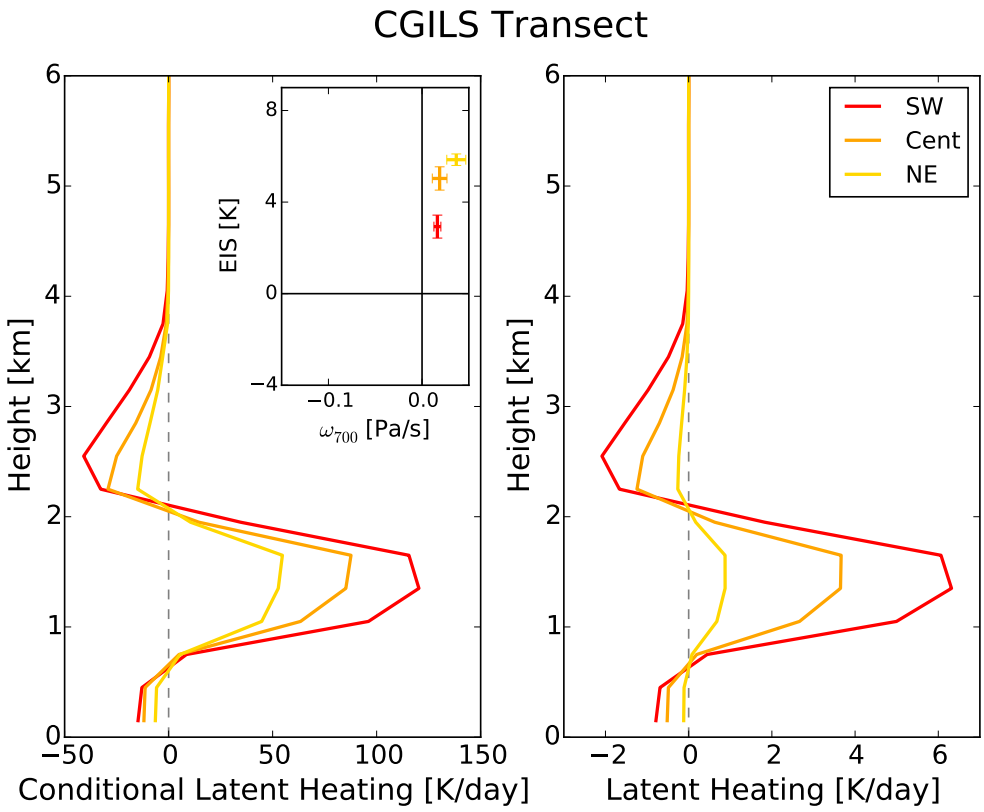

FIGURE 4.1: Profiles of latent heating [K day^{-1}] for boxes selected from the CGILS experiment for both the conditional mean (left) and monthly mean (right). Also presented are the box average and standard deviation EIS [K] and ω_{700} [Pa/s] (inset).

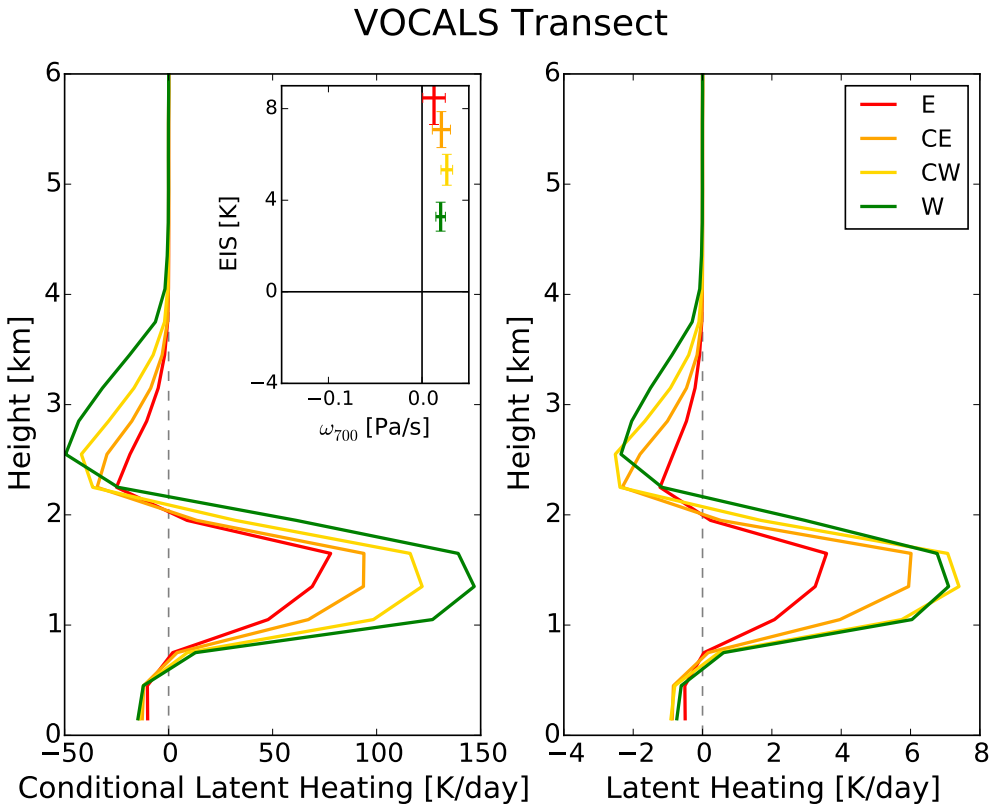

FIGURE 4.2: As in Figure 4.1 but for the VOCALS campaign region.

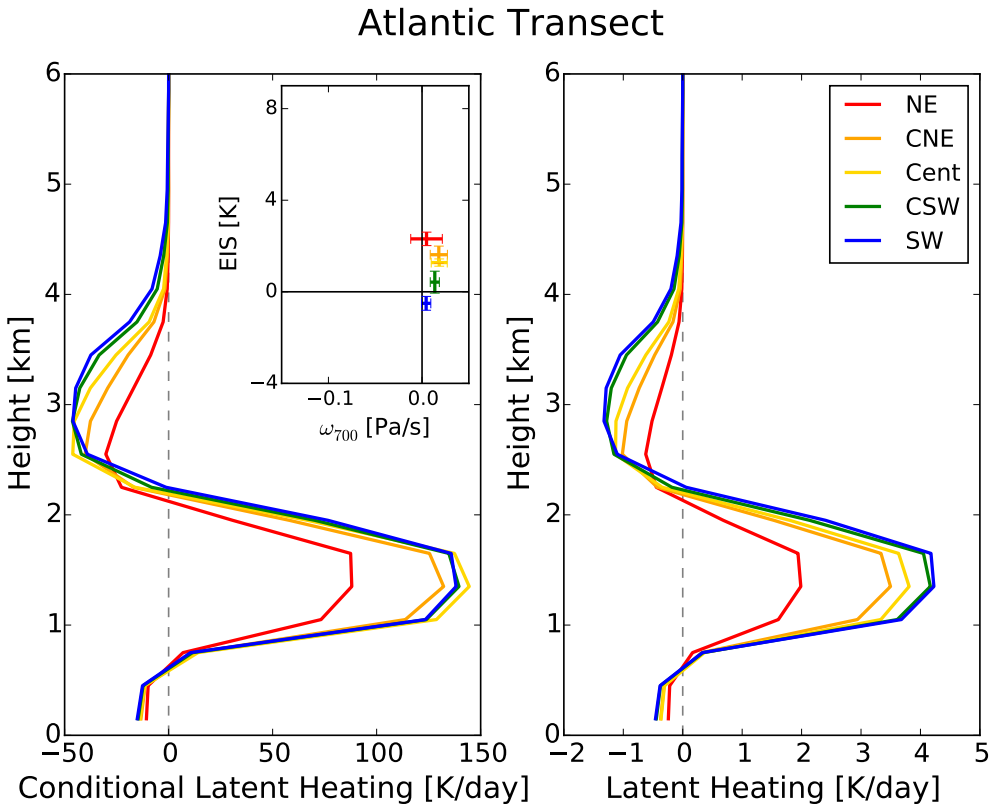

FIGURE 4.3: As in Figure 4.1 but for a transect extending from the Azores to Barbados.

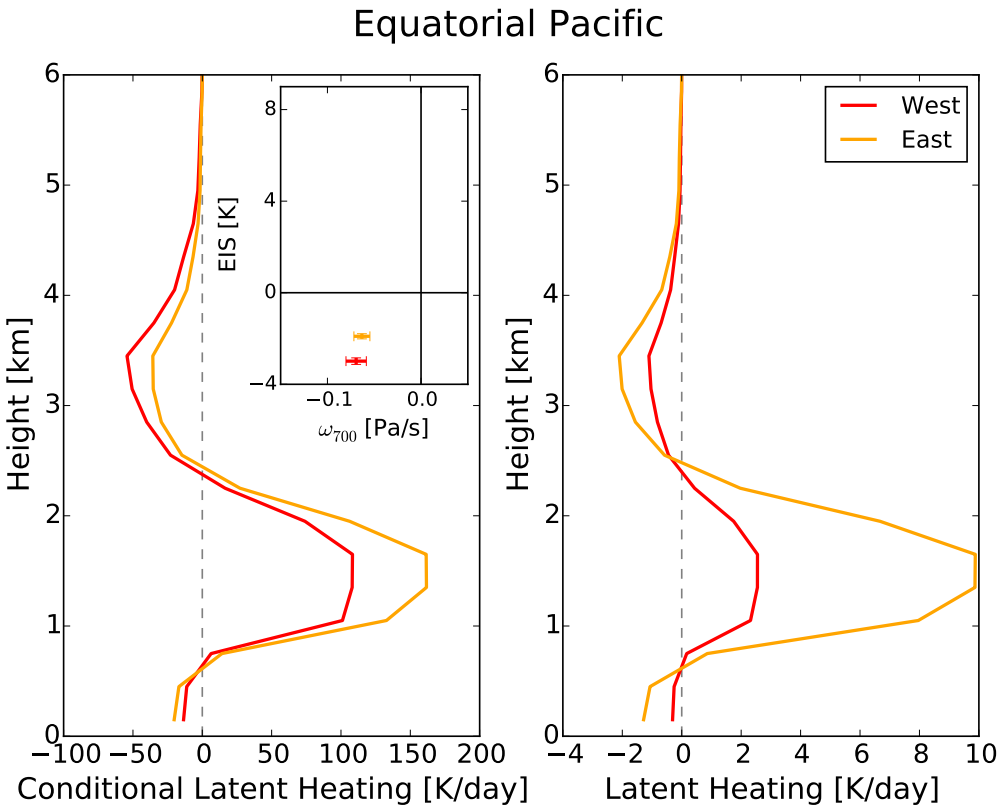

FIGURE 4.4: As in Figure 4.1 but for two regions embedded in the ITCZ from Back and Bretherton (2006).

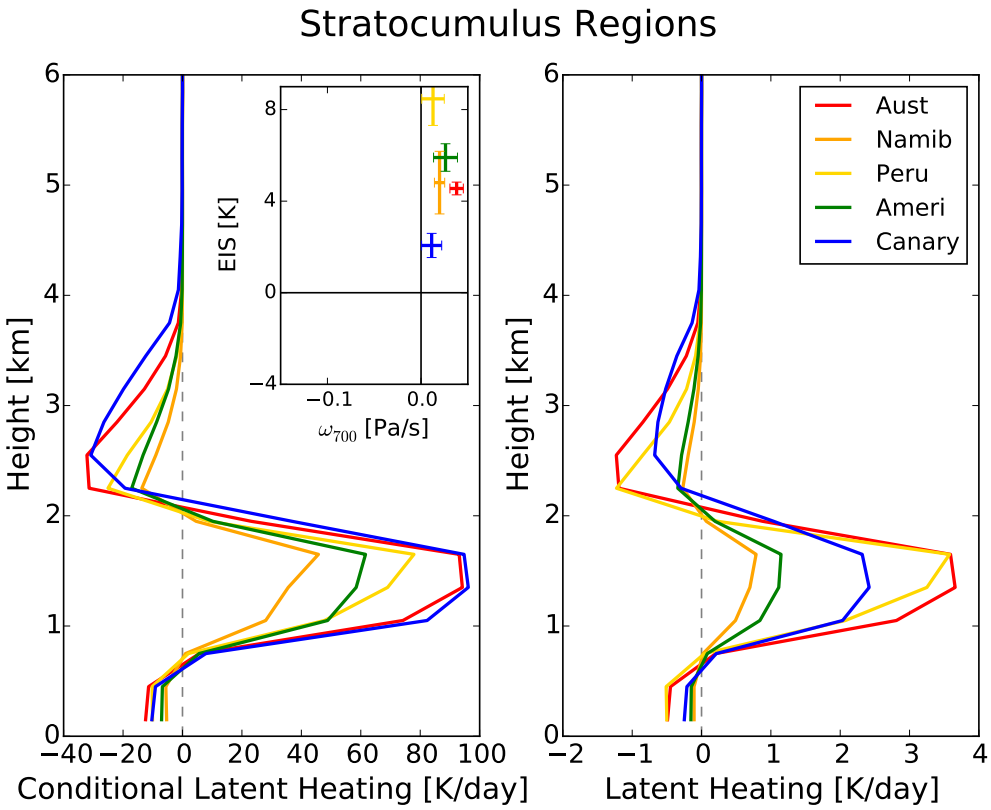

FIGURE 4.5: As in Figure 4.1 but for regions of stratocumulus taken from Klein and Hartmann (1993).

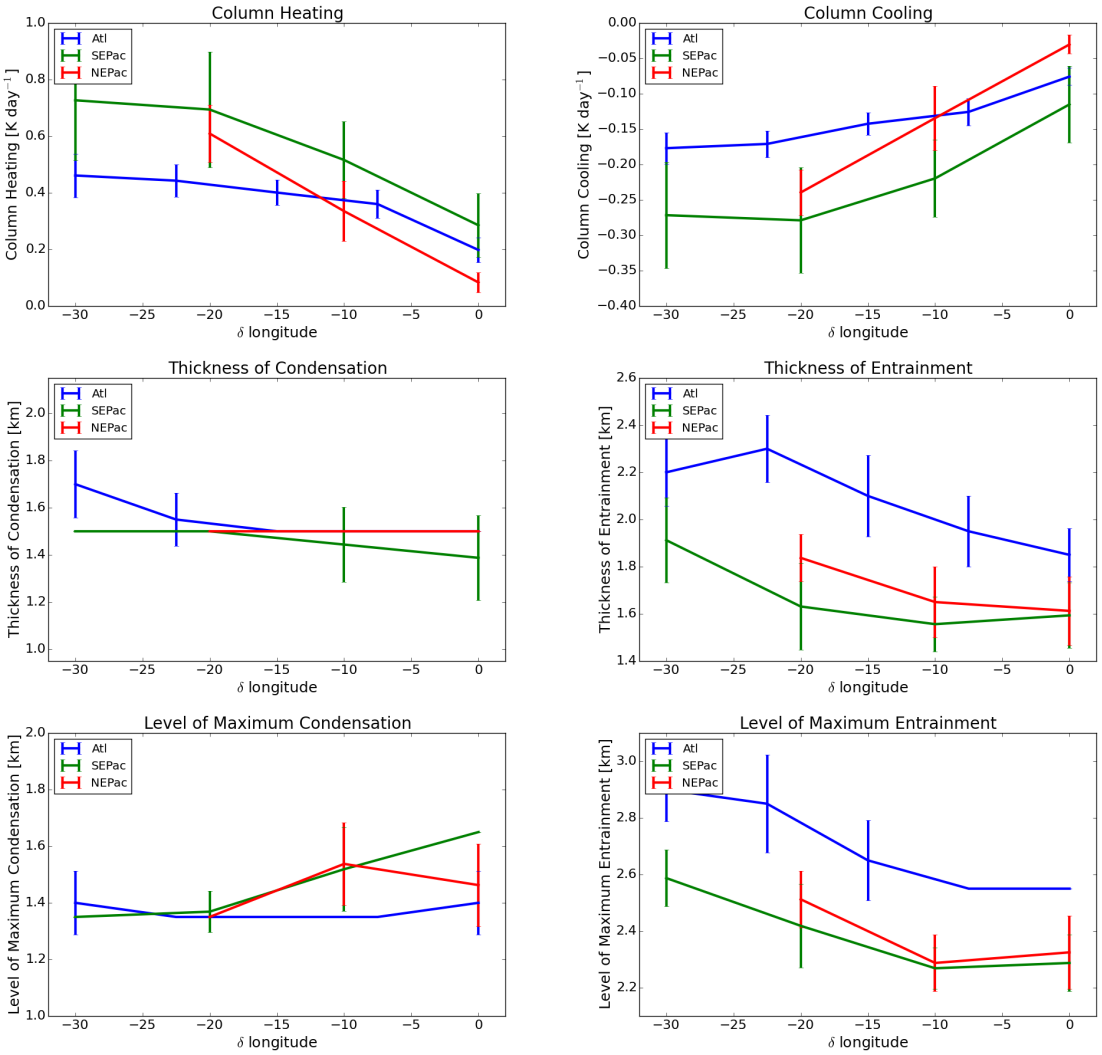

FIGURE 4.6: Behavior of latent heating heating and cooling characteristics as a function of longitude from the easternmost box.

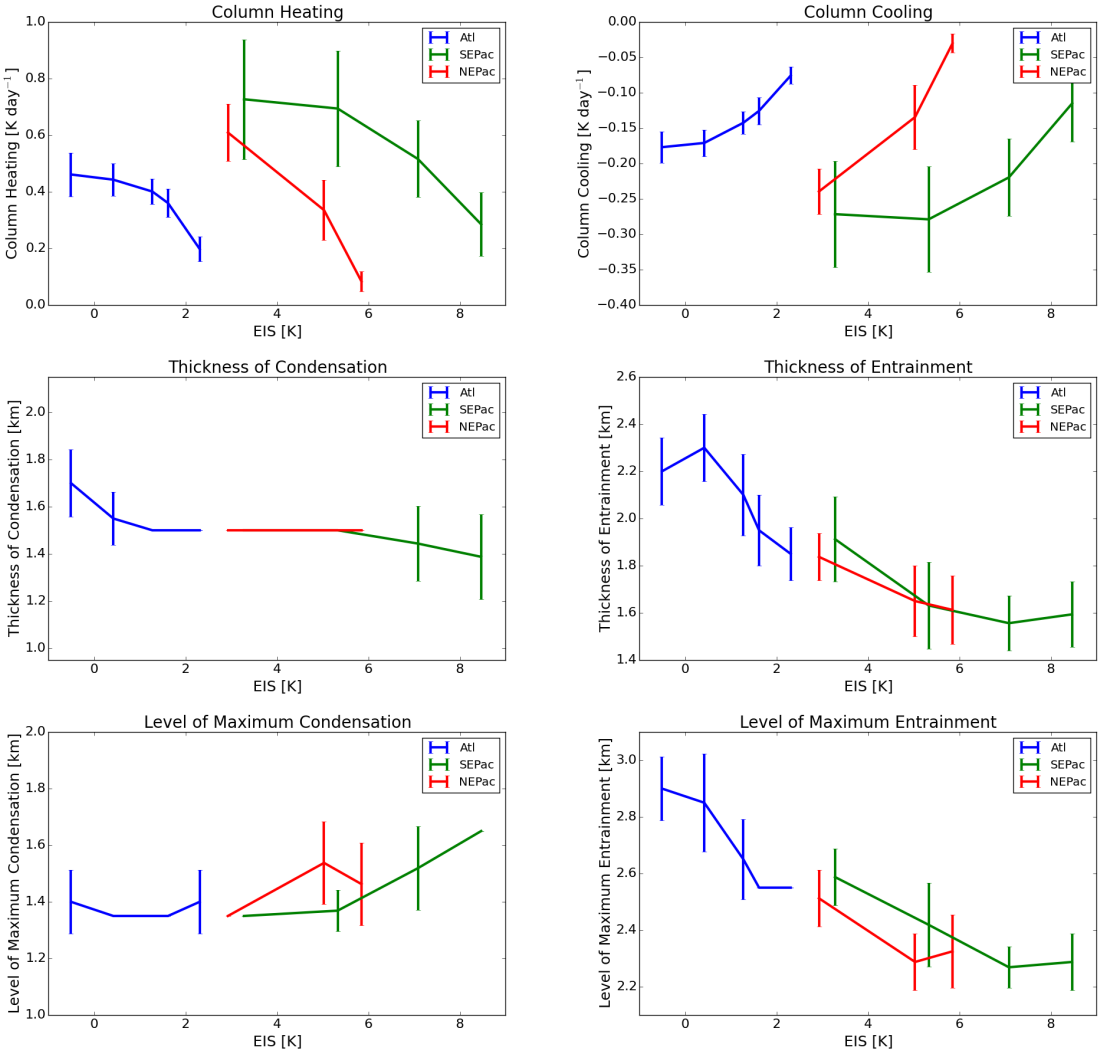

FIGURE 4.7: As in Figure 4.6 but as a function of EIS.

Chapter 5

A Blended Perspective and the Madden-Julian Oscillation

5.1 Blended Perspective

As outlined in Section 2.3, and given the synergies between CloudSat and TRMM (e.g. Berg et al., 2010), a merged perspective of latent heating between CloudSat WALRUS and TRMM SLH has the potential to cover the full spectrum of global precipitation systems. This stems from CloudSat's increased detectability of lightly precipitating systems but attenuation in stronger systems and TRMM's ability to penetrate intensely raining systems but underestimating light precipitation. To these ends, a blended CloudSat–TRMM latent heating dataset is established by substituting SLH shallow latent heating

with WALRUS estimates. Figure 5.1 breaks down all of the individual regime contributions to column net latent heating in the greater tropics. Convective cloud latent heating from SLH (Fig. 5.1(a)) is strongest in areas known for deep convection, including just north of the Equator in the Atlantic Ocean and Eastern Pacific Ocean basins where the ITCZ is prevalent on average. The Indian Ocean and Maritime Continent are also areas of strong convection, as is an arm extending from the Maritime Continent southeastward in the South Pacific Convergence Zone. Convective heating is also high over Central America, parts of the Amazon Basin often dubbed the "green ocean" (Williams et al., 2002), and Central Africa–all areas known for convection (e.g. Liu and Zipser, 2005).

Stratiform latent heating (Fig. 5.1(b)) is much lower in magnitude compared to that from convective clouds across the greater tropics. This regime peaks around the 30^{o} latitude in both hemisphere, with smaller peaks in the Maritime Continent area. Latent heating from warm rain taken from WALRUS (Fig. 5.1(c)) peaks north of the Equator in the Eastern Pacific Ocean and has local maxima in the stratiform regions, namely off the western coasts of South America, Africa, North America, and Australia as seen in Chapter 3. Finally, the sum of these three regimes is presented in Figure 5.1(d) providing a fuller perspective of latent heating merged from instruments sensitive to different regimes of precipitation.

5.2 Madden-Julian Oscillation

To gain a more complete perspective of the evolution of the vertical structure of diabatic heating over the MJO, this blended latent heating dataset is composited according to the WHI (Wheeler and Hendon, 2004) to indicate the stage of the MJO for a given day. Anomalous heating observations are first calculated for each day in the boreal winter and straddling transition months (i.e. November to April). Anomalies are calculated by taking the mean profile of each day over all of the years used and then removing the monthly mean from each respective day of each given month. After the mean is removed, the five day trailing mean of anomalous heating observations is calculated for each day to further reduce noise due to observational frequency. Finally, the trailing averaged values are composited with the stage of the WHI for the final day, and only active events are included as indicated by a magnitude greater than one of the WHI EOF vector.

This methodology differs slightly from Jiang et al. (2011). Rather than removing the annual cycle on a monthly basis for each day, the authors removed the annual cycle on a daily basis and applied some smoothing to the annual cycle by including the first three leading harmonics (X. Jiang, personal communication). The methods used here are employed to further account for noise that may occur when restricting the study period to fewer years, but differences that occur may warrant further investigation.

Analysis from Jiang et al. (2011) of composited mean profiles over the Western Pacific Ocean (150°E-160°E, 10°S-10°N) and Eastern Indian Ocean (80°E-90°E, 10°S-10°N) is

replicated to determine if an adequate comparison can be made with conclusions from that study. Figure 5.2 shows the analysis calculated over the ten year period from 1998 to 2007 for $Q_1 - Q_R$ (Eq. 1.3) in all regimes from SLH. The same analysis is performed for Figure 5.3 but for latent heating from all regimes explicitly. Jiang et al. (2011, Figure 3) displays the same major characteristics as Figure 5.2, with some small differences in the lower atmosphere starting in earlier phases. Differences do also exist because of contouring applied to the original plot, but the large scale pattern matches.

Similarly in the Indian Ocean, the large scale structure is close to the original, including the slightly sloping bottom of cooling in the later phases and the most anomalous heating occurring in earlier stages. Differences between $Q_1 - Q_R$ and latent heating arise in slightly lower vertical extents in anomalous heating as well as a lower magnitude of noise in the lower atmosphere, but otherwise the general structure continues to persist.

As previously discussed, there are limitations to the observational period from CloudSat, the greatest of which is that it did not launch until 2006. Thus the TRMM analysis is repeated for January 2007 to December 2010 to provide the same sampling time period as CloudSat (Figure 5.4). The differences that exist may be the result of different MJO strengths in this shorter and more recent time period. these years compared to the original analysis including possible influences from other climate features. Both cooling and heating anomalies are more focused in both regions for the shorter time period, still possibly due to more noise in the shorter time period. Differences between $Q_1 - Q_R$ and

latent heating also behave with a similar pattern, shifting the profile anomalies slightly lower in the atmosphere.

Composites are next assembled for latent heating from CloudSat WALRUS estimates in Figure 5.6 following the same methodology as SLH. In the Western Pacific, there are some low level anomalies in positive heating that occur in earlier stages, followed by alternating negative and positive lower level anomalies. Negative values may mean either less net heating or more net cooling. Elevated areas of positive anomalies are likely less entrainment cooling as opposed to elevated heating. Separating profiles before removing the annual mean in terms of heating and cooling may help confirm this. Nonetheless, some low level heating growing in height does appear in earlier stages in the Western Pacific region. The Indian Ocean box also exhibits low level positive anomalies that precede the stronger anomalous heating.

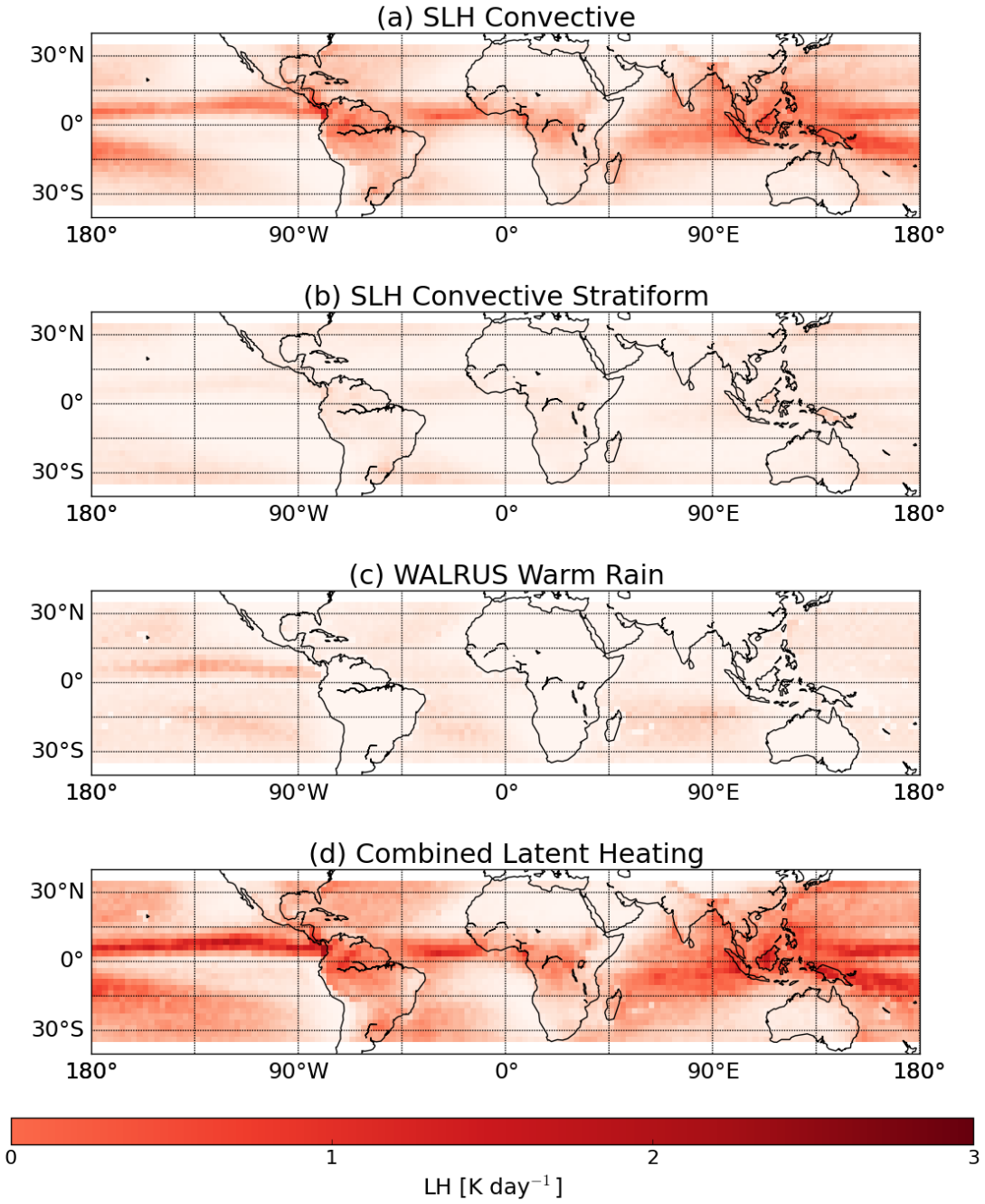

FIGURE 5.1: Monthly mean latent heating from January 2007 to December 2010 for (a) convective precipitation from SLH, (b) stratiform convective precipitation from SLH, (c) warm precipitation from WALRUS, and (d) all three regimes combined.

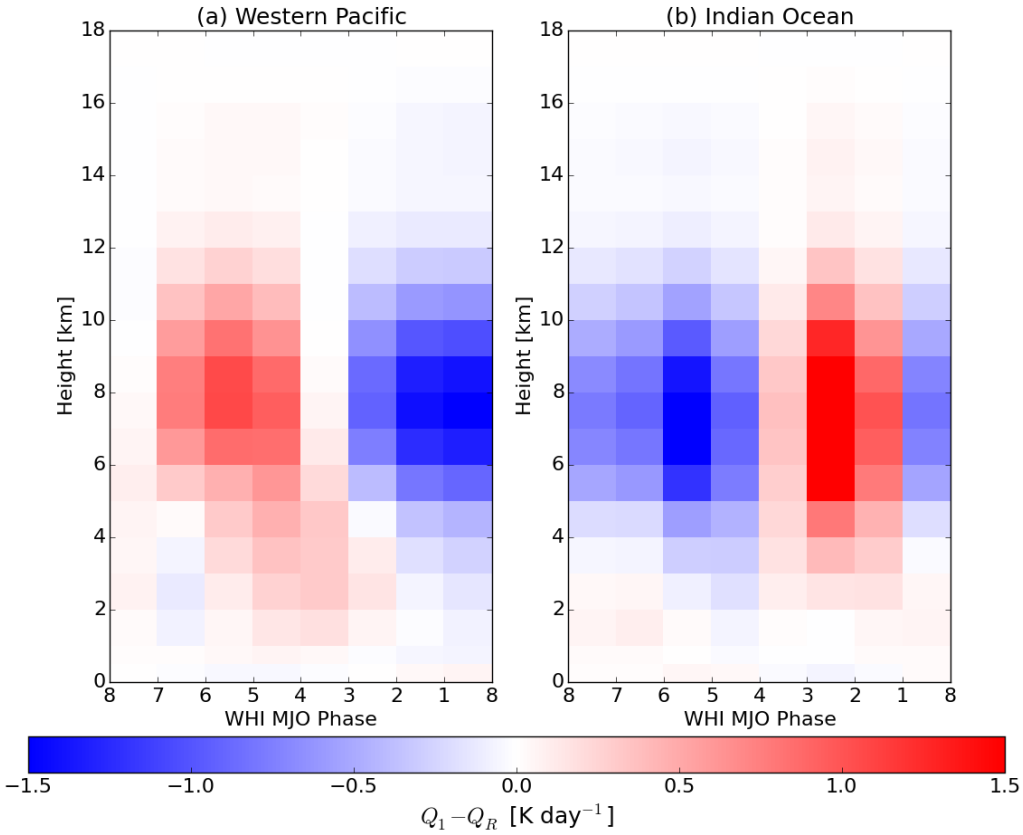

FIGURE 5.2: Composites from 1998-2008 of boreal winter anomalous $Q_1 - Q_R$ heating [K day^{-1}] from TRMM SLH with WHI MJO indices for a box in (a) the western Pacific Ocean (150°E-160°E, 10°S-10°N) and (b) the Eastern Indian Ocean (80°E-90°E, 10°S-10°N).

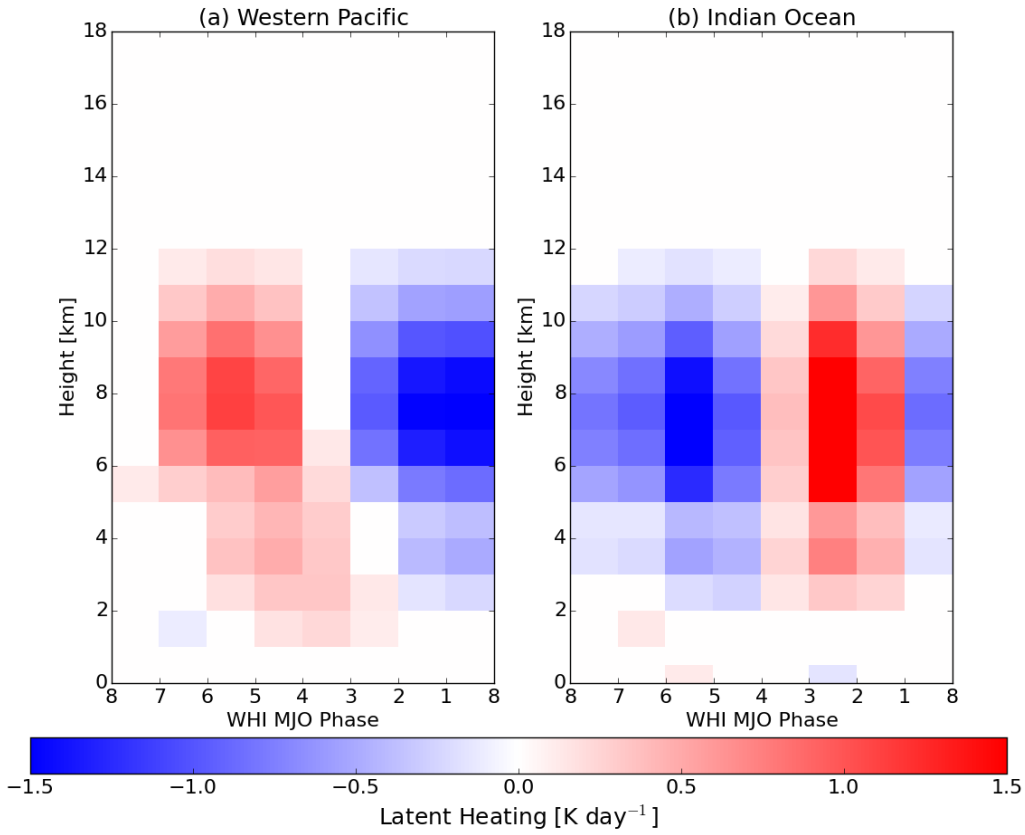

FIGURE 5.3: As in Figure 5.2 but for latent heating [K day^{-1}] from TRMM SLH.

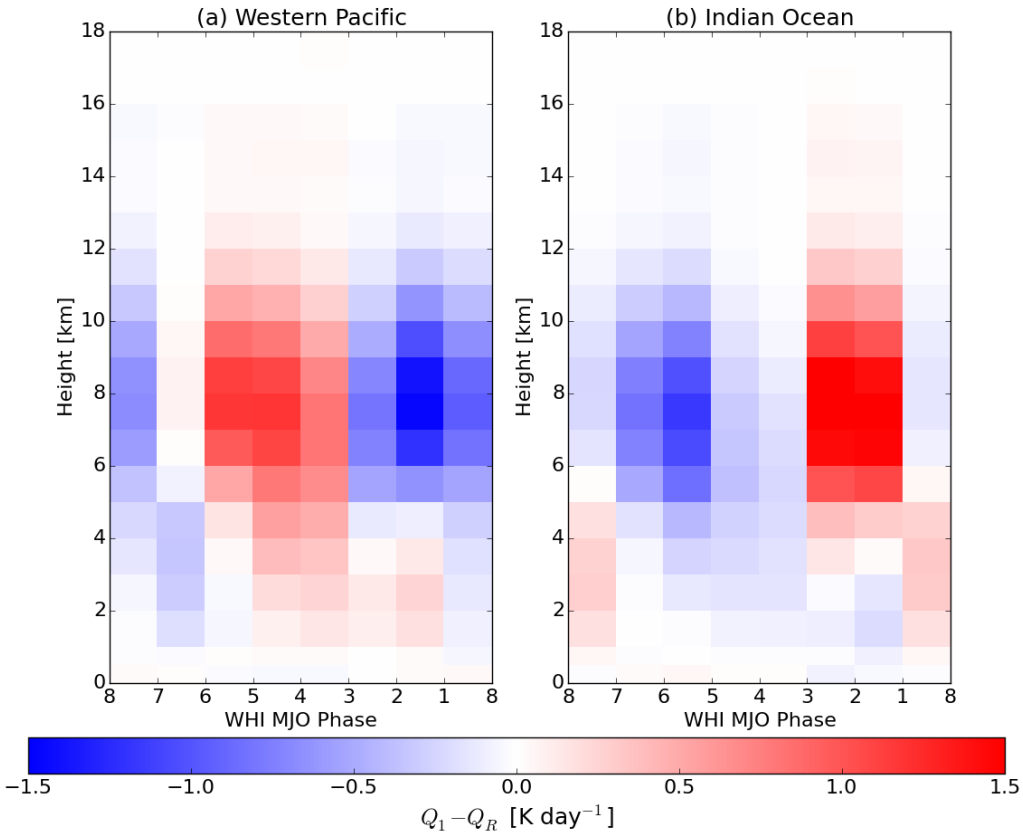

FIGURE 5.4: As in Figure 5.2 but for 2007-2010.

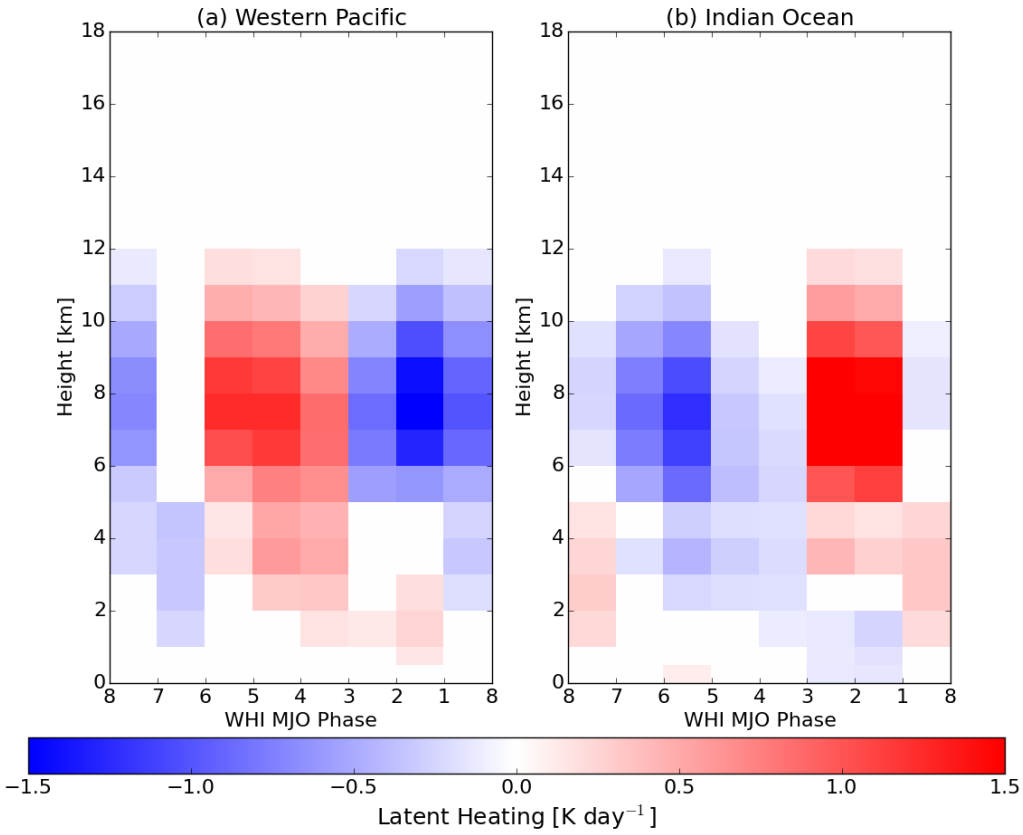

FIGURE 5.5: As in Figure 5.3 but for 2007-2010.

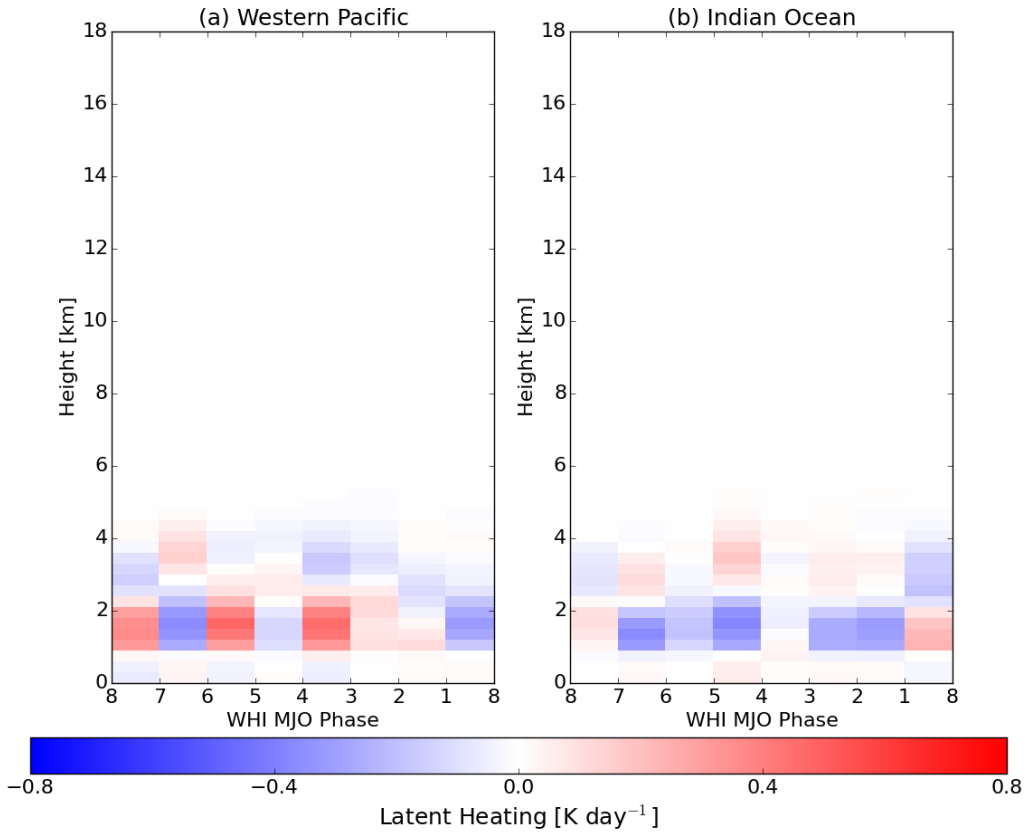

FIGURE 5.6: As in Figure 5.5 but for CloudSat WALRUS latent heating.

Chapter 6

Synthesis*

A four year (2007-2010) climatology of latent heating and cooling for oceanic warm rain systems has been established based on CloudSat CPR observations. Because of the CPR's sensitivity to clouds and light precipitation, we can observe and estimate the impact that may otherwise be underestimated or missed in other estimates as evidenced by Berg et al. (2010). Warm rain makes up nearly 9.2% of precipitation accumulation over the oceans and comprises nearly 14% of tropical rainfall (bounded by 25^{o} latitudes). Convective warm rain, defined as profiles where the in-cloud vertical velocity exceeds 1 ms $^{-1}$ in any height bin, constitutes 11% of warm rain occurrence but yields more than a third of the total warm rain accumulation. Warm rain condensational processes contribute 0.15 K day^{-1} (7.44 W m^{-2}) of heating globally on average to the atmosphere, accounting for

* Part of this chapter is under review in the *Journal of Geophysical Research: Atmospheres.*

7.6% of the total atmospheric latent heating contribution over the oceans estimated in L'Ecuyer et al. (2015) and nearly matching the difference between observed and optimal estimation constrained latent heating estimates.

The character of the vertical profile of latent heating and cooling varies substantially across the globe on a monthly timescale, with areas of environmental instability yielding deeper evaporative layers than those in more stable environments. Regions vary not only in the heights of cooling from entrainment but also in the ratio of cooling below and above the heating layer which stems from the regime of warm rain occurring. There is much less variation in the layer of net heating, which generally resides consistently between 1 and 2 km suggesting that condensation processes are less sensitive to changes in stability than evaporation associated with cloud top entrainment. Column latent heating and cooling varies substantially on seasonal time scales, with hemispheric winters contributing more overall heating than the respective hemispheric summers. Contributions from convective and stratiform rain to the global mean latent heating are nearly equal in spite of their different frequencies of occurrence.

Examining latent heating on a more regional scale provided further information about variability of the processes as well as environmental effects on the character of the latent heating profile. In transects moving from western coasts of continents eastward, profiles generally followed the trend of increased condensational heating and expansion and increase of the cooling layer above the heating. This behavior aligned with a fairly robust

relationship with EIS. Large scale vertical velocity did not reflect as strong of relationship which could possiby be the result of other stronger influences or that the regions examine were of differing size and possibly convoluting a coherent signal.

A merged perspective of latent heating was created from both CloudSat WALRUS and TRMM SLH by substituting SLH shallow stratocumulus with WALRUS warm rain latent heating. This hybrid product yielded increased column heating over areas of coastal upwelling and the Equatorial North Pacific. Composite analyses of the MJO WHI with respect to SLH alone were replicated from prior work. However, when performing the same analysis from CloudSat WALRUS, a less discernable signal emerged from the data that requires further investigation. This has yielded potential avenues of further investigation but also hints at some possible limitations of WALRUS.

It is important to note that, because this analysis is based on observations from a sun-synchronous satellite, the results may be biased due to the sampling time of day and revisit time of the satellite. CloudSat crosses the Equator at 1:30 (AM/PM) local time so the diurnal cycle that exists in warm rain (e.g. Rozendaal et al., 1995) is not completely sampled. Additionally, CloudSat is unable to sense clouds and precipitation below about 1 km due to ground backscatter of the radar signal. This means that warm rain wholly confined to the lowest kilometer of the troposphere is missed by CloudSat (Rapp et al., 2013) and therefore this analysis.

Additionally, the lack of consideration for non-raining profiles or for profiles that are precipitating at rates less than drizzle is a constraint on extending this analysis to a higher time resolution. As an example, clouds with longer lifetimes may yield nonnegligible amounts of latent heating in earlier stages of development without precipitation-sized hydrometeors. This has been known since the first applications of radar data to precipitation methods (e.g. Bergeron, 1960, Miyakoda et al., 1969).

Looking toward warming climates, the environmental dependencies of latent heating and cooling touched on here are likely to have an effect on the warm rain morphologies and distributions that evolve globally. For example, the results suggest that future changes in atmospheric stability are likely to exert a greater impact on the depth of evaporative cooling than the height of maximum latent heating. Yet establishing the true climatology of warm rain is still difficult given the recent launch of CloudSat only a decade ago, its limited sampling with only daytime operations, and its limited remaining lifetime. Future sensors with a high sensitivity to clouds and light rain are therefore important to continuing this important record and further documenting the effects warm rain has on the global climate and the feedbacks therein.

Appendix A

Transport in the Earth System

A.1 Foreword

An underlying theme in the study of warm rain and its effect on the atmosphere is that the clouds and precipitation represent a transfer of energy in the Earth System. Stemming from a graduate seminar on radiation and climate, I served as the lead author and computer for a project assessing the current state of transport representation by climate models, reanalyses, and observations. The following article culminates the result of my work extending well beyond the seminar class to analyze most of the data and synthesize the conclusions.

A.2 Abstract

Modern reanalyses, climate models, and observations are used to assess the energy budgets and transports of the Earth system. Zonal distributions at the top of the atmosphere are similar among the model and observational datasets with a southward transport at the Equator, though differences arise in the calculation of cloud radiative effect. Inferred transports peak on the order of 5-6 PW at the top of the atmosphere. The largest spread between datasets occurs in the separation between surface and atmospheric transports owing to differing estimates of surface turbulent heat fluxes and surface cloud radiative effect. Generally, Southern Hemispheric ocean transports are about half the magnitude of the Northern Hemisphere with one reanalysis implying northward transport across the Equator. There is some spread in the implied atmospheric transport across the Equator, with many climate models indicating Southward movement across the Equator. Nevertheless, the overall distribution and magnitude of energy budgets and transport are converging toward a more unified answer compared to prior studies that used previous generation climate models and reanalyses.

A.3 Introduction

The climate we experience on Earth's surface is a direct result of the way energy from the Sun is intercepted, transformed, redistributed, and ultimately emitted back to space

by the atmosphere. Scientists have been attempting to describe and quantify Earth's energy budget for over a century, with some of the first seminal work stemming from Dines (1917). Scientists have used the knowledge that regional temperatures remain fairly consistent on annual timescales to assume closure when estimating the budget; the amount of energy received from the Sun must approximately balance the energy emitted by the planet. Primitive, simple balances were created using sparse observations and large assumptions, but as computational power and observational technology have improved, the energy budget has been continuously refined (L'Ecuyer et al., 2015, Stephens et al., 2012, Trenberth et al., 2009). The assumption of absolute balance is not necessarily guaranteed in a global warming scenario, where overall less energy is emitted than intercepted (Hansen et al., 2005, Trenberth et al., 2014) and temperatures within the atmospheric column will necessarily increase until top of atmosphere (TOA) balance is regained (Hansen et al., 1997).

More important than the global mean energy balance from the climate perspective are local imbalances that drive atmospheric and oceanic circulations. The orbital and geometric characteristics of Earth produce a gradient of intercepted solar radiation, with more energy received at the Equator than at the poles, that varies over the course of a year. This results in warmer surface temperatures in the low latitudes relative to the high latitudes. However that temperature difference would be significantly larger if it depended only on column incoming and outgoing radiation. The latitudinal gradient of planetary emission is significantly weaker than that of solar absorption, and it is only by

poleward transport of energy in the atmosphere and ocean that regional temperatures can be maintained. This transport is critical for defining atmospheric and oceanic circulations and must be well represented to accurately model the climate system.

Satellites have provided measurements of Earth's TOA incoming and outgoing radiation, allowing for calculations of the total poleward transport required to maintain energy balance. Assuming land does not store or transport an appreciable amount of energy, the total transport can be partitioned between the atmosphere and the ocean. To precisely calculate this partition, global surface energy flux estimates are required. Advances in satellite technology and *in-situ* observational networks have significantly improved global estimates of surface fluxes, however they are not comprehensive. Therefore most current estimates of atmospheric and oceanic energy transports are based on models and reanalyses using relatively sparse measurements for validation and assimilation (Trenberth and Caron, 2001, Yamada and Pauluis, 2015).

Clouds play a critical role in local energy imbalances: increasing the planetary albedo by reflecting incoming solar radiation, trapping outgoing terrestrial emissions, and releasing energy in the atmosphere through latent heat processes. Each of these contributions varies widely depending on cloud microphysics, cloud location, underlying atmosphere, surface characteristics, and so forth–properties which vary spatially and temporally, making them both difficult to measure and difficult to model. As a result, clouds remain a particularly difficult variable to constrain when quantifying the global energy budget (Trenberth et al.,

2009). Despite continued advances in satellite technology, the observational details of global cloud climatology and the feedbacks that occur due to cloud climatology changes are still in flux (Christensen et al., 2013, Spencer and Braswell, 2008, Stephens, 2005, Yu et al., 2017). Furthermore, despite recent advances in numerical models, accurately simulating clouds remains a challenge for global models as well (e.g. Kay et al., 2015, Li et al., 2013). This sort of variability leads to large uncertainties in surface fluxes, transport, and the total effect that clouds have on them (Stephens and Greenwald, 1991).

Despite difficulties constraining surface fluxes, previous studies have used available observations to attempt both a partition of the transport into ocean and atmospheric components (Carissimo et al., 1985, Hastenrath, 1980) with some going so far as to separate the role of cloud radiative effects on the magnitude of those transports (Gleckler et al., 1995, Zhang and Rossow, 1997). While these early studies showed promising agreement in the general character of transport with most datasets implying northward TOA transport across the equator, there were large discrepencies in both the magnitude and the equatorial direction for the partitioned transports, due in large part to the lack of global scale surface observations. Comparisons to contemporary global climate models were also made (Gleckler, 2005, Gleckler et al., 1995), though these early models did not contain dynamic, coupled oceans and the majority had implied northward transport in both hemispheres of the ocean.

Some recent observational studies have shown that cross equatorial heat transport in both

the atmosphere and ocean is northward (Donohoe et al., 2013), though others maintain partitioning results in a northward cross-equatorial transport by the ocean and southward by the atmosphere (Stephens et al., 2016). Regardless of specific conclusions, there is consensus that accurately constraining clouds and their radiative influence, particularly on meridional transport, is one of the large challenges remaining in projecting future climate scenerios (e.g. Bischoff and Schneider, 2014, Bourgeois et al., 2016, Randall et al., 2007, Schneider et al., 2017, Weaver, 2003). In this study we estimate global meridional energy transport as a whole and as divided between the atmosphere and ocean using two modeling projects, three reanalyses, and multiple observational datasets with the goal of determining how much progress there has been towards a unified representation of Earth's energy balance.

A.4 Datasets

The data used in this study includes model, observational and reanalysis datasets to compute the TOA and surface energy balances and transports, as well as all compared to clear sky where available. A brief description of each dataset is described below with the time period, coordinate extent, and spatial resolution, summarized in Table A.1. All model and reanalysis datasets are used over the 1996-2005 time period, while the periods of observations are chosen to overlap this period as much as possible while attempting to retain a ten-year period length.

A.4.1 Model Data

The fifth phase of the Coupled Model Intercomparison Project (CMIP5) is the most recent international group of climate model experiments used for the IPCC AR5 report in order to provide a framework of integrated climate change experiments. Due to the abundance of models used in the CMIP5 analysis, the individual models chosen for analysis that provide all necessary variables are presented in Table A.2. Each model in CMIP5 has its own limitations depending on its modeling parameters, which are described with additional information on the experiment design discussed in Taylor et al. (2012). Only historical runs are included to cover the time period of interest.

The Community Earth System Model (CESM) Large Ensemble project is composed of 30 ensemble members and is a fully coupled atmosphere, ocean, and land and sea ice model using the CAM5, POP2, CLM4 and CICE4 components respectively. Each ensemble was run from 1920 to 2080 with the same model physics and external forcings, but with slightly perturbed (round-off error differences in sea surface temperatures) initial conditions. Each member shows a unique climate trajectory and together they show a spread of possibilities within this particular model climate system. Data for this study uses the ensemble mean. Further details on the CESM Large Ensemble project can be found in Kay et al. (2015).

A.4.2 Observational Data

The Clouds and Earth's Radiant Energy System (CERES) is a satellite instrument developed by NASA and was launched on the Terra and Aqua satellites. CERES supplies radiometric measurements from three broadband channels for TOA and surface longwave, shortwave and net fluxes under clear and all sky conditions (Loeb et al., 2009). CERES Energy Balanced and Filled (EBAF) estimates are derived by applying empirical angular distribution models from high resolution imager based cloud retrievals. The 2.8 version was released in 2014 with improvements to TOA solar radiation estimates. Version 4.0 was released in early 2017 with improved ancillary input for clear sky values and an updated data assimilation core.

Launched in 2006, CloudSat is a sun-synchronous, polar orbiting satellite that is part of the NASA A-Train constellation. The satellites fly at an altitude near 700 km with an inclination of 98.2° (L'Ecuyer and Jiang, 2010). CloudSat is in tight formation with the Cloud-Aerosol Lidar and Infrared Pathfinder Satellite Observation (CALIPSO) satellite; together, CloudSat and CALIPSO provide active radar and lidar sensors to obtain the internal structure of cloud and aerosol layers (Winker et al., 2009). The 2B-FLXHR-LIDAR dataset, which combines data from CloudSat and CALIPSO, is used in order to estimate the downwelling longwave and shortwave flux profiles at the surface and TOA. CloudSat can not measure surface latent and sensible heat fluxes and is therefore augmented with SeaFlux data for the atmospheric and oceanic transport values. Recent

comparisons between CERES and CloudSat TOA fluxes have shown small differences at a 2.5° resolution, with root-mean-square differences at 4.9 W m^{-2} for TOA outgoing longwave radiation and at 8.9 W m^{-2} for TOA outgoing shortwave radiation (Matus and L'Ecuyer, 2017).

Three turbulent flux datasets are compared in part of this work. The SeaFlux project was implemented under the World Climate Research Programme (WCRP) Global Energy and Water Experiment (GEWEX) Data and Assessment Panel (Curry et al., 2004). The sensible and latent heat fluxes are calculated using a neural network emulation of the regional flux product, Tropical Ocean and Global Atmosphere (TOGA) Coupled Ocean Atmosphere Response Experiment (COARE) 3.0 algorithm. The raw near-surface temperature, near-surface humidity and wind speed data are from SSM/I sensors, which were active from 1998 through 2007 (Curry et al., 2004). The Objectively Analyzed Air-Sea Fluxes for the Global Oceans, or OAFlux, project is a surface turblent flux dataset over the ice-free oceans sponsored under the NOAA Climate Observations and Monitoring program. OAFlux blends satellite remote sensing, reanalysis, and oceanic weather observations with an objective analysis approach that minimizes error variance in the process (Yu and Weller, 2007). The Hamburg Ocean Atmosphere Parameters and Fluxes from Satellite Data (HOAPS) is yet another surface turbulent flux dataset. HOAPS turbulent fluxes are derived strictly from SSM/I microwave radiometer measurements (Andersson et al., 2010).

A.4.3 Reanalysis Data

The Modern Era Retrospective-analysis for Research and Applications (MERRA) reanalysis product is generated by the Goddard Earth Observing System Data Assimilation System Version 5 (GOES-5) in order to provide support studies of the hydrological cycle (Rienecker et al., 2011). Examples of previous work on the energy fluxes and transport characteristics of MERRA can be found in the work of Yamada and Pauluis (2015). The second version, MERRA-2, was released in early 2017 and includes not only an updated dynamical core but also automated bias corrections and additional assimilated observations, including aerosols (Gelaro et al., 2017).

The European Center for Medium-range Weather Forecasting (ECMWF) Re-analysis–Interim (ERA-I) is the second successor in the line of ERA products. ERA-I uses a 4D-Var data assimilation technique in a 12-hour update cycle as input to the ECMWF Integrated Forecast System model Dee et al. (2011). Previous ERA products, namely ERA-40, have been used to examine atmospheric transport (Gleckler et al., 2006), yet substantial improvements are present in ERA-Interim compared to ERA-40, resulting from use of the 4D-Var data assimilation scheme, improved model physics (e.g. hydrological cycle, aerosol radiative effects), and bias adjustments of many observational datasets (Dee et al., 2011).

These datasets together represent the state-of-the-art in understanding our atmosphere. Climate models in CMIP5 and also the CESM provide coupling between the atmosphere

and ocean circulations, representing the energy transfer and interactions that occur between them. Reanalyses from MERRA and ERA provide the best model-based global understanding of the likely atmospheric state. And the observations from CloudSat, CESM, and surface fluxes–though not omniscent–provide samplings of the atmospheric state nearly globally. This diversity of sources will allow an evaluation of the current state of transport in the Earth system representation.

A.5 A TOA perspective

Energy balance at the top of the atmosphere (TOA) is simply the balance of radiation coming into and leaving the Earth system:

$$N_{TOA} = R_{TOA} = F_{SW\downarrow TOA} - F_{SW\uparrow TOA} - F_{LW\uparrow TOA}, \tag{A.1}$$

where SW denotes shortwave radiation, LW denotes longwave radiation, and arrows indicate upward or downward fluxes with downward fluxes defined as positive. Energy balance can be computed under both all-sky and clear sky conditions. All-sky conditions are simply those that exist in reality where all grid boxes, whether or not they contain clouds, are included. Clear sky conditions are computed in one of two ways: either by removing clouds from scenes and running a radiative transfer model again or by only selecting grid boxes that do not contain clouds. The cloud radiative effect (CRE), or

cloud forcing, is computed as

$$CRE = R_{all} - R_{clear}. \tag{A.2}$$

The balance of energy at TOA for both all-sky and clear sky conditions, as well as the implied cloud radiative effect, are shown in Figure A.1. TOA energy balance for all sky is a first-order measure the full representation of the atmosphere: the profile of temperature and water vapor in the atmosphere in conjunction with the cloud distribution is ultimately responsible for this value.

Balance at TOA in all-sky conditions (Fig. A.1(a)) is variable among the different datasets. Observations tend to favor higher fluxes in the tropics while reanalyses favor lower values. For the most part, CMIP5 models capture the spread of these variables, with the exception of CloudSat in the vicinity of the Equator. Outside of the tropics in the Northern Hemisphere, the spread among the datasets tends to shrink from about 25 W m^{-2} closer to 15 W m^{-2}. All datasets also capture a local plateau around the 35°N mark. Consistency mostly exists in the Southern Hemisphere with the exception of MERRA2 in the midlatitude regions, yielding a 50% lower flux near 55°S. This feature is likely the result of Southern Ocean stratus representation within the reanalysis data. And, similar to the Northern Hemisphere, datasets are mostly consistent poleward of 60°S.

Derived clear sky TOA energy balance (Fig. A.1(b)) is strictly dependent on the profile of temperature and water vapor in the atmosphere–and not the distribution of clouds–so this value should be easier for models and reanalyses to represent. Indeed, a similar magnitude of spread among the datasets, though in this case, reanalyses and some climate models tend to favor higher values. CESM and a few CMIP5 members remain consistently above all others through the extent of the tropics and subtropics. The bias of MERRA2 in the midlatitude Southern Hemisphere does not exist in clear sky calculations, further supporting the assertion that behavior in all sky conditions is due to cloud cover representation in the Southern Ocean.

The resulting CRE is shown in Figure A.1(c). Large variance remains in the tropical region, with observations favoring lower cloud radiative forcings than reanalyses and many climate models. Moving from the subtropics poleward in each hemisphere, the spread among datasets is reduced as expected from the behavior in Figures A.1(a-b), with the exception of MERRA2 and some CMIP5 members again in the Southern Ocean; compared to the other datasets, these have a much larger cloud radiative effect than others. Overall, datasets reveal a sloped distribution from about 60°S upwards to 60°N.

Individual latitude bands do not collect or lose energy and remain imbalanced–turning into a snowball or fireball. Instead, energy is transported from one latitude to another to balance any imbalance resulting from the radiative inputs and outputs. This is accomplished through the cumulative behavior of "weather" features, namely baroclinic

cyclones, ocean circulations, and so forth. Meridional transport can be calculated by integrating the energy balance in each latitude band from pole to pole:

$$T_{TOA}(\phi) = 2\pi a^2 \int_{-\pi/2}^{\phi} N_{TOA} cos(\phi')\ d\phi', \tag{A.3}$$

where a is the radius of the Earth. However, a problem exists with energy balance in this basic calculation. In the climate models, balance must exist or the model would be unstable. While this is true of the Earth system as well, observations of radiation do not cover every point of the planet at every moment in time. As a result, all of the radiative calculations presented here are not necessarily forced to be in radiative balance. This imbalance is made gravely apparent in the naive calculation of transports in Figure A.2 as the integral starting from the South Pole does not reach 0 at the North Pole. This excess energy or deficit of energy implied at the North Pole should not be confused with some storage of energy in the Arctic region, but rather a fundamental issue with radiative closure constraints. In a warming climate on long enough time scales there will be some inbalance of energy, but for the time length inspected here that term is not large. Thus, a scaling of the energy budget needs to occur to restore balance.

To correct this imbalance, the remainder at the North Pole in Figure A.2, detailed in Table A.3, is distributed zonally with area weighting to the TOA all-sky fluxes. Recalculated fluxes are displayed in Figure A.3(a). Spread among the different datasets is reduced with the scaling. The dip in MERRA2 in the Southern Hemisphere has been somewhat

reduced, while a new one is introduced in CloudSat around 20°S. CloudSat was designed to have a particular sensitivity to clouds and light precipitation beyond traditional satellites, and this signal could be stemming from enhanced observation of stratocumulus clouds.

This rebalancing procedure cannot necessarily be applied to clear sky conditions. Indeed, clouds do have an effect on the surrounding atmosphere and surface beyond their immediate area. This means they can keep a planet similar to Earth's present state with clouds instantaneously removed or ignored from not having any storage of energy. One example of this is the effect of clouds on the Greenland ice sheet. It is the presence of clouds that warm the surface and has been shown to enhance melt the ice compared to clear sky conditions (van Tricht et al., 2015). When clouds are instantaneously removed from the atmosphere during clear sky radiative calculations, their integrated effect on the surface budget is neglected and thus an unnatural source of heating or cooling may be introduced. Nevertheless, the closest measure we have of clouds' effects on the environment is the cloud radiative effect term. We therefore scale the clear sky TOA energy balance in Figure A.1(b) by the same amount as the all-sky (Figure A.3(a)) to ensure cloud forcing (Figure A.3(c)) remains the same in the new energy balance.

Transport at TOA in all-sky conditions with energy balanced is shown in Figure A.4. The structure of transport is similar among all the datasets, peaking between 4-6 PW in both hemispheres, with climate models favoring higher values in the Northern Hemisphere, reanalyses in the Southern Hemisphere, and observations about equal. Climate model

and observation magnitudes remain above reanalyses in the Northern Hemisphere, while observation and MERRA reanalysis magnitudes are lower in the Southern Hemisphere. Maximum transport values in each hemisphere are listed in Table A.4.

One of the greatest disparities between the datasets is the implied transport at the Equator: all reanalyses and one CMIP5 model imply southward transport at the Equator while all other datasets imply northward transport across the Equator. In other words, reanalyses are implying that the combined effect of atmospheric and oceanic transport is a movement of energy from a surplus in the Southern Hemisphere to the Northern Hemisphere, while the others are the reverse. This result could stem from the nature of reanalyses: though they implement a dynamical core similar to global models, their state variables are forced by observations every few hours and the physical processes resulting are based on the parameterizations that occur therein. These results line up with previous work for reanalyses in Mayer and Haimberger (2012) and observations tend to follow those presented in Stephens et al. (2016).

A.6 The surface

Energy balance at the surface is not as straightforward as TOA. Firstly, there is an additional radiative component of downwelling longwave radiation since the atmosphere is emitting longwave radiation not only to space but also to the surface. This term is

added to the radiative balance at the surface:

$$R_{SFC} = F_{SW\downarrow SFC} - F_{SW\uparrow SFC} + F_{LW\downarrow SFC} - F_{LW\uparrow SFC}. \tag{A.4}$$

Secondly, turbulent heat fluxes serve as another pathway of energy exchange either to or from the surface. These processes–latent and sensible heat (respectively, LE and SH)–must be included with radiation in the surface energy balance:

$$N_{SFC} = R_{SFC} - LE - SH. \tag{A.5}$$

Climate models and reanalyses natively provide radiative and turbulent heat flux calculations since they simulate the complete Earth system. Observational estimates, however, are more complex. Satellite measurements from the CERES and CloudSat missions are able to estimate radiative fluxes at the surface through the use of cloud and radiation measurements coupled to radiative transfer models. Turbulent heat fluxes require very localized observations of atmospheric and oceanic state variables–temperature, wind, and humidity–and are thus more difficult to obtain by remote sensing. Surface observational datasets exist that can be combined with satellite observations to obtain the surface energy budget, albeit without a unified perspective.

The radiative balance alone at the surface is displayed in Figure A.5(a). The overall shape of the distribution is similar between the datasets, with an asymmetry among the

hemispheres where the Southern Hemisphere peaks at a higher magnitude and a distance closer to the Equator than the Northern Hemisphere. Higher spread again occurs in the tropical regions, while the variance is much lower in the midlatitudes. Antarctica poses a challenge in the surface radiative balance as some satellite measurements actually turn positive over the continent.

Combining radiative balance at the surface with turbulent heat fluxes does not directly lead to an intuitive transport calculation because land cannot transport energy over long distances unlike the ocean. To calculate a surface transport, we must concern ourselves only with the energy balance and implied transport from that balance over the ocean. This is achieved by removing values over land; when this is performed, the quantity will be referred to as "oceanic" instead of "surface":

$$N_{OCN} = R_{OCN} - LE_{OCN} - SH_{OCN}. \tag{A.6}$$

For reanalyses, the supplied land and land-ice fraction are used to determine if a grid box contains land. CESM also uses a native land mask. CMIP5 uses a generated land mask that is applied similarly to each model. Observational radiative datasets remove areas of no data from the respectively combined surface turbulent flux datasets. From Table A.1, both CERES versions are combined with OAFlux given their similar resolution. Figure A.5(b) shows the zonal mean land fraction used by each dataset. Differences are most apparent in polar regions, where some models do not include areas of sea ice for part of

the year as land. Though it is out of the scope of this paper to examine differences that result from this treatment, the use of dataset-specific land masks ensures that calculations here are consistent with model physics representing ocean versus land.

Oceanic turbulent heat fluxes are shown in Figure A.5(c). The zonal structure is similar among the datasets, though there are particularly large differences in the Antarctic region with observational datasets containing much more noise, while a separation is prevalent between climate models and observations in the subtropics with the latter lower.

The oceanic energy balance in all-sky conditions is shown in Figure A.6(a). Recall differences between this and the surface radiative balance are due to the exclusion of land areas and addition of turbulent heat fluxes. Patterns in the zonal structure are consistent between most of the datasets: a strong peak just south of the Equator and secondary peaks in the midlatitudes of both hemispheres between 40^{o} and 60^{o}. Observations are consistently higher in the tropics with a marked peak centered around 10^{o}N. MERRA2 has an additional deviation in Southern Hemispheric values particularly in the midlatitudes. It is of particular interest to also keep in mind that observational datasets qualitatively have a larger uncertainty in the oceanic energy balance due to the combination of quantities from separate sources.

Clear sky oceanic energy balance in Figure A.6(b) has a more consistent shape among the datasets. Note that turbulent heat fluxes are only computed in all-sky conditions because it is difficult to disentangle these surface processes from near-surface fluxes in

the presence of clouds, but are still used in these calculations while the clear sky radiative fluxes are used. Spread has decreased across the whole zonal distribution save one CMIP5 member that is much lower throughout the tropics and subtropics. The resulting cloud forcing is shown in Figure A.6(c). Spread is somewhat larger than at TOA, though one CMIP5 member has reduced over the full extent and both MERRA reanalyses are closer to others in the Southern Hemisphere.

The oceanic transport is calculated similarly to TOA in Equation A.3 by integrating the energy balance at each latitude from pole to pole, though the area used is only that of the ocean in a given band:

$$T_{OCN}(\phi) = 2\pi a^2 \int_{-\pi/2}^{\phi} N_{OCN}\mathcal{F}(\phi')cos(\phi')\ d\phi', \tag{A.7}$$

where $\mathcal{F}(\phi)$ the fraction of ocean at a given latitude.

Implied oceanic transport for all-sky conditions is calculated from these transports (Fig. A.7). These transports do not integrate to 0 at the North Pole, just as the TOA transports did not either (Fig. A.2). So, the all-sky ocean remainders shown in Table A.3 are distributed based on the area of ocean that exists in a given latitude since areas over land have been removed. The recalculated fluxes for oceanic energy balance in all-sky conditions is shown in Figure A.8(a) and clear sky conditions in Figure A.8(b).

Resulting oceanic transport in balance is shown in Figure A.9. The zonal pattern varies

among the datasets, with some peaking more in the midlatitudes than the subtropics in the Northern Hemisphere. In the Southern Hemisphere, some imply there are regions of net northward transport by the ocean. MERRA2 is the only dataset that implies southward transport across the Equator, while others favor northward. Oceanic dynamics are especially difficult to represent in any instance due to the sparse observations available even to this day, so it stands to reason there is not significant agreement among different dynamical cores or observations. Peaks in each hemisphere's midlatitude regions are marked for all of the datasets in the core of the Hadley Cell. This behavior follows similar results from Stephens et al. (2016), Trenberth and Caron (2001).

A.7 The atmosphere

Transport by the atmosphere is the residual of transport implied by the TOA energy balance and transport by the ocean,

$$T_{ATM}(\phi) = 2\pi a^2 \int_{-\pi/2}^{\phi} N_{TOA} - (N_{OCN}\mathcal{F}(\phi'))cos(\phi')\ d\phi', \tag{A.8}$$

which is shown in Figure A.10. Differences that arise in both the TOA and oceanic transports will continue to show up in the atmospheric transport. Most of the CMIP5 models show a northward transport across the Equator, while reanalyses, observations, and some climate models indicate a southward transport. These results are in line with other work for reanalyses (Trenberth and Caron, 2001), though their behavior is indeed different from others.

A.7.1 Equilibrium latitude of forcing

It is not enough to determine only the implied direction of transport across the Equator in diagnosing the behavior of the climate system. The equilibrum latitude of forcing, or ELF, indicates the latitude at which transport is poleward on either side. In a world where both hemispheres are precisely equal in every respect, the ELF would be situated at the Equator meaning transport north of the Equator would be northward and transport south of the Equator would be southward. However, it is not the case that each hemisphere is actually equal in the real Earth system. Conceptually, the ELF should represent the latitude at which air converges at the surface, convects, and is transported poleward aloft (e.g. Holton et al., 1971)–namely, the ascending branch of the Hadley Cell. Observational studies have consistently found the ITCZ to have an annual mean location that favors the northern side of the Equator (e.g Waliser and Gautier, 1993, Wodzicki and Rapp, 2016).

Derived ELF for each of the datasets in this study on all-sky atmospheric transport is shown in Figure A.11, with many north of the Equator. Observations are near 4^{o}N, ERA-Interim and MERRA sit near 6^{o}N, MERRA2 is much lower near 1^{o}N, CESM is similar to the observations near 4^{o}N, and CMIP5 models range from 6^{o}S to 3^{o}N. We speculate the placement of ELF in the Southern Hemisphere by CMIP5 models could be responsible for the presence of the double ITCZ in some general circulation models (de Szoeke and Xie, 2008, Mechoso et al., 1995).

A.8 Discussion

A comparison of energy balance and meridional transport for TOA, the ocean, and residually the atmosphere was completed using modern observations, renalyses, and climate models. After accounting for and redistributing accumulated energy in transport calculations, TOA energy balance among all of the datasets is consistent in clear sky conditions and nearly as consistent in all sky conditions. Large variability exists in TOA cloud forcing among the datasets, with observations favoring smaller magnitudes and some reanalyses favoring larger magnitudes. Implied all sky transport at TOA reveals all reanalyses show southward transport across the Equator, while observations and the majority of climate models dictate northward transport. A single climate model indicates no cross-equatorial transport.

Energy balance over the oceans reveals very noisy behavior outside of the Equatorial region. All datasets replicate a general trend of a slight increase around 10°N, local maxima in the midlatitude regions between 40° and 60° in both hemispheres, and a secondary peak between 60°N and 70°N. Nevertheless, the magnitudes are greatly variable due to the representation of surface CRE since the clear sky oceanic balance is much more consistent. Balanced oceanic transport in all sky conditions has a similar pattern among the datasets, but the magnitudes are wide ranging, with ERA-Interim and some climate models showing northward transport from 40°S-50°S. With the exception of MERRA2, a northward cross-Equatorial transport is implied by each of the datasets.

Atmospheric transport in all sky conditions, defined as the residual between TOA all-sky and oceanic all-sky energy transport, shows a very predictable pattern of strongest poleward transport centered in each hemispheric Hadley Cell. The magnitude of the peak varies, with Northern Hemispheric peaks ranging from 3.5-5.5 PW and Southern Hemispheric peaks from 4-6 PW. Climate models tend to favor larger transport in the Northern Hemisphere and smaller transport in the Southern Hemisphere compared to reanalyses and observations. CESM, reanalyses, observations, and some CMIP5 models show a southward cross-Equatorial transport in the atmosphere, while the rest of the CMIP5 models indicate northward flowing. ELF computed in reanalyses and observations is found to be north of the Equator, while there is spread across the climate models.

Two pathways of improvement in the future are suggested from this work. The first is improving CRE both at TOA and particularly at the surface, which requires an accurate representation of cloud morphology and extent over the full globe, given that clear sky energy balances are much more consistent than all sky (Figs. A.3(b,c) and A.8(a,b)). This is evidenced by agreement between all datasets in clear sky conditions. The second is consistency in surface turbulent heat fluxes, which show differences up to 20% between observations and models in much of the subtropics and midlatitudes (Fig. A.5(c)).

TABLE A.1: Radiative and turbulent heat flux datasets used in this study.

	Dataset	Version	Horizontal Resolution	Time Period	Notes
Climate models	CMIP	5	$0.25° \times 0.25°$	1996–2005	[a,b]
	CESM		$\sim 0.9° \times \sim 0.9°$	1996–2005	
Reanalyses	MERRA	1.0	$0.5° \times 0.\overline{6}°\times$	1996–2005	
	MERRA	2.0	$0.5° \times 0.625°$	1996–2005	
	ERA-I		$0.5° \times 0.5°$	1996–2005	
Observations	CERES	2.8	$1.0° \times 1.0°$	2000–2010	[c]
	CERES	4.0	$1.0° \times 1.0°$	2000–2010	[d]
	CloudSat	R05	$2.5° \times 2.5°$	2007–2010	[e]
	HOAPS	3.2	$0.5° \times 0.5°$	1996–2005	[e]
	OAFLUX	3	$1.0° \times 1.0°$	1996–2005	[c,d]
	SeaFlux	1.0	$0.25° \times 0.25°$	1998–2007	

[a]See Table A.2 for full list of models. [b]All models regridded to common resolution. [c]Combined. [d]Combined. [e]Data available between $|80°|$.

TABLE A.2: List of CMIP-5 model datasets used in this study.

ACCESS1.0, ACCESS1.3, BCC-CSM1.1, BCC-CSM1.1(m), BNU-ESM, CCSM4, CESM1 (FASTCHEM), CESM1 (WACCM), CNRM-CM5, CNRM-CM5-2, CSIRO-Mk3.6.0, CanESM2, GFDL-CM3, GFDL-ESM2G, GFDL-ESM2M, GISS-E2-H, GISS-E2-H-CC, GISS-E2-R, GISS-E2-R-CC, HadCM3, HadGEM2-CC, HadGEM2-ES, INM-CM4, IPSL-CM5A-LR, IPSL-CM5A-MR, IPSL-CM5B-LR, MIROC-ESM, MIROC-ESM-CHEM, MIROC4h, MIROC5, MPI-ESM-LR, MPI-ESM-MR, MPI-ESM-P, MRI-CGCM3, MRI-ESM1, NorESM1-M, NorESM1-ME

TABLE A.3: Remainder terms after initial transport integration for different levels in all sky conditions [W m^{-2}].

Dataset	TOA	Ocean	Atmo
CERES 2.8	0.74	15.59	-14.85
CERES 4	0.74	16.14	-15.39
CESM	3.77	1.27	2.50
CloudSat	9.12		
CMIP5 Mean	0.99	1.22	-0.22
ERA-I	-1.44	5.75	-7.20
MERRA	0.48	10.02	-9.54
MERRA2	-3.58	-3.88	0.30

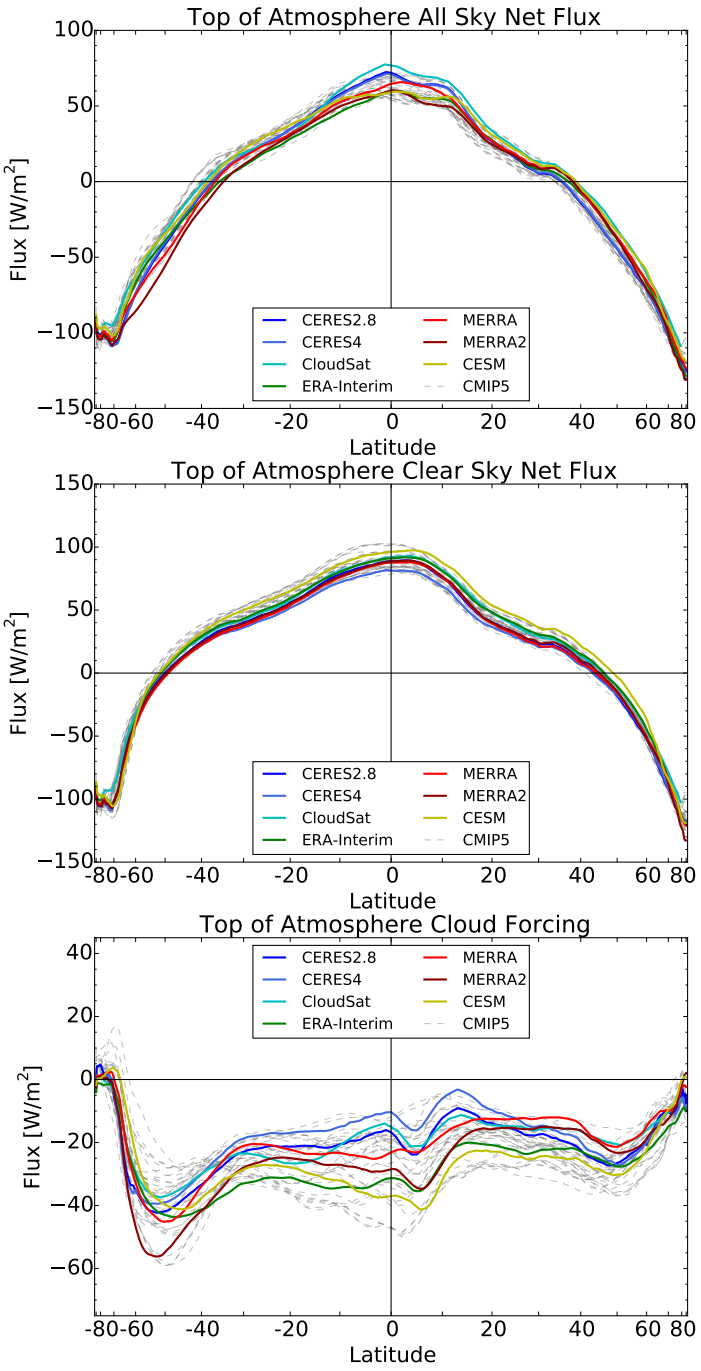

FIGURE A.1: Zonal mean top of the atmosphere (a) all sky energy balance, (b) clear sky energy balance, and (c) cloud forcing.

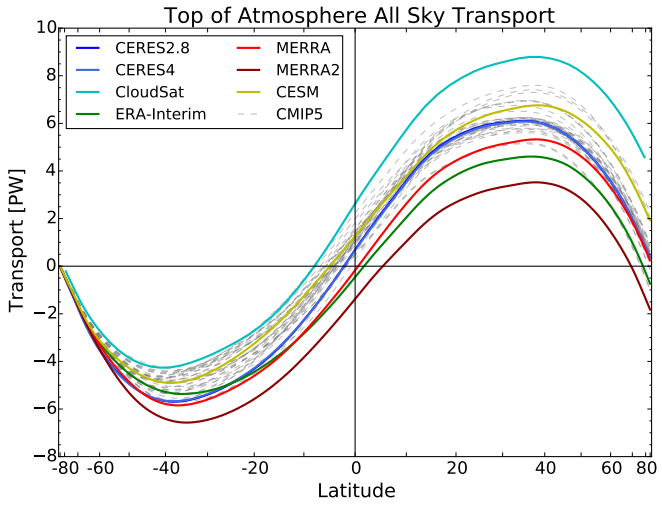

FIGURE A.2: Top of the atmosphere implied all sky meridional transport by the energy balance in Figure A.1(a).

TABLE A.4: Maximum balanced transport integration values for different levels in all sky conditions [PW].

Dataset	TOA SH	TOA NH	Ocean SH	Ocean NH	Atmo SH	Atmo NH
CERES 2.8	5.77	5.80	1.34	1.97	5.34	4.66
CERES 4	5.75	5.78	1.41	2.14	5.11	4.49
CESM	5.28	5.20	0.68	1.68	5.16	4.22
Cloudsat	5.13	5.11				
CMIP5 Mean	5.02	5.81	0.64	1.52	4.96	4.99
ERA-I	5.22	5.20	0.68	1.58	5.20	4.48
MERRA	5.90	5.13	1.49	1.72	4.56	3.84
MERRA2	6.18	5.01	1.27	0.87	5.34	4.51

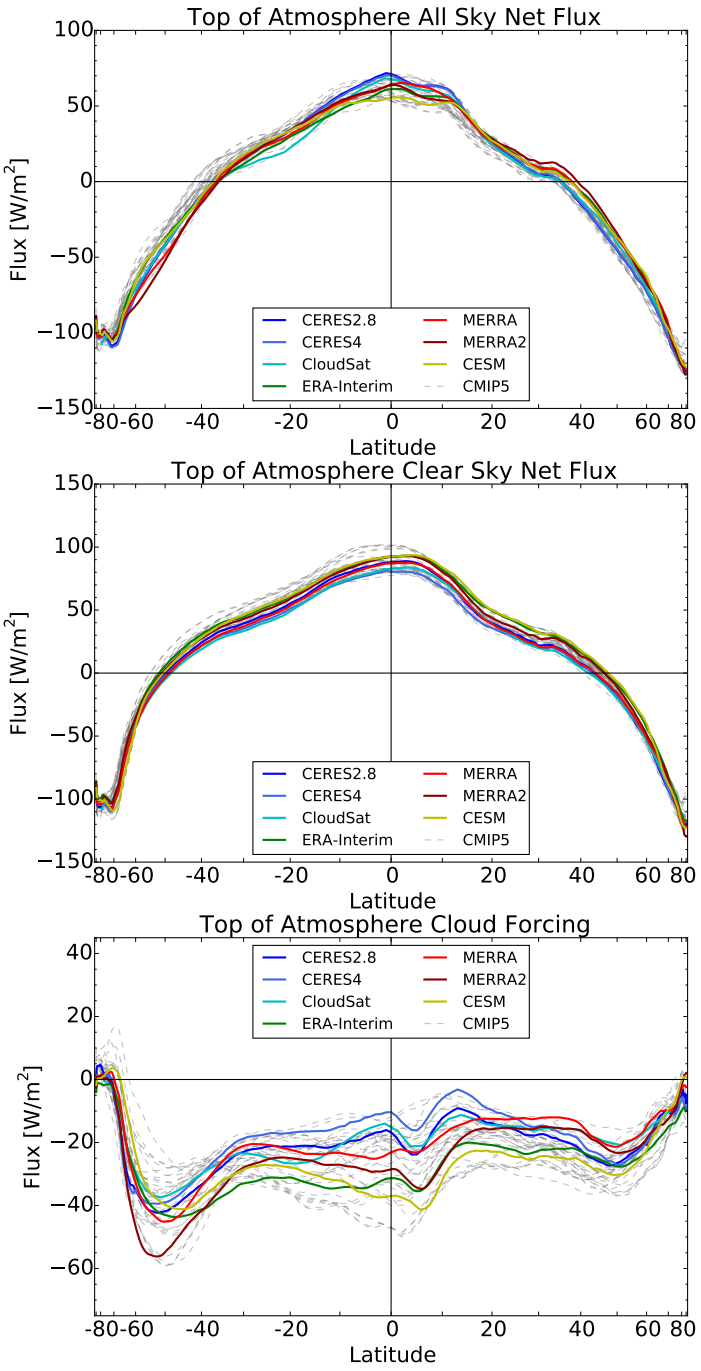

FIGURE A.3: As in Figure A.1 but scaled by the meridional transport remainder in Figure A.2.

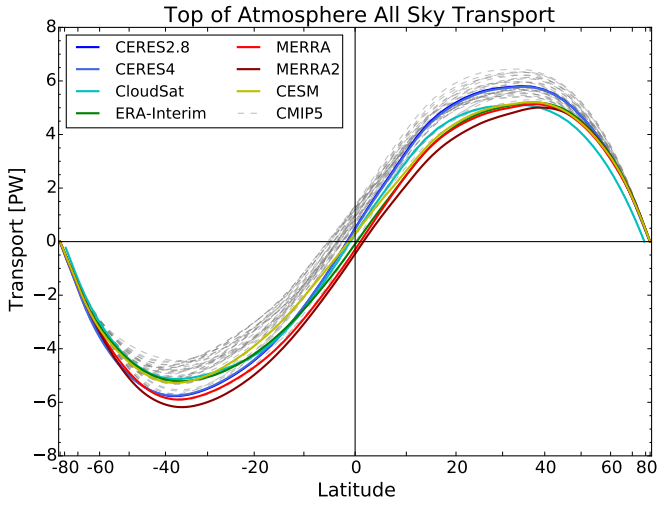

FIGURE A.4: As in Figure A.2 but of the scaled energy balance in Figure A.3(a).

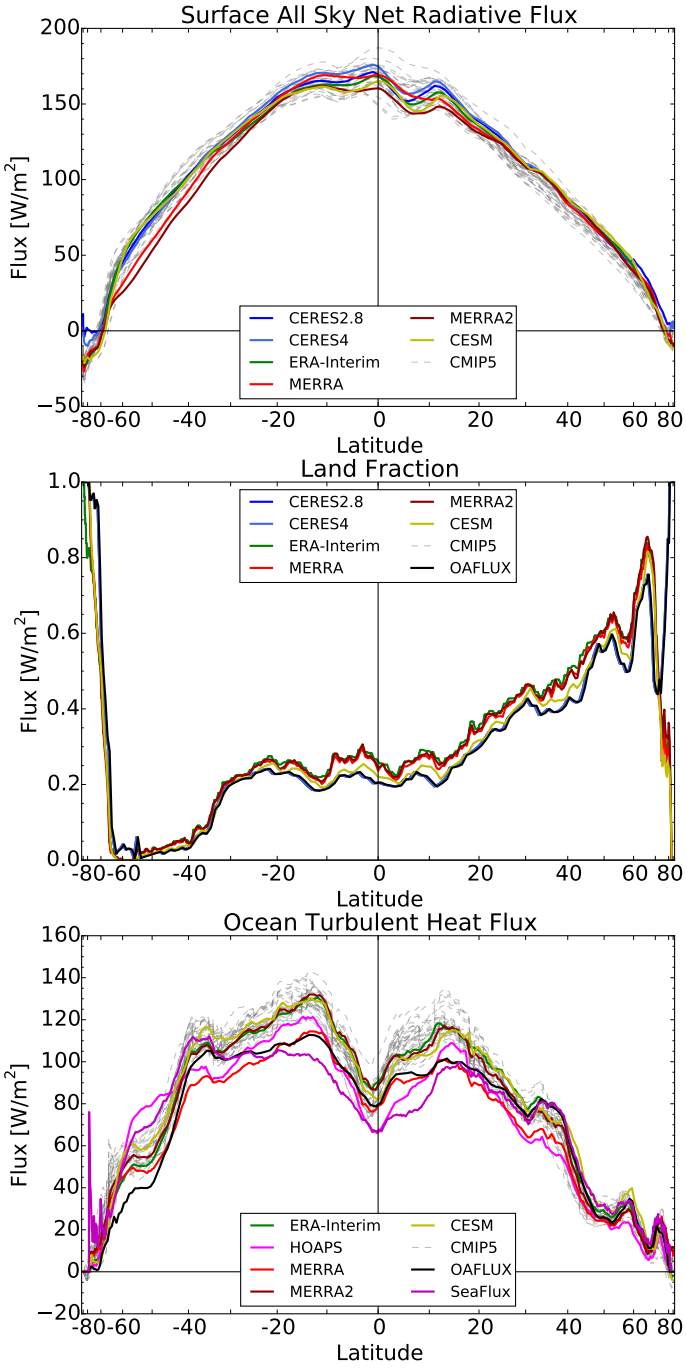

FIGURE A.5: Zonal mean (a) all sky surface radiative balance, (b) zonal land fraction, and (c) turbulent heat fluxes over the ocean.

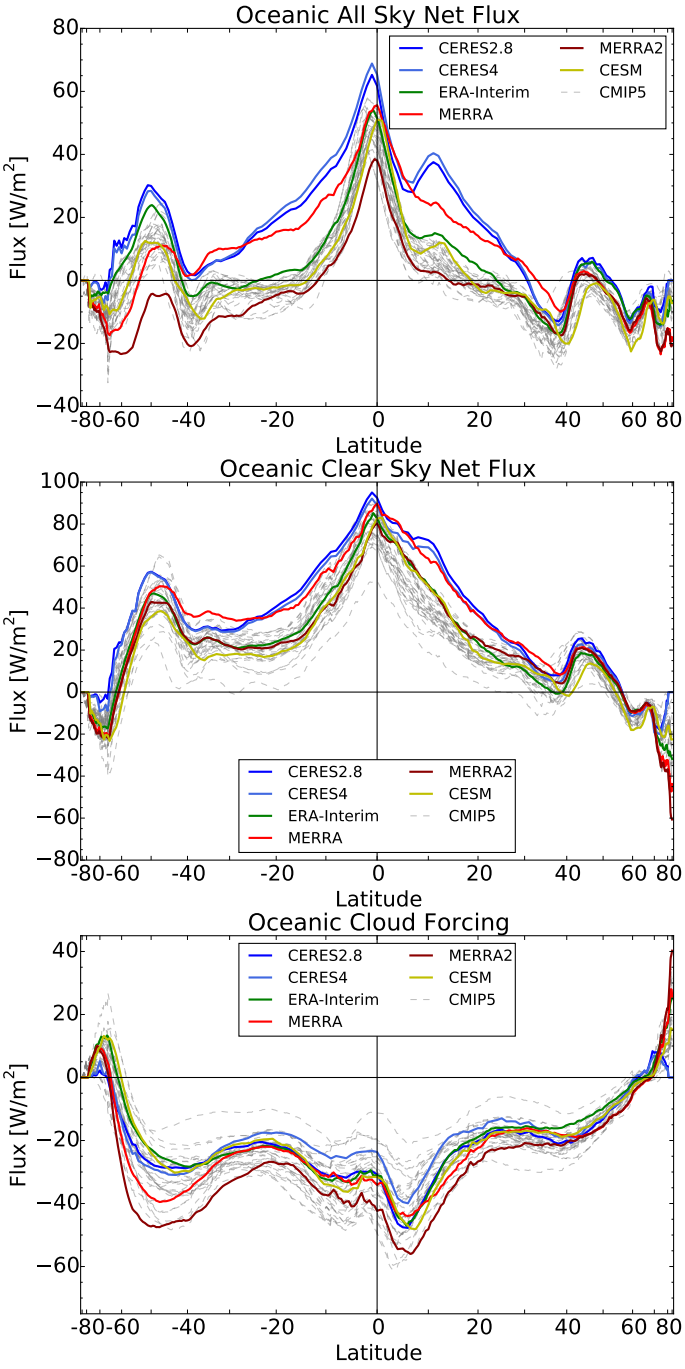

FIGURE A.6: Zonal mean (a) all sky oceanic energy balance, (b) clear sky oceanic energy balance, and (c) oceanic cloud forcing.

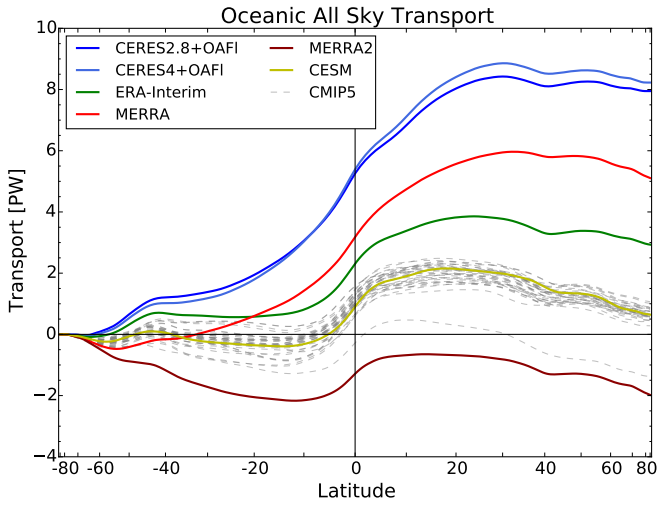

FIGURE A.7: Oceanic implied all sky meridional transport by the all sky oceanic energy balance in Figure A.6(a).

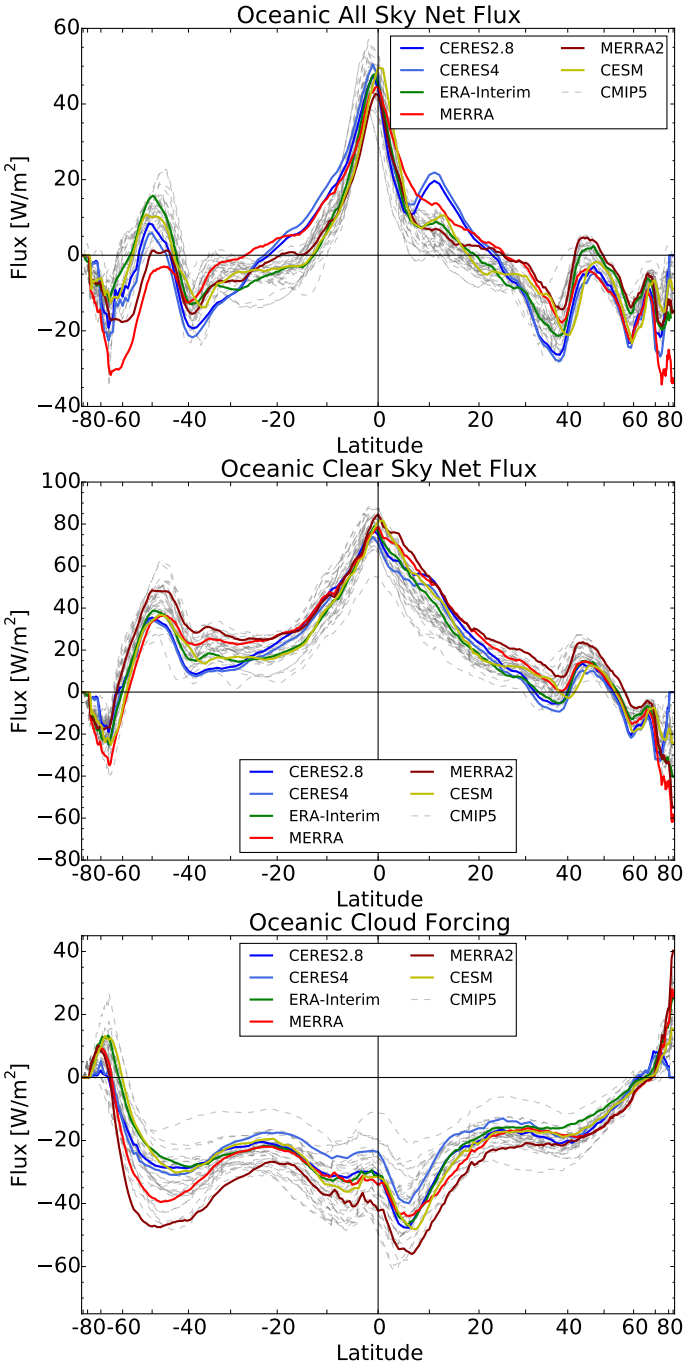

FIGURE A.8: As in Figure A.6 but scaled by the meridional transport remainder in Figure A.7.

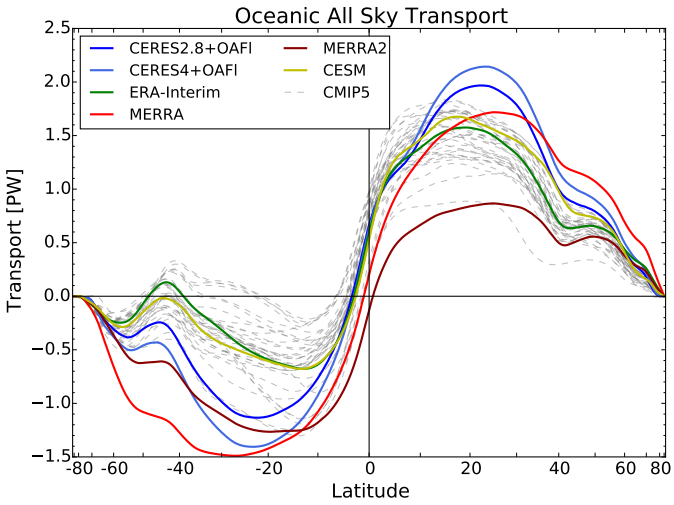

FIGURE A.9: As in Figure A.7 but of the scaled energy balance in Figure A.8(a).

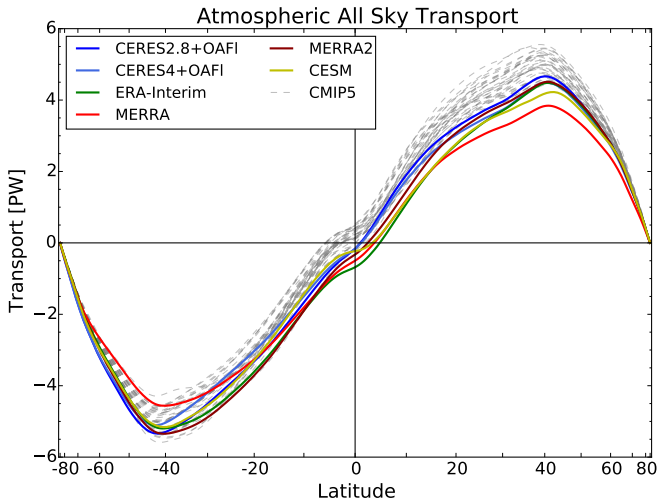

FIGURE A.10: Implied atmospheric meridional transport based on the residual between Figures A.3(a) and A.8(a).

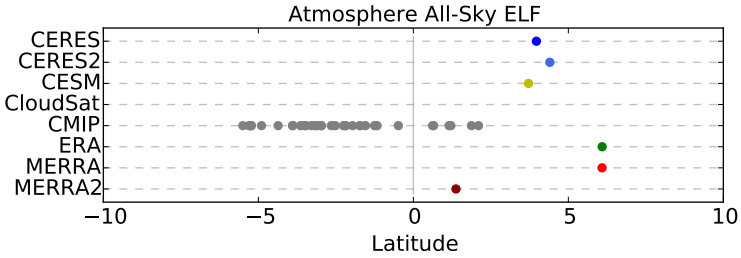

FIGURE A.11: Equilibrium latitude of forcing of the atmosphere in all-sky conditions.

Bibliography

Abbot, C. G. and L. B. Aldrich, 1917: The pyranometer–an instrument for measuring sky radiation. *Smithsonian Misc. Coll.*, **66**, 1–9.
URL `https://archive.org/details/smithsonianmisce661917smit`

Ackerman, B., 1956: Buoyancy and precipitation in tropical cumuli. *J. Meteor.*, **13**, 302–310, doi:10.1175/1520-0469(1956)013<0302:BAPITC>2.0.CO;2.

Adler, R. F., G. J. Huffman, A. Chang, R. Ferraro, P.-P. Xie, J. Janowiak, B. Rudolf, U. Schneider, S. Curtis, D. Bolvin, A. Gruber, J. Susskind, P. Arkin, and E. Nelkin, 2003: The version-2 Global Precipitation Climatology Project (GPCP) monthly precipitation analysis (1979–Present). *J. Hydrometeor.*, **4**, 1147–1167, doi:10.1175/1525-7541(2003)004<1147:TVGPCP>2.0.CO;2.

Albrecht, B. A., D. A. Randall, and S. Nicholls, 1988: Observations of marine stratocumulus clouds during FIRE. *Bull. Amer. Meteor. Soc.*, **69**, 618–626, doi:10.1175/1520-0477(1988)069<0618:OOMSCD>2.0.CO;2.

Andersson, A., K. Fennig, C. Klepp, S. Bakan, H. Graßl, and J. Schulz, 2010: The hamburg ocean atmosphere parameters and fluxes from satellite data–hoaps-3. *Earth Syst. Sci. Data*, **2**, 215–234, doi:10.5194/essd-2-215-2010.

Atlas, D., ed., 1990: *Radar in Meteorology: Battan Memorial and 40th anniversary radar meteorology conference*. American Meteorological Society, Boston.

Augstein, E., H. Schmidt, and F. Ostapoff, 1974: The vertical structure of the atmospheric planetary boundary layer in undisturbed trade winds over the Atlantic Ocean. *Boundary-Layer Meteor.*, **6**, 129–150, doi:10.1007/BF00232480.

Back, L. E. and C. S. Bretherton, 2006: Geographic variability in the export of moist static energy and vertical motion profiles in the tropical pacific. *Geophys. Res. Lett.*, **33**, L17810, doi:10.1029/2006GL026672.

Barrett, E. C., 1970: The estimation of monthly rainfall from satellite data. *Mon. Wea. Rev.*, **98**, 322–327, doi:10.1175/1520-0493(1970)098<0322:TEOMRF>2.3.CO;2.

Battan, L. J. and R. R. Braham, 1956: A study of convective precipitation based on cloud and radar observations. *J. Meteor.*, **13**, 587–591, doi:10.1175/1520-0469(1956)013<0587:ASOCPB>2.0.CO;2.

Behrangi, A., M. Lebsock, S. Wong, and B. Lambrigtsen, 2012: On the quantification of oceanic rainfall using spaceborne sensors. *J. Geophys. Res.*, **117**, D20105, doi:10.1029/2012JD017979.

Berg, W., T. L'Ecuyer, and J. M. Haynes, 2010: The distribution of rainfall over oceans from spaceborne radars. *J. Appl. Meteor. Climatol.*, **49**, 535–543, doi:10.1175/2009JAMC2330.1.

Bergeron, T., 1960: Problems and methods of rainfall investigation: Address of the honorary chairman of the conference. *Physics of Precipitation: Proceedings of the Cloud Physics Conference, Woods Hole, Massachusetts, June 3-5, 1959*, H. Weickmann, ed., American Geophysical Union, Washington, D.C., 5–30.

Bischoff, T. and T. Schneider, 2014: Energetic constraints on the position of the Intertropical Convergence Zone. *J. Climate*, **27**, 4937–4951, doi:10.1175/JCLI-D-13-00650.1.

Blossey, P. N., C. S. Bretherton, A. Cheng, S. Endo, T. Heus, A. P. Lock, and J. J. van der Dussen, 2016: CGILS Phase 2 LES intercomparison of response of subtropical marine low cloud regimes to CO2 quadrupling and a CMIP3 composite forcing change. *J. Adv. Model. Earth Sys.*, **8**, 1714–1726, doi:10.1002/2016MS000765.
URL `http://dx.doi.org/10.1002/2016MS000765`

Bony, S. and J.-L. Dufresne, 2005: Marine boundary layer clouds at the heart of tropical cloud feedback uncertainties in climate models. *Geophys. Res. Lett.*, **32**, L20B06, doi:10.1029/2005GL023851.

Boucher, O., D. Randall, P. Artaxo, C. Bretherton, G. Feingold, P. Forster, V.-M. Kerminen, Y. Kondo, H. Liao, U. Lohmann, P. Rasch, S. Satheesh, S. Sherwood, B. Stevens, and X. Zhang, 2013: Clouds and aerosols. *Climate Change 2013: The Physical Science Basis. Contribution of Working Group I to the Fifth Assessment Report of the Intergovernmental Panel on Climate Change*, T. Stocker, D. Qin, G.-K. Plattner, M. Tignor, S. Allen, J. Boschung, A. Nauels, Y. Xia, V. Bex, and P. Midgley, eds., Cambridge University Press, Cambridge, United Kingdom, 571–658.

Bourgeois, Q., A. M. L. Ekman, M. R. Igel, and R. Krejci, 2016: Ubiquity and impact of thin mid-level clouds in the tropics. *Nature Comms.*, **7**, 12432.

Bretherton, C. S., P. N. Blossey, and C. R. Jones, 2013: Mechanisms of marine low cloud sensitivity to idealized climate perturbations: A single-LES exploration extending the CGILS cases. *J. Adv. Model. Earth Sys.*, **5**, 316–337, doi:10.1002/jame.20019.

Brient, F., T. Schneider, Z. Tan, S. Bony, X. Qu, and A. Hall, 2016: Shallowness of tropical low clouds as a predictor of climate models' response to warming. *Climate Dyn.*, **47**, 433–449, doi:10.1007/s00382-015-2846-0.

Byers, H. R. and R. K. Hall, 1955: A census of cumulus-cloud height versus precipitation in the vicinity of Puerto Rico during the winter and spring of 1953-1954. *J. Meteor.*, **12**, 176–178, doi:10.1175/1520-0469(1955)012<0176:ACOCCH>2.0.CO;2.

Carissimo, B. C., A. H. Oort, and T. H. V. Haar, 1985: Estimating the meridional energy transports in the atmosphere and ocean. *J. Phys. Oceanogr.*, **15**, 82–91, doi:10.1175/1520-0485(1985)015<0082:ETMETI>2.0.CO;2.

Cess, R. D., G. L. Potter, J. P. Blanchet, G. J. Boer, A. D. Del Genio, M. Déqué, V. Dymnikov, V. Galin, W. L. Gates, S. J. Ghan, J. T. Kiehl, A. A. Lacis, H. Le Treut, Z.-X. Li, X.-Z. Liang, B. J. McAvaney, V. P. Meleshko, J. F. B. Mitchell, J.-J. Morcrette, D. A. Randall, L. Rikus, E. Roeckner, J. F. Royer, U. Schlese, D. A. Sheinin, A. Slingo, A. P. Sokolov, K. E. Taylor, W. M. Washington, R. T. Wetherald, I. Yagai, and M.-H. Zhang, 1990: Intercomparison and interpretation of climate feedback processes in 19 atmospheric general circulation models. *J. Geophys. Res.*, **95**, 16601–16615, doi:10.1029/JD095iD10p16601.

Christensen, M. W., G. L. Stephens, and M. D. Lebsock, 2013: Exposing biases in retrieved low cloud properties from CloudSat: A guide for evaluating observations and climate data. *J. Geophys. Res.*, **118**, 12120–12131, doi:10.1002/2013JD020224.

Chung, D. and J. Teixeira, 2012: A simple model for stratocumulus to shallow cumulus cloud transitions. *J. Climate*, **25**, 2547–2554, doi:10.1175/JCLI-D-11-00105.1.

Curry, J., A. Bentamy, M. Bourassa, D. Bourras, E. F. Bradley, M. Brunke, S. Castro, S. Chou, C. Clayson, W. Emery, et al., 2004: Seaflux. *Bull. Amer. Meteor. Soc.*, **85**, 409–424.

Daloz, A., E. L. Nelson, T. S. L'Ecuyer, A. D. Rapp, and L. Sun, 2017: Assessing the coupled influences of clouds on the atmospheric energy and water cycles in reanalyses with A-Train observations. *J. Climate*, in preparation.

de Szoeke, S. P. and S.-P. Xie, 2008: The Tropical Eastern Pacific seasonal cycle: Assessment of errors and mechanisms in IPCC AR4 Coupled Ocean–Atmosphere General Circulation Models. *J. Climate*, **21**, 2573–2590, doi:10.1175/2007JCLI1975.1.

Dee, D. P., S. M. Uppala, A. J. Simmons, P. Berrisford, P. Poli, S. Kobayashi, U. Andrae, M. A. Balmaseda, G. Balsamo, P. Bauer, P. Bechtold, A. C. M. Beljaars, L. van de Berg, J. Bidlot, N. Bormann, C. Delsol, R. Dragani, M. Fuentes, A. J. Geer, L. Haimberger, S. B. Healy, H. Hersbach, E. V. Hólm, L. Isaksen, P. Kallberg, M. Köhler, M. Matricardi, A. P. McNally, B. M. Monge-Sanz, J.-J. Morcrette, B.-K. Park, C. Peubey,

P. de Rosnay, C. Tavolato, J.-N. Thépaut, and F. Vitart, 2011: The ERA-Interim reanalysis: Configuration and performance of the data assimilation system. *Quart. J. Roy. Meteor. Soc.*, **137**, 553–597, doi:10.1002/qj.828.

DeMoss, J. D. and K. P. Bowman, 2007: Changes in TRMM rainfall due to the orbit boost estimated from buoy rain gauge data. *J. Atmos. Oceanic Technol.*, **24**, 1598–1607, doi:10.1175/JTECH2082.1.

Dicke, R. H., 1946: The measurement of thermal radiation at microwave frequencies. *Rev. Sci. Inst.*, **17**, 268–275, doi:10.1063/1.1770483.

Dines, W. H., 1917: The heat balance of the atmosphere. *Quart. J. Roy. Meteor. Soc.*, **43**, 151–158, doi:10.1002/qj.49704318203.

Donohoe, A., J. Marshall, D. Ferreira, and D. Mcgee, 2013: The relationship between ITCZ location and cross-equatorial atmospheric heat transport: From the seasonal cycle to the last glacial maximum. *J. Climate*, **26**, 3597–3618, doi:10.1175/JCLI-D-12-00467.1.

Douglas, C. K. M., 1934: The physical processes of cloud formation. *Quart. J. Roy. Meteor. Soc.*, **60**, 333–344, doi:10.1002/qj.49706025607.

Dubach, L. L. and C. Ng, 1988: Compendium of meteorological space programs, satellites, and experiments. Technical report, National Aeronautics and Space Administration, Goddard Space Flight Center.
URL `https://ntrs.nasa.gov/archive/nasa/casi.ntrs.nasa.gov/19900009927.pdf`

Dufresne, J.-L. and S. Bony, 2008: An assessment of the primary sources of spread of global warming estimates from coupled atmosphere-ocean models. *J. Climate*, **21**, 5135–5144, doi:10.1175/2008JCLI2239.1.

Ebert, E. E., M. J. Manton, P. A. Arkin, R. J. Allam, C. E. Holpin, and A. Gruber, 1996: Results from the GPCP algorithm intercomparison programme. *Bull. Amer. Meteor. Soc.*, **77**, 2875–2887, doi:10.1175/1520-0477(1996)077<2875:RFTGAI>2.0.CO;2.

Eccles, P. J. and E. A. Mueller, 1971: X-band attenuation and liquid water content estimation by a dual-wavelength radar. *J. Appl. Meteor.*, **10**, 1252–1259, doi:10.1175/1520-0450(1971)010<1252:XBAALW>2.0.CO;2.

Ellis, T. D., T. S. L'Ecuyer, J. M. Haynes, and G. L. Stephens, 2009: How often does it rain over the global oceans? The perspective from CloudSat. *Geophys. Res. Lett.*, **36**, L03815, doi:10.1029/2008GL036728.

Findeisen, W., 1938: Die kolloidmeteorologischen vorgänge bei der niederschlagsbildung. *Meteor. Z.*, **55**, 121–133, translated and edited by E. Volken, A.M. Giesche, S. Brönnimann (2015). *Meteor. Z.*, **24**, doi:10.1127/metz/2015/0675.

Fraser, L. W., 1985: High altitude research at the Applied Physics Laboratory in the 1940s. *Johns Hopkins Applied Physics Laboratory Tech, Dig,*, **6**, 92–99.
URL `http://techdigest.jhuapl.edu/views/pdfs/V06_N1_1985/V6_N1_1985_Fraser.pdf`

Gelaro, R., W. McCarty, M. J. Suárez, R. Todling, A. Molod, L. Takacs, C. A. Randles, A. Darmenov, M. G. Bosilovich, R. Reichle, K. Wargan, L. Coy, R. Cullather, C. Draper, S. Akella, V. Buchard, A. Conaty, A. M. da Silva, W. Gu, G.-K. Kim, R. Koster, R. Lucchesi, D. Merkova, J. E. Nielsen, G. Partyka, S. Pawson, W. Putman, M. Rienecker, S. D. Schubert, M. Sienkiewicz, and B. Zhao, 2017: The Modern-Era Retrospective Analysis for Research and Applications, Version 2 (MERRA-2). *J. Climate*, **30**, 5419–5454, doi:10.1175/JCLI-D-16-0758.1.

Gleckler, P. J., 2005: Surface energy balance errors in AGCMs: Implications for ocean-atmosphere model coupling. *Geophys. Res. Lett.*, **32**, L15708, doi:10.1029/2005GL023061.

Gleckler, P. J., D. A. Randall, G. Boer, R. Colman, M. Dix, V. Galin, M. Helfand, J. Kiehl, A. Kitoh, W. Lau, X.-Y. Liang, V. Lykossov, B. McAvaney, K. Miyakoda, S. Planton, and W. Stern, 1995: Cloud-radiative effects on implied oceanic energy transports as simulated by Atmospheric General Circulation Models. *Geophys. Res. Lett.*, **22**, 791–794, doi:10.1029/95GL00113.

Gleckler, P. J., K. R. Sperber, and K. AchutaRao, 2006: Annual cycle of global ocean heat content: Observed and simulated. *J. Geophys. Res.*, **111**, C06008, doi:10.1029/2005JC003223.

Grabowski, W. W. and M. W. Moncrieff, 2004: Moisture-convection feedback in the tropics. *Quart. J. Roy. Meteor. Soc.*, **130**, 3081–3104.

Hanel, R. A., J. Licht, W. Nordberg, R. A. Stampfl, and W. G. Stroud, 1960: The satellite Vanguard II: Cloud Cover Experiment. *IRE Trans. Mil. Elect.*, **MIL-4**, 245–247, doi:10.1109/IRET-MIL.1960.5008229.

Hansen, J., L. Nazarenko, R. Ruedy, M. Sato, J. Willis, A. Del Genio, D. Koch, A. Lacis, K. Lo, S. Menon, T. Novakov, J. Perlwitz, G. Russell, G. A. Schmidt, and N. Tausnev, 2005: Earth's energy imbalance: Confirmation and implications. *Science*, **308**, 1431–1435, doi:10.1126/science.1110252.

Hansen, J., M. Sato, and R. Ruedy, 1997: Radiative forcing and climate response. *J. Geophys. Res.*, **102**, 6831–6864, doi:10.1029/96JD03436.

Hartmann, D. L., H. H. Hendon, and R. A. Houze, 1984: Some implications of the mesoscale circulations in tropical cloud clusters for large-scale dynamics and climate. *J. Atmos. Sci.*, **41**, 113–121, doi:10.1175/1520-0469(1984)041<0113:SIOTMC>2.0.CO;2.

Hastenrath, S., 1980: Heat budget of tropical ocean and atmosphere. *J. Phys. Oceanogr.*, **10**, 159–170, doi:10.1175/1520-0485(1980)010<0159:HBOTOA>2.0.CO;2.

Haynes, J. M., T. S. L'Ecuyer, G. L. Stephens, S. D. Miller, C. Mitrescu, N. B. Wood, and S. Tanelli, 2009: Rainfall retrieval over the ocean with spaceborne W-band radar. *J. Geophys. Res.*, **114**, D00A22, doi:10.1029/2008JD009973.

Haynes, J. M., Z. Luo, G. L. Stephens, R. T. Marchand, and A. Bodas-Salcedo, 2007: A multipurpose radar simulation package: QuickBeam. *Bull. Amer. Meteor. Soc.*, **88**, 1723–1727, doi:10.1175/BAMS-88-11-1723.

Henderson, D. S., T. LEcuyer, G. Stephens, P. Partain, and M. Sekiguchi, 2013: A multisensor perspective on the radiative impacts of clouds and aerosols. *J. Appl. Meteor. Climatol.*, **52**, 853–871, doi:10.1175/JAMC-D-12-025.1.

Heymsfield, G. M., B. Geerts, and L. Tian, 2000: TRMM Precipitation Radar reflectivity profiles as compared with high-resolution airborne and ground-based radar measurements. *J. Appl. Meteor.*, **39**, 2080–2102, doi:10.1175/1520-0450(2001)040<2080:TPRRPA>2.0.CO;2.

Heywood, G. S. P., 1940: Rain formation in the tropics. *Quart. J. Roy. Meteor. Soc.*, **66**, 46, doi:10.1002/qj.49706628307.

Holland, J. Z. and E. M. Rasmusson, 1973: Measurements of the atmospheric mass, energy, and momentum budgets over a 500-kilometer square of tropical ocean. *Mon. Wea. Rev.*, **101**, 44–55, doi:10.1175/1520-0493(1973)101<0044:MOTAME>2.3.CO;2.

Holton, J. R., J. M. Wallace, and J. A. Young, 1971: On boundary layer dynamics and the ITCZ. *J. Atmos. Sci.*, **28**, 275–280, doi:10.1175/1520-0469(1971)028<0275:OBLDAT>2.0.CO;2.

Huffman, G. J., R. F. Adler, P. Arkin, A. Chang, R. Ferraro, A. Gruber, J. Janowiak, A. McNab, B. Rudolf, and U. Schneider, 1997: The Global Precipitation Climatology Project (GPCP) combined precipitation dataset. *Bull. Amer. Meteor. Soc.*, **78**, 5–20, doi:10.1175/1520-0477(1997)078¡0005:TGPCPG¿2.0.CO;2.

Huffman, G. J., R. F. Adler, D. T. Bolvin, and G. Gu, 2009: Improving the global precipitation record: GPCP version 2.1. *Geophys. Res. Lett.*, **36**, L17808, doi:10.1029/2009GL040000.

Illingworth, A. J., H. W. Barker, A. Beljaars, M. Ceccaldi, H. Chepfer, N. Clerbaux, J. Cole, J. Delanoë, C. Domenech, D. P. Donovan, S. Fukuda, M. Hirakata, R. J. Hogan, A. Huenerbein, P. Kollias, T. Kubota, T. Nakajima, T. Y. Nakajima, T. Nishizawa, Y. Ohno, H. Okamoto, R. Oki, K. Sato, M. Satoh, M. W. Shephard, A. Velázquez-Blázquez, U. Wandinger, T. Wehr, and G.-J. van Zadelhoff, 2015: The EarthCARE

Satellite: The next step forward in global measurements of clouds, aerosols, precipitation, and radiation. *Bull. Amer. Meteor. Soc.*, **96**, 1311–1332, doi:10.1175/BAMS-D-12-00227.1.

Jakob, C., 2010: Accelerating progress in global atmospheric model development through improved parameterizations. *Bull. Amer. Meteor. Soc.*, **91**, 869–876, doi:10.1175/2009BAMS2898.1.

Jiang, X., D. E. Waliser, W. S. Olson, W.-K. Tao, T. S. L'Ecuyer, K.-F. Li, Y. L. Yung, S. Shige, S. Lang, and Y. N. Takayabu, 2011: Vertical diabatic heating structure of the MJO: Intercomparison between recent reanalyses and TRMM estimates. *Mon. Wea. Rev.*, **139**, 3208–3223, doi:10.1175/2011MWR3636.1.

Johnson, R. H. and P. E. Ciesielski, 2000: Rainfall and radiative heating rates from TOGA COARE atmospheric budgets. *J. Atmos. Sci.*, **57**, 1497–1514, doi:10.1175/1520-0469(2000)057<1497:RARHRF>2.0.CO;2.

Kahn, A. B., 1957: A generalization of average-correlation methods of spectrum analysis. *J. Meteor.*, **14**, 9–17, doi:10.1175/0095-9634-14.1.9.

Kay, J. E., C. Deser, A. Phillips, A. Mai, C. Hannay, G. Strand, J. M. Arblaster, S. C. Bates, G. Danabasoglu, J. Edwards, M. Holland, P. Kushner, J. F. Lamarque, D. Lawrence, K. Lindsay, A. Middleton, E. Munoz, R. Neale, K. Oleson, L. Polvani, and M. Vertenstein, 2015: The Community Earth System Model (CESM) Large Ensemble Project: A community resource for studying climate change in the presence of internal climate variability. *Bull. Amer. Meteor. Soc.*, **96**, 1333–1349, doi:10.1175/BAMS-D-13-00255.1.

Keys, D. J., 2010: Wilkinson Microwave Anisotropy Probe (WMAP) battery operations Problem Resolution Team (PRT). Technical report, National Aeronautics and Space Administration, Greenbelt, Maryland, nASA/TM-2010-216840, NESC-RP-10-00608. URL `https://ntrs.nasa.gov/archive/nasa/casi.ntrs.nasa.gov/20100030608.pdf`

Kidder, S. Q. and T. H. Vonder Haar, 1995: *Satellite meteorology*. Academic Press, San Diego, 466 pp. pp.

Kikuchi, K. and Y. N. Takayabu, 2004: The development of organized convection associated with the MJO during TOGA COARE IOP: Trimodal characteristics. *Geophys. Res. Lett.*, **31**, L10101, doi:10.1029/2004GL019601.

Kikuchi, K., B. Wang, and Y. Kajikawa, 2012: Bimodal representation of the tropical intraseasonal oscillation. *Climate Dyn.*, **38**, 1989–2000, doi:10.1007/s00382-011-1159-1.

Klein, S. A. and D. L. Hartmann, 1993: The seasonal cycle of low stratiform clouds. *J. Climate*, **6**, 1587–1606, doi:10.1175/1520-0442(1993)006<1587:TSCOLS>2.0.CO;2.

Kummerow, C., J. Simpson, O. Thiele, W. Barnes, A. T. C. Chang, E. Stocker, R. F. Adler, A. Hou, R. Kakar, F. Wentz, P. Ashcroft, T. Kozu, Y. Hong, K. Okamoto, T. Iguchi, H. Kuroiwa, E. Im, Z. Haddad, G. Huffman, B. Ferrier, W. S. Olson, E. Zipser, E. A. Smith, T. T. Wilheit, G. North, T. Krishnamurti, and K. Nakamura, 2000: The status of the Tropical Rainfall Measuring Mission (TRMM) after two years in orbit. *J. Appl. Meteor.*, **39**, 1965–1982, doi:10.1175/1520-0450(2001)040<1965:TSOTTR>2.0.CO;2.

Langley, S. P., 1900: *Annals of the Astrophysical Observatory of the Smithsonian Institute. Volume I.*. Government Printing Office, Washington, D.C.
URL `https://hdl.handle.net/2027/hvd.32044077087641`

Larson, K., D. L. Hartmann, and S. A. Klein, 1999: The role of clouds, water vapor, circulation, and boundary layer structure in the sensitivity of the tropical climate. *J. Climate*, **12**, 2359–2374, doi:10.1175/1520-0442(1999)012<2359:TROCWV>2.0.CO;2.

Lebsock, M. D. and T. S. L'Ecuyer, 2011: The retrieval of warm rain from CloudSat. *J. Geophys. Res.*, **116**, D20209, doi:10.1029/2011JD016076.

L'Ecuyer, T. S., H. K. Beaudoing, M. Rodell, W. Olson, B. Lin, S. Kato, C. A. Clayson, E. Wood, J. Sheffield, R. Adler, G. Huffman, M. Bosilovich, G. Gu, F. Robertson, P. R. Houser, D. Chambers, J. S. Famiglietti, E. Fetzer, W. T. Liu, X. Gao, C. A. Schlosser, E. Clark, D. P. Lettenmaier, and K. Hilburn, 2015: The observed state of the energy budget in the Early Twenty-First Century. *J. Climate*, **28**, 8319–8346, doi:10.1175/JCLI-D-14-00556.1.

L'Ecuyer, T. S. and J. H. Jiang, 2010: Touring the atmosphere aboard the A-Train. *Phys. Today*, **63**, 36–41.

L'Ecuyer, T. S. and G. L. Stephens, 2002: An estimation-based precipitation retrieval algorithm for attenuating radars. *J. Appl. Meteor.*, **41**, 272–285, doi:10.1175/1520-0450(2002)041<0272:AEBPRA>2.0.CO;2.

Leslie, J., 1804: *An experimental inquiry into the nature of propagation of heat*. Printed for J. Mawman, London, 562 pp. pp.

Lhermitte, R., 1973: Meteorological Doppler radar. *Science*, **182**, 258–262, doi:10.1126/science.182.4109.258.

Li, J.-L. F., D. E. Waliser, G. Stephens, S. Lee, T. L'Ecuyer, S. Kato, N. Loeb, and H.-Y. Ma, 2013: Characterizing and understanding radiation budget biases in CMIP3/CMIP5 GCMs, contemporary GCM, and reanalysis. *J. Geophys. Res.*, **118**, 8166–8184, doi:10.1002/jgrd.50378.

Li, L., G. M. Heymsfield, L. Tian, and P. E. Racette, 2005: Measurements of ocean surface backscattering using an airborne 94-ghz cloud radar—implication for calibration of airborne and spaceborne w-band radars. *J. Atmos. Oceanic Technol.*, **22**, 1033–1045, doi:10.1175/JTECH1722.1.

Lilly, D. K., 1968: Models of cloud-topped mixed layers under a strong inversion. *Quart. J. Roy. Meteor. Soc.*, **94**, 292–309, doi:10.1002/qj.49709440106.

Liu, C. and E. J. Zipser, 2005: Global distribution of convection penetrating the tropical tropopause. *J. Geophys. Res.*, **110**, D23104, doi:10.1029/2005JD006063.

— 2009: "Warm rain" in the Tropics: Seasonal and regional distributions based on 9 yr of TRMM data. *J. Climate*, **22**, 767–779, doi:10.1175/2008JCLI2641.1.

Liu, P., Q. Zhang, C. Zhang, Y. Zhu, M. Khairoutdinov, H.-M. Kim, C. Schumacher, and M. Zhang, 2016: A revised real-time multivariate MJO index. *Mon. Wea. Rev.*, **144**, 627–642, doi:10.1175/MWR-D-15-0237.1.

Loeb, N. G., B. A. Wielicki, D. R. Doelling, G. L. Smith, D. F. Keyes, S. Kato, N. Manalo-Smith, and T. Wong, 2009: Toward optimal closure of the Earth's top-of-atmosphere radiation budget. *J. Climate*, **22**, 748–766, doi:10.1175/2008JCLI2637.1.

Madden, R. A. and P. R. Julian, 1971: Detection of a 40-50 day oscillation in the zonal wind in the tropical pacific. *J. Atmos. Sci.*, **28**, 702–708, doi:10.1175/1520-0469(1971)028<0702:DOADOI>2.0.CO;2.

— 1972: Description of global-scale circulation cells in the tropics with a 40-50 day period. *J. Atmos. Sci.*, **29**, 1109–i1123, doi:10.1175/1520-0469(1972)029<1109:DOGSCC>2.0.CO;2.

Mapes, B. E., P. E. Ciesielski, and R. H. Johnson, 2003: Sampling errors in rawinsonde-array budgets. *J. Atmos. Sci.*, **60**, 2697–2714, doi:10.1175/1520-0469(2003)060<2697:SEIRB>2.0.CO;2.

Marchand, R., G. G. Mace, T. Ackerman, and G. Stephens, 2008: Hydrometeor detection using Cloudsat: An Earth-orbiting 94-GHz cloud radar. *J. Atmos. Oceanic Technol.*, **25**, 519–533, doi:10.1175/2007JTECHA1006.1.

Matus, A. V. and T. S. L'Ecuyer, 2017: The role of cloud phase in earth's radiation budget. *J. Geophys. Res.*, **122**, 2559–2578, doi:10.1002/2016JD025951.

Mayer, M. and L. Haimberger, 2012: Poleward atmospheric energy transports and their variability as evaluated from ECMWF reanalysis data. *J. Climate*, **25**, 734–752, doi:10.1175/JCLI-D-11-00202.1.

Maynard, R. H., 1945: Radar and weather. *J. Meteor.*, **2**, 214–226, doi:10.1175/1520-0469(1945)002<0214:RAW>2.0.CO;2.

Mechoso, C., A. Robertson, N. Barth, M. Davey, P. Delecluse, P. Gent, S. Ineson, B. Kirtman, M. Latif, H. L. Treut, T. Nagai, J. Neelin, S. Philander, J. Polcher, P. Schopf, T. Stockdale, M. Suarez, L. Terray, O. Thual, and J. Tribbia, 1995: The seasonal cycle over the Tropical Pacific in coupled ocean–atmosphere general circulation models. *Mon. Wea. Rev.*, **123**, 2825–2838, doi:10.1175/1520-0493(1995)123<2825:TSCOTT>2.0.CO;2.

Mechoso, C. R., R. Wood, R. Weller, C. S. Bretherton, A. D. Clarke, H. Coe, C. Fairall, J. T. Farrar, G. Feingold, R. Garreaud, C. Grados, J. McWilliams, S. P. de Szoeke, S. E. Yuter, and P. Zuidema, 2014: Ocean-cloud-atmosphere-land interactions in the Southeastern Pacific: The VOCALS program. *Bull. Amer. Meteor. Soc.*, **95**, 357–375, doi:10.1175/BAMS-D-11-00246.1.

Medeiros, B. and B. Stevens, 2011: Revealing differences in GCM representations of low clouds. *Climate Dyn.*, **36**, 385–399, doi:10.1007/s00382-009-0694-5.

Mitrescu, C., T. L'Ecuyer, J. Haynes, S. Miller, and J. Turk, 2010: Cloudsat precipitation profiling algorithm—model description. *J. Appl. Meteor. Climatol.*, **49**, 991–1003, doi:10.1175/2009JAMC2181.1.

Miyakoda, K., J. Smagorinsky, R. F. Strickler, and G. D. Hembree, 1969: Experimental extended predictions with a nine-level hemispheric model. *Mon. Wea. Rev.*, **97**, 1–76, doi:10.1175/1520-0493(1969)097<0001:EEPWAN>2.3.CO;2.

Nakamura, K., K. Okamoto, T. Ihara, J. Awaka, T. Kozu, and T. Manabe, 1990: Conceptual design of rain radar for the tropical rainfall measuring mission. *Int. J. Sat. Comms.*, **8**, 257–268, doi:10.1002/sat.4600080318.

NASA Orbital Debris Program Office, 2015: Re-entry and risk assessment for the Tropical Rainfall Measuring Mission (TRMM).
URL `https://trmm.gsfc.nasa.gov/publications_dir/TRMM_Reentry_Risk_Assessment_FINAL_20150604.pdf`

Nayak, M., M. Witkowski, D. Vane, T. Livermore, M. Rokey, M. Barthuli, I. J. Gravseth, B. Pieper, A. Rodzinak, S. Silva, and P. Woznick, 2012: Cloudsat anomaly recovery and operational lessons learned. Technical report, California Institute of Technology, Jet Propulsion Laboratory.
URL `http://www.dtic.mil/dtic/tr/fulltext/u2/a568401.pdf`

Nelson, E. L., T. S. L'Ecuyer, S. M. Saleeby, W. Berg, S. R. Herbener, and S. C. van den Heever, 2016: Toward an algorithm for estimating latent heat release in warm rain systems. *J. Atmos. Oceanic Technol.*, **33**, 1309–1329, doi:10.1175/JTECH-D-15-0205.1.

Newell, B., 1982: *The history of photography: From 1839 to present*. Museum of Modern Art, New York.

Nuijens, L., B. Medeiros, I. Sandu, and M. Ahlgrimm, 2015: The behavior of trade-wind cloudiness in observations and models: The major cloud components and their variability. *J. Adv. Model. Earth Sys.*, **7**, 600–616, doi:10.1002/2014MS000390.

Nuijens, L., B. Stevens, and A. P. Siebesma, 2009: The environment of precipitating shallow cumulus convection. *J. Atmos. Sci.*, **66**, 1962–1979, doi:10.1175/2008JAS2841.1.

Park, S., 2014: A unified convection scheme (unicon). part ii: Simulation. *J. Atmos. Sci.*, **71**, 3931–3973, doi:10.1175/JAS-D-13-0234.1.

Petty, G. W., 1999: Prevalence of precipitation from warm-topped clouds over Eastern Asia and the Western Pacific. *J. Climate*, **12**, 220–229, doi:10.1175/1520-0442-12.1.220.

Rainbird, A. F., 1969: Some potential applications of meteorological satellites in flood forecasting. *Proceedings of the WMO/Unesco Symposium on Hydrological Forecasting*, World Meteorological Organization, Secretariat of the World Meteorolgoical Organization, 73–80.
URL `http://unesdoc.unesco.org/images/0007/000731/073130eo.pdf`

Randall, D., R. Wood, S. Bony, R. Colman, T. Fichefet, J. Fyfe, V. Kattsov, A. Pitman, J. Shukla, J. Srinivasan, R. Stouffer, A. Sumi, and K. Taylor, 2007: Climate models and their evaluation. *Climate Change 2007: The physical science basis. Contribution of Working Group I to the Fourth Assessment Report of the Intergovernmental Panel on Climate Change*, S. Solomon, D. Qin, M. Manning, Z. Chen, M. Marquis, K. Averyt, M.Tignor, and H. Miller, eds., Cambridge University Press, Cambridge, 589–662.

Rapp, A. D., M. Lebsock, and T. L'Ecuyer, 2013: Low cloud precipitation climatology in the southeastern Pacific marine stratocumulus region using CloudSat. *Env. Res. Lett.*, **8**, 014027.

Rauber, R. M., H. T. O. III, L. D. Girolamo, S. Göke, E. Snodgrass, B. Stevens, C. Knight, J. B. Jensen, D. H. Lenschow, R. A. Rilling, D. C. Rogers, J. L. Stith, B. A. Albrecht, P. Zuidema, A. M. Blyth, C. W. Fairall, W. A. Brewer, S. Tucker, S. G. Lasher-Trapp, O. L. Mayol-Bracero, G. Vali, B. Geerts, J. R. Anderson, B. A. Baker, R. P. Lawson, A. R. Bandy, D. C. Thornton, E. Burnet, J.-L. Brenguier, L. Gomes, P. R. A. Brown, P. Chuang, W. R. Cotton, H. Gerber, B. G. Heikes, J. G. Hudson, P. Kollias, S. K. Krueger, L. Nuijens, D. W. O'Sullivan, A. P. Siebesma, and C. H. Twohy, 2007: Rain in shallow cumulus over the ocean: The rico campaign. *Bull. Amer. Meteor. Soc.*, **88**, 1912–1928, doi:10.1175/BAMS-88-12-1912.

Reed, R. J. and E. E. Recker, 1971: Structure and properties of synoptic-scale wave disturbances in the Equatorial Western Pacific. *J. Atmos. Sci.*, **28**, 1117–1133, doi:10.1175/1520-0469(1971)028<1117:SAPOSS>2.0.CO;2.

Rémillard, J., P. Kollias, E. Luke, and R. Wood, 2012: Marine boundary layer cloud observations in the azores. *J. Climate*, **25**, 7381–7398, doi:10.1175/JCLI-D-11-00610.1.

Rienecker, M. M., M. J. Suarez, R. Gelaro, R. Todling, J. Bacmeister, E. Liu, M. G. Bosilovich, S. D. Schubert, L. Takacs, G.-K. Kim, S. Bloom, J. Chen, D. Collins, A. Conaty, A. da Silva, W. Gu, J. Joiner, R. D. Koster, R. Lucchesi, A. Molod, T. Owens, S. Pawson, P. Pegion, C. R. Redder, R. Reichle, F. R. Robertson, A. G. Ruddick, M. Sienkiewicz, and J. Woollen, 2011: MERRA: NASA's Modern-Era Retrospective Analysis for Research and Applications. *J. Climate*, **24**, 3624–3648, doi:10.1175/JCLI-D-11-00015.1.

Rosenthal, S. L., 1960: Some estimates of the power spectra of large-scale disturbances in low latitudes. *J. Meteor.*, **17**, 259–263, doi:10.1175/1520-0469(1960)017<0259:SEOTPS>2.0.CO;2.

Rozendaal, M. A., C. B. Leovy, and S. A. Klein, 1995: An observational study of diurnal variations of marine stratiform cloud. *J. Climate*, **8**, 1795–1809, doi:10.1175/1520-0442(1995)008<1795:AOSODV>2.0.CO;2.

Ryde, J. W., 1946: The attenuation of centimetre radio waves and the echo intensities resulting from atmospheric phenomena. *J. Inst. Elec. Eng. - Part IIIA: Radiolocation*, **93**, 101–103, doi:10.1049/ji-3a-1.1946.0029.

Saleeby, S. M., S. R. Herbener, S. C. van den Heever, and T. S. L'Ecuyer, 2015: Impacts of cloud droplet nucleating aerosols on shallow tropical convection. *J. Atmos. Sci.*, **72**, 1369–1385, doi:10.1175/JAS-D-14-0153.1.

Sandu, I. and B. Stevens, 2011: On the factors modulating the stratocumulus to cumulus transitions. *J. Atmos. Sci.*, **68**, 1865–1881, doi:10.1175/2011JAS3614.1.

Schneider, S. H., 1972: Cloudiness as a global climatic feedback mechanism: The effects on the radiation balance and surface temperature of variations in cloudiness. *J. Atmos. Sci.*, **29**, 1413–1422, doi:10.1175/1520-0469(1972)029<1413:CAAGCF>2.0.CO;2.

Schneider, T., J. Teixeira, C. S. Bretherton, F. Brient, K. G. Pressel, C. Schär, and A. P. Siebesma, 2017: Climate goals and computing the future of clouds. *Nature Climate Change*, **7**, 3–5, doi:10.1038/nclimate3190.

Schumacher, C., M. H. Zhang, and P. E. Ciesielski, 2007: Heating structures of the TRMM field campaigns. *J. Atmos. Sci.*, **64**, 2593–2610, doi:10.1175/JAS3938.1.

Seliga, T. A. and V. N. Bringi, 1976: Potential use of radar differential reflectivity measurements at orthogonal polarizations for measuring precipitation. *J. Appl. Meteor.*, **15**, 69–76, doi:10.1175/1520-0450(1976)015<0069:PUORDR>2.0.CO;2.

Shige, S., Y. N. Takayabu, S. Kida, W.-K. Tao, X. Zeng, C. Yokoyama, and T. L'Ecuyer, 2009: Spectral retrieval of latent heating profiles from TRMM PR data. Part IV: Comparisons of lookup tables from two- and three-dimensional cloud-resolving model simulations. *J. Climate*, **22**, 5577–5594, doi:10.1175/2009JCLI2919.1.

Shige, S., Y. N. Takayabu, and W.-K. Tao, 2008: Spectral retrieval of latent heating profiles from TRMM PR data. Part III: Estimating apparent moisture sink profiles over tropical oceans. *J. Appl. Meteor. Climatol.*, **47**, 620–640, doi:10.1175/2007JAMC1738.1.

Shige, S., Y. N. Takayabu, W.-K. Tao, and D. E. Johnson, 2004: Spectral retrieval of latent heating profiles from TRMM PR data. Part I: Development of a model-based algorithm. *J. Appl. Meteor.*, **43**, 1095–1113, doi:10.1175/1520-0450(2004)043<1095:SROLHP>2.0.CO;2.

Shige, S., Y. N. Takayabu, W.-K. Tao, and C.-L. Shie, 2007: Spectral retrieval of latent heating profiles from TRMM PR data. Part II: Algorithm improvement and heating estimates over tropical ocean regions. *J. Appl. Meteor. Climatol.*, **46**, 1098–1124, doi:10.1175/JAM2510.1.

Short, D. A. and K. Nakamura, 2000: TRMM radar observations of shallow precipitation over the tropical oceans. *J. Climate*, **13**, 4107–4124.

Sikdar, D. N., 1972: ATS-3 observed cloud brightness field related to a meso-to-subsynoptic scale rainfall pattern. *Tellus*, **24**, 400–413, doi:10.1111/j.2153-3490.1972.tb01567.x.

Sikdar, D. N., V. E. Suomi, and C. E. Anderson, 1970: Convective transport of mass and energy in severe storms over the United States–an estimate from a geostationary altitude. *Tellus*, **22**, 521–532, doi:10.1111/j.2153-3490.1970.tb00519.x.

Simpson, G. C., 1941: On the formation of cloud and rain. *Quart. J. Roy. Meteor. Soc.*, **67**, 99–133, doi:10.1002/qj.49706729002.

Simpson, J., R. F. Adler, and G. R. North, 1988: A proposed Tropical Rainfall Measuring Mission (TRMM) Satellite. *Bull. Amer. Meteor. Soc.*, **69**, 278–295, doi:10.1175/1520-0477(1988)069<0278:APTRMM>2.0.CO;2.

Skofronick-Jackson, G., W. A. Petersen, W. Berg, C. Kidd, E. F. Stocker, D. B. Kirschbaum, R. Kakar, S. A. Braun, G. J. Huffman, T. Iguchi, P. E. Kirstetter, C. Kummerow, R. Meneghini, R. Oki, W. S. Olson, Y. N. Takayabu, K. Furukawa, and T. Wilheit, 2017: The Global Precipitation Measurement (GPM) Mission for science and society. *Bull. Amer. Meteor. Soc.*, **98**, 1679–1695, doi:10.1175/BAMS-D-15-00306.1.

Smalley, M. and T. L'Ecuyer, 2015: A global assessment of the spatial distribution of precipitation occurrence. *J. Appl. Meteor. Climatol.*, **54**, 2179–2197, doi:10.1175/JAMC-D-15-0019.1.

Smalley, M., T. L'Ecuyer, M. Lebsock, and J. Haynes, 2014: A comparison of precipitation occurrence from the NCEP Stage IV QPE Product and the CloudSat Cloud Profiling Radar. *J. Hydrometeor.*, **15**, 444–458, doi:10.1175/JHM-D-13-048.1.

Smith, E., X. Xiang, A. Mugnai, and G. Tropoli, 1994: Design of an inversion-based precipitation proflie retrieval algorithm using an explicit cloud model for initial guess microphysics. *Meteor. Atmos. Phys.*, **54**, 53–78, doi:10.1007/BF01030052.

Spencer, R. W. and W. D. Braswell, 2008: Potential biases in feedback diagnosis from observational data: A simple model demonstration. *J. Climate*, **21**, 5624–5628, doi:10.1175/2008JCLI2253.1.

Stephens, G. L., 2005: Cloud feedbacks in the climate system: A critical review. *J. Climate*, **18**, 237–273, doi:10.1175/JCLI-3243.1.

Stephens, G. L. and T. J. Greenwald, 1991: The Earth's radiation budget and its relation to atmospheric hydrology: 1. Observations of the clear sky greenhouse effect. *J. Geophys. Res.*, **96**, 15311–15324, doi:10.1029/91JD00973.

Stephens, G. L., M. Z. Hakuba, M. Hawcroft, J. M. Haywood, A. Behrangi, J. E. Kay, and P. J. Webster, 2016: The curious nature of the hemispheric symmetry of the Earth's water and energy balances. *Curr. Climate Change Rep.*, **2**, 135–147, doi:10.1007/s40641-016-0043-9.

Stephens, G. L., J. Li, M. Wild, C. A. Clayson, N. Loeb, S. Kato, T. L'Ecuyer, P. W. Stackhouse, M. Lebsock, and T. Andrews, 2012: An update on Earth's energy balance in light of the latest global observations. *Nature Geosci.*, **5**, 691–696, doi:10.1038/ngeo1580.

Stephens, G. L., D. G. Vane, R. J. Boain, G. G. Mace, K. Sassen, Z. Wang, A. J. Illingworth, E. J. O'Connor, W. B. Rossow, S. L. Durden, S. D. Miller, R. T. Austin, A. Benedetti, C. Mitrescu, and T. C. S. Team, 2002: The CloudSat mission and the A-Train. *Bull. Amer. Meteor. Soc.*, **83**, 1771–1790, doi:10.1175/BAMS-83-12-1771.

Stephens, G. L., D. G. Vane, S. Tanelli, E. Im, S. Durden, M. Rokey, D. Reinke, P. Partain, G. G. Mace, R. Austin, T. L'Ecuyer, J. Haynes, M. Lebsock, K. Suzuki, D. Waliser, D. Wu, J. Kay, A. Gettelman, Z. Wang, and R. Marchand, 2008: CloudSat mission: Performance and early science after the first year of operation. *J. Geophys. Res.*, **113**, D00A18, doi:10.1029/2008JD009982.

Stevens, B., 2002: Entrainment in stratocumulus-topped mixed layers. *Quart. J. Roy. Meteor. Soc.*, **128**, 2663–2690, doi:10.1256/qj.01.202.

Stevens, B., D. Farrell, L. Hirsch, F. Jansen, L. Nuijens, I. Serikov, B. Brügmann, M. Forde, H. Linne, K. Lonitz, and J. M. Prospero, 2016: The Barbados Cloud Observatory: Anchoring investigations of clouds and circulation on the edge of the ITCZ. *Bull. Amer. Meteor. Soc.*, **97**, 787–801, doi:10.1175/BAMS-D-14-00247.1.

Sun, F., A. Hall, and X. Qu, 2011: On the relationship between low cloud variability and lower tropospheric stability in the Southeast Pacific. *Atmos. Chem. Phys.*, **11**, 9053–9065, doi:10.5194/acp-11-9053-2011.

Suomi, V. R., 1961: The thermal radiation balance experiment on board Explorer VII. *Juno II summary project report: Explorer VII satellite*, National Aeronautics and Space Administration, Washington, D.C., volume 1, 273–305, nASA Technical Report D-608.
URL `http://library.ssec.wisc.edu/SuomiWebsite/SuomiImages/scanned%20documents/Suomi_ExplorerVII_Radiometer_018.pdf`

Tanelli, S., S. L. Durden, E. Im, K. S. Pak, D. G. Reinke, P. Partain, J. M. Haynes, and R. T. Marchand, 2008: CloudSat's Cloud Profiling Radar after two years in orbit: Performance, calibration, and processing. *IEEE Trans. Geosci. Remote Sensing*, **46**, 3560–3573, doi:10.1109/TGRS.2008.2002030.

Tao, W.-K., Y. N. Takayabu, S. Lang, S. Shige, W. Olson, A. Hou, G. Skofronick-Jackson, X. Jiang, C. Zhang, W. Lau, T. Krishnamurti, D. Waliser, M. Grecu, P. E. Ciesielski, R. H. Johnson, R. Houze, R. Kakar, K. Nakamura, S. Braun, S. Hagos, R. Oki, and A. Bhardwaj, 2016: TRMM latent heating retrieval: Applications and comparisons with field campaigns and large-scale analyses. *Meteor. Monogr.*, **56**, 2.1–2.34.

Taylor, K. E., R. J. Stouffer, and G. A. Meehl, 2012: An overview of CMIP5 and the experiment design. *Bull. Amer. Meteor. Soc.*, **93**, 485–498.

Thompson, R. M., S. W. Payne, E. E. Recker, and R. J. Reed, 1979: Structure and properties of synoptic-scale wave disturbances in the Intertropical Convergence Zone of the Eastern Atlantic. *J. Atmos. Sci.*, **36**, 53–72, doi:10.1175/1520-0469(1979)036<0053:SAPOSS>2.0.CO;2.

Trenberth, K. E. and J. M. Caron, 2001: Estimates of meridional atmosphere and ocean heat transports. *J. Climate*, **14**, 3433–3443, doi:10.1175/1520-0442(2001)014<3433:EOMAAO>2.0.CO;2.

Trenberth, K. E., J. T. Fasullo, and M. A. Balmaseda, 2014: Earth's energy imbalance. *J. Climate*, **27**, 3129–3144, doi:10.1175/JCLI-D-13-00294.1.

Trenberth, K. E., J. T. Fasullo, and J. Kiehl, 2009: Earth's global energy budget. *Bull. Amer. Meteor. Soc.*, **90**, 311–323, doi:10.1175/2008BAMS2634.1.

Tsai, J.-Y. and C.-M. Wu, 2016: Critical transitions of stratocumulus dynamical systems due to perturbation in free-atmosphere moisture. *Dyn. Atmos. Oceans*, **76**, 1–13, doi:10.1016/j.dynatmoce.2016.08.002.

Turk, J., 2016: 2B-CSATGPM-COIN: Experimental CloudSat–GPM Coincidence Dataset Version 1.

van Tricht, K., S. Lhermitte, J. T. M. Lenaerts, I. V. Gorodetskaya, T. S. L'Ecuyer, B. Noël, M. R. van den Broeke, D. D. Turner, and N. P. M. van Lipzig, 2015: Clouds enhance Greenland ice sheet meltwater runoff. *Nature Communications*, **7**, 10266, doi:10.1038/ncomms10266.

Ventrice, M. J., M. C. Wheeler, H. H. Hendon, C. J. Schreck III, C. D. Thorncroft, and G. N. Kiladis, 2013: A modified multivariate Madden-Julian Oscillation index using velocity potential. *Mon. Wea. Rev.*, **141**, 4197–4210, doi:10.1175/MWR-D-12-00327.1.

Waliser, D. E. and C. Gautier, 1993: A satellite-derived climatology of the ITCZ. *J. Climate*, **6**, 2162–2174, doi:10.1175/1520-0442(1993)006<2162:ASDCOT>2.0.CO;2.

Wallace, J. M. and C. Chang, 1969: Spectrum analysis of large-scale wave disturbances in the tropical lower troposphere. *J. Atmos. Sci.*, **26**, 1010–1025, doi:10.1175/1520-0469(1969)026<1010:SAOLSW>2.0.CO;2.

Weaver, C. P., 2003: Efficiency of storm tracks an important climate parameter? The role of cloud radiative forcing in poleward heat transport. *J. Geophys. Res.*, **108**, 4018, doi:10.1029/2002JD002756.

Wedgwood, J. and J. Banks, 1782: An attempt to make a thermometer for measuring the higher degrees of heat, from a red heat up to the strongest that vessels made of clay can support. *Philos. Trans. Roy. Soc. London*, **72**, 305–326, doi:10.1098/rstl.1782.0021.

Wheeler, M. C. and H. H. Hendon, 2004: An all-season real-time multivariate mjo index: Development of an index for monitoring and prediction. *Mon. Wea. Rev.*, **132**, 1917–1932, doi:10.1175/1520-0493(2004)132<1917:AARMMI>2.0.CO;2.

Wielicki, B. A., B. R. Barkstrom, E. F. Harrison, R. B. L. III, G. L. Smith, and J. E. Cooper, 1996: Clouds and the Earth's Radiant Energy System (CERES): An Earth observing system experiment. *Bull. Amer. Meteor. Soc.*, **77**, 853–868, doi:10.1175/1520-0477(1996)077<0853:CATERE>2.0.CO;2.

Williams, E., D. Rosenfeld, N. Madden, J. Gerlach, N. Gears, L. Atkinson, N. Dunnemann, G. Frostrom, M. Antonio, B. Biazon, R. Camargo, H. Franca, A. Gomes, M. Lima, R. Machado, S. Manhaes, L. Nachtigall, H. Piva, W. Quintiliano, L. Machado, P. Artaxo, G. Roberts, N. Renno, R. Blakeslee, J. Bailey, D. Boccippio, A. Betts, D. Wolff, B. Roy, J. Halverson, T. Rickenbach, J. Fuentes, and E. Avelino, 2002: Contrasting convective regimes over the amazon: Implications for cloud electrification. *J. Geophys. Res.*, **107**, LBA 50–1–LBA 50–19, doi:10.1029/2001JD000380, 8082.

Winker, D. M., M. A. Vaughan, A. Omar, Y. Hu, K. A. Powell, Z. Liu, W. H. Hunt, and S. A. Young, 2009: Overview of the calipso mission and caliop data processing algorithms. *J. Atmos. Oceanic Technol.*, **26**, 2310–2323, doi:10.1175/2009JTECHA1281.1.

Wodzicki, K. R. and A. D. Rapp, 2016: Long-term characterization of the Pacific ITCZ using TRMM, GPCP, and ERA-Interim. *J. Geophys. Res.*, **121**, 3153–3170, doi:10.1002/2015JD024458.

Wood, R., 2012: Stratocumulus clouds. *Mon. Wea. Rev.*, **140**, 2373–2423, doi:10.1175/MWR-D-11-00121.1.

Wood, R. and C. S. Bretherton, 2006: On the relationship between stratiform low cloud cover and lower-tropospheric stability. *J. Climate*, **19**, 6425–6432, doi:10.1175/JCLI3988.1.

Wyant, M., C. Bretherton, H. Rand, and D. Stevens, 1997: Numerical simulations and a conceptual model of the stratocumulus to trade cumulus transition. *J. Atmos. Sci.*, **54**, 168–192, doi:10.1175/1520-0469(1997)054<0168:NSAACM>2.0.CO;2.

Wyant, M. C., C. S. Bretherton, J. T. Bacmeister, J. T. Kiehl, I. M. Held, M. Zhao, S. A. Klein, and B. J. Soden, 2006: A comparison of low-latitude cloud properties and their response to climate change in three AGCMs sorted into regimes using mid-tropospheric vertical velocity. *Climate Dyn.*, **27**, 261–279, doi:10.1007/s00382-006-0138-4.
URL `http://dx.doi.org/10.1007/s00382-006-0138-4`

Yamada, R. and O. Pauluis, 2015: Annular mode variability of the atmospheric meridional energy transport and circulation. *J. Atmos. Sci.*, **72**, 2070–2089.

Yanai, M., S. Esbensen, and J.-H. Chu, 1973: Determination of bulk properties of tropical cloud clusters from large-scale heat and moisture budgets. *J. Atmos. Sci.*, **30**, 611–627, doi:10.1175/1520-0469(1973)030<0611:DOBPOT>2.0.CO;2.

Yanai, M., T. Maruyama, T. Nitta, and Y. Hayashi, 1968: Power spectra of large-scale disturbances over the Tropical Pacific. *J. Meteor. Soc. Japan*, **46**, 308–323, doi:10.2151/jmsj1965.46.4_308.

Yang, S. and E. A. Smith, 1999: Four-dimensional structure of monthly latent heating derived from SSM/ISatellite measurements. *J. Climate*, **12**, 1016–1037, doi:10.1175/1520-0442(1999)012<1016:FDSOML>2.0.CO;2.

Yu, H., M. Zhang, W. Lin, and X. Zhang, 2017: Cloud transitions: Comparison of temporal variation in the southeastern Pacific with the spatial variation in the northeastern Pacific at low latitudes. *Int. J. Climatol.*, **37**, 2923–2933, doi:10.1002/joc.4889.

Yu, L. and R. A. Weller, 2007: Objectively analyzed air-sea heat fluxes for the global ice-free oceans (1981-2005). *Bull. Amer. Meteor. Soc.*, **88**, 527–539, doi:10.1175/BAMS-88-4-527.

Yuter, S. E. and R. A. Houze Jr., 1995: Three-dimensional kinematic and microphysical evolution of Florida cumulonimbus. Part I: Spatial distribution of updrafts, downdrafts, and precipitation. *Mon. Wea. Rev.*, **123**, 1921–1940, doi:10.1175/1520-0493(1995)123<1921:TDKAME>2.0.CO;2.

Zhang, C., 2013: Madden-Julian Oscillation: Bridging weather and climate. *Bull. Amer. Meteor. Soc.*, **94**, 1849–1870, doi:10.1175/BAMS-D-12-00026.1.

Zhang, G. J. and X. Song, 2009: Interaction of deep and shallow convection is key to madden-julian oscillation simulation. *Geophys. Res. Lett.*, **36**, L09708, doi:10.1029/2009GL037340.

Zhang, M., C. S. Bretherton, P. N. Blossey, P. H. Austin, J. T. Bacmeister, S. Bony, F. Brient, S. K. Cheedela, A. Cheng, A. D. Del Genio, S. R. De Roode, S. Endo, C. N. Franklin, J.-C. Golaz, C. Hannay, T. Heus, F. A. Isotta, J.-L. Dufresne, I.-S. Kang, H. Kawai, M. Köhler, V. E. Larson, Y. Liu, A. P. Lock, U. Lohmann, M. F. Khairoutdinov, A. M. Molod, R. A. J. Neggers, P. Rasch, I. Sandu, R. Senkbeil, A. P. Siebesma, C. Siegenthaler-Le Drian, B. Stevens, M. J. Suarez, K.-M. Xu, K. von Salzen, M. J. Webb, A. Wolf, and M. Zhao, 2013: CGILS: Results from the first phase of an international project to understand the physical mechanisms of low cloud feedbacks in single column models. *J. Adv. Model. Earth Sys.*, **5**, 826–842, doi:10.1002/2013MS000246.

Zhang, M. H., W. Y. Lin, S. A. Klein, J. T. Bacmeister, S. Bony, R. T. Cederwall, A. D. Del Genio, J. J. Hack, N. G. Loeb, U. Lohmann, P. Minnis, I. Musat, R. Pincus, P. Stier, M. J. Suarez, M. J. Webb, J. B. Wu, S. C. Xie, M.-S. Yao, and J. H. Zhang, 2005: Comparing clouds and their seasonal variations in 10 atmospheric general circulation models with satellite measurements. *J. Geophys. Res.*, **110**, D15S02, doi:10.1029/2004JD005021.

Zhang, Y., W. B. Rossow, A. A. Lacis, V. Oinas, and M. I. Mishchenko, 2004: Calculation of radiative fluxes from the surface to top of atmosphere based on ISCCP and other global data sets: Refinements of the radiative transfer model and the input data. *J. Geophys. Res.*, **109**, D19105, doi:10.1029/2003JD004457.

Zhang, Y. C. and W. B. Rossow, 1997: Estimating meridional energy transports by the atmospheric and oceanic general circulations using boundary fluxes. *J. Climate*, **10**, 2358–2373, doi:10.1175/1520-0442(1997)010<2358:EMETBT>2.0.CO;2.

Zhou, X., P. Kollias, and E. R. Lewis, 2015: Clouds, precipitation, and marine boundary layer structure during the MAGIC field campaign. *J. Climate*, **28**, 2420–2442, doi:10.1175/JCLI-D-14-00320.1.